Engineering microenvironmental cues for guiding stem cell fate

By

Ji Sun Park

Submitted in partial fulfillment of the
requirements for the degree of
Doctor of Philosophy
in the Graduate School of Arts and Sciences

COLUMBIA UNIVERSITY

2020

Abstract

Engineering Microenvironmental Cues for Guiding Stem Cell Fate

Ji Sun Park

Injury, aging, and congenital disabilities of the muscular and neural systems impose a significant burden on patients and their families. Due to the tissue's limited regenerative capacity, effective treatment interventions for restoring progressive damage is still lacking. Cell replacement therapy is primarily limited by the restricted supply of viable donor cells and variable graft survival. For addressing these limitations, we propose new strategies to obtain a target cell of interest from an autologous cell source. Herein, we engineer cell fate decisions by 1) harnessing host microenvironment and the CRISPR/dCas9-mediated transcriptional activation system to promote myogenesis of human endothelial progenitor cells (EPCs); and 2) employing substrate-mediated biophysical cues with soluble factors (biochemical cues) to drive cell commitment to neuronal lineages.

For the first strategy, we hypothesized that therapeutic cells could be obtained *in situ* by employing the CRISPR/dCas9 system to engineer cell fate in the host tissue. Using this system, we transactivated MYOD1, a master regulator for myogenesis, to directly reprogram primary EPCs to skeletal myoblasts (SkMs). EPCs were chosen as a cell source for their easy accessibility, high proliferation, and potential contribution to regenerate vasculature and musculature tissue. The early myogenic commitment of EPCs was confirmed *in vitro* by MYOD1 expression, which yielded a 230-fold higher induction than the original EPCs. These cells were then transplanted for assessing their therapeutic efficacy in myotoxin-induced muscle injury model in immunodeficient mice. A one-month post-injury study resulted in the integration of induced SkMs to the injured host tissue, promotion of neoangiogenesis, and

reduction in fibrotic scar formation. These findings indicate that CRISPR/Cas9-mediated target gene activation can be achieved *in situ* to accelerate muscle regeneration after myotoxin-induced damage.

For the second strategy, we utilized both soluble and insoluble factors to convert the cell fate of neural stem/progenitor and somatic cells to various neuronal lineages, including motor neurons (MNs) and dopaminergic (DA) neurons. For soluble factors, cells were exposed to various biochemical factors, inspired by the neuronal niche environs during the natural developmental process. For insoluble factors, the conductive graphene substrate was used to support the endogenous electrical signal between neurons for enhancing the neuronal phenotypes and their functionality. We postulated that exposing the cells to these collective stimuli *in vitro* can alter their intrinsic signaling pathway to tailor their fate to neuronal lineages. To test the hypothesis, neural stem/progenitor and somatic cells were cultured on various substrates with or without electroactive graphene and aligned patterns. After two weeks to one month of cell fate induction in the chemically defined conditions, our results implied that cell adhesion, survival, neurite outgrowth, and maturation were facilitated on the electroactive substrates with aligned patterns compared to the control platforms.

Taken together, our results in this dissertation demonstrate the feasibility of tailoring the donor cell fates within or across the germ layers. We achieved this by employing a transcriptional gene activation system and tunable microenvironmental cues elicited by soluble (chemical and growth factors) and insoluble (physical cues from the substrate) factors. Utilizing such strategies hold great promise for elucidating the optimal conditions to guide cell fate to target lineages. This work provides a rational basis for establishing a robust protocol and an *in vitro* culture platform to module cell fate decisions that could help realize the autologous cell-based therapy for muscular and neurodegenerative diseases.

Table of Contents

List of Figures

List of Tables

Acknowledgement

The completion of my Ph.D. work would have been impossible without the guidance, stimulation, and continuous support from numerous mentors, collaborators, friends, and families. First, I would like to express my gratitude to Prof. Kam W. Leong for allowing me to continue and complete my degree at Columbia University. Your productive criticism, patient mentoring, and humble diligence not only influenced me to freely execute my ideas and deepen my knowledge in this field, but also facilitated to rediscover myself. I will forever support and respect your passion for conducting good science, and devotion for being a loving father by running long-distance races with Wei, respectively.

I also sincerely thank my committee members – Profs. Lu, Vunjak-Novakovic, Kim, Xu, and Sia – who had made themselves available during their frantic schedules at their offices, in a tiny conference room, and over Skype and phone. They always kept the exam ambiance optimistic and stimulating by sharing their thoughtful suggestions and questions with scientific acumen.

My recognition extends to my undergraduate research advisor, Prof. Narendra Singh, who has first introduced and cultivated the joy of helping cancer patients to me through research outcomes. You are dearly missed, and your humble leadership and legacy will continue throughout my life for serving others.

I am truly indebted to my mentors Dr. Syandan Chakraborty and Dr. Jong-Wan Kim, who spent extra efforts on teaching and inspiring me to practice perfection and a divine work ethic. Their patient coaching equipped me with the fundamental techniques for conducting research *in vitro* and *in vivo*. I also sincerely appreciate the contributions made by all my collaborators and colleagues, including Dr. Hongxia(xia) Wang, Dr. Hyesung Kim, Dr. Chinmaya Mahapatra, Teresa Cauvel, Dr. Adam Jakus, Dr. Damian Williams, Dr. Saera Song, Prof. Hae Won Kim, Prof. Ramile Shah, Dr. Sang Min Park, Dr. Hong Sun An, Dr. Nicholas Hornstein, Prof. Zaozao Chen, Prof. Peter Sims, and Prof. Hosup Shim. I genuinely thank you all for your concerted efforts in having countless meetings for planning, troubleshooting, and sharing the updated data.

Coping with abrupt transitions – from Duke to Columbia and Columbia to Dankook University – would have been difficult without my dear friends who warmly welcomed me into the scientific families of the Tosh lab, Duke BME, Leong lab, and ITREN. I would like to especially thank Nick Tang, Parisa Yousefpour, Stacey Qi, Anna Lee, Sena Bae, Kate Ho, Danielle Huang, Jing Gong, Helen Lee, Wei Leong, Jungju Kim, Hahee Shin, Jennifer Olmos, Minsil Kang, Meeju Kim, and Mark Baek, for their emotional support, camaraderie, entertainment, and care that they have provided.

Outside of the research lab, I would like to thank my friends, Stella Chun, Joanne Lee, Katherine Cho, Yungtai Yoo, Tim Liu, Dennis Su, and Seth Kim, for satisfying my adventurous appetite in exploring life outside of the lab. I am grateful for your fellowship, encouragement, and moral support, which have kept me sound and safe during this journey. Special thanks go to my brothers and sisters in the body of Christ – from the Adelpos, Hanmaum Church, and Campus Mission Church – who have kept me in their prayers. I will cherish all the moments that we have shared to learn and spread the Gospel and God’s love to our neighbors in Seattle, Durham, and New York. I would also like to acknowledge the financial support granted by the Andrew Kim Memorial Foundation, KSEA-KUSCO, and the Mary Gates Foundation throughout my academic career.

Lastly, I would like to dedicate the culmination of my work to my beloved parents, sister, grandparents, and the extended families who have (had) sacrificed and enabled me to pursue my dream abroad.

Chapter 1. Introduction: motivation and objectives

1.1. Clinical Significance: Muscular and Neuronal Diseases

With the increase in life expectancy and advances in medical prognosis, patients with muscular and neuronal diseases (MNDs) are projected to elevate across the world. It is more devastating as a wide range of progressive MNDs currently lack viable treatment options and only partially relies on the rehabilitation and palliative treatment methods to alleviate the symptoms, instead of restoring the loss of tissues. This stems from an inability to proliferate and replace the damaged tissues and not being able to obtain self-renewing therapeutic cells for replacing damaged tissues. Therefore, lacking effective therapeutic modalities still imposes a high societal and economic burden on patients with MNDs.

For circumventing these limitations, numerous groups have investigated on how cellular microenvironments can be modulated for stem cell development, activation, and differentiation either by cell-to-surface or cell-to-cell interactions. Among the various strategies, three of them are employed herein to modulate programmed cell determination: 1) 3D microenvironmental cues, 2) cocktails of soluble factors, and 3) insoluble biomaterial-mediated topographical cues.

For achieving cell fate transition, we targeted the excitable cells, which transmits action potential signals from the central nervous system (CNS) to skeletal myofibers at the neuromuscular junction (NMJ); MN's axon transmits chemical signals across a synapse from the spinal cord to skeletal muscle for facilitating voluntary movements (Figure 1). For both systems, cell migration and chemosensation are the critical factors for efficient myogenesis and

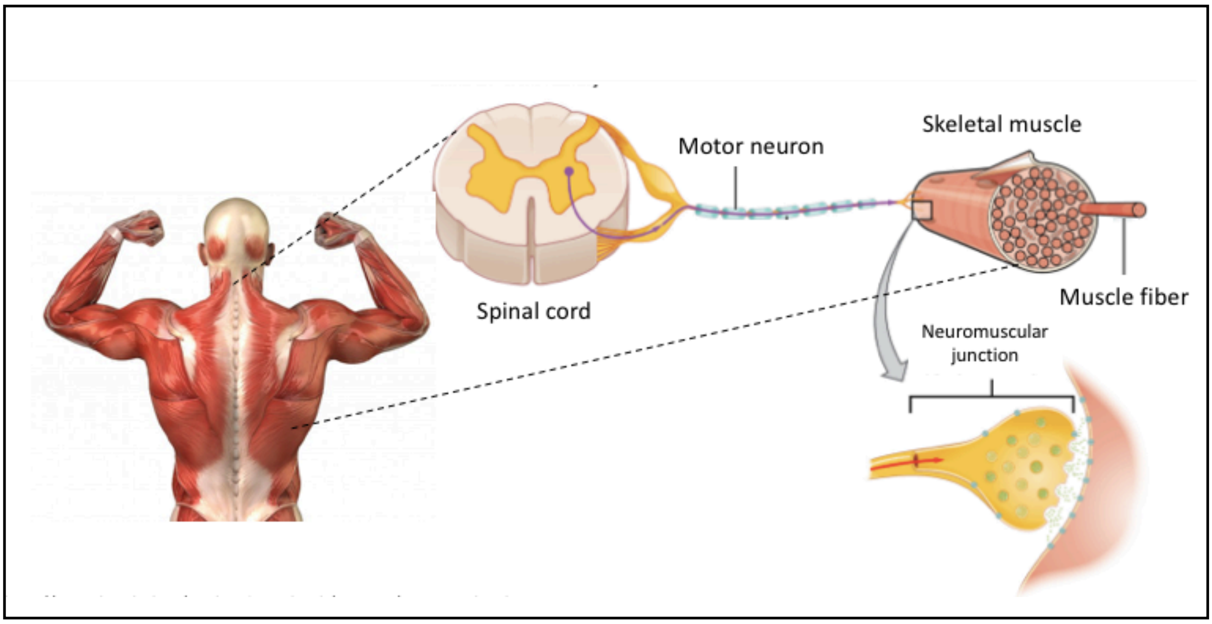

Figure 1. Target neuronal and muscular systems for the study. Adapted from (“Github,” 2017)

neurogenesis. They are closely connected at the neuromuscular junction to process the electrochemical signals from the CNS to the contractile machinery for generating voluntary movements. Any impairment or interruption from the injury or disease between these systems would lead to compromised muscle/neural functions, paralysis, or suffer in pain for the rest of one's life. This is due to the limited regeneration capability of the mitotically quiescent mature neuronal and muscular cells.

1.1.1. Muscular injury/disease

Musculoskeletal diseases from aging, trauma, injury, and genetic mutations induce muscle weakness and impaired functions. Although it is a significant challenge our society and it only expects to escalate as the life expectancy is projected to increase, no effective treatment modalities are available.

1.1.2. Neurodegenerative disease

For the scope of this study, we plan to focus only on the two major neurodegenerative diseases, which are one of the most debilitating, costly, prevalent, and incurable diseases: Lou Gehrig's Disease/Amyotrophic lateral sclerosis (ALS) and Parkinson's disease (PD).

ALS, named after a baseball player Mr. Lou Gehrig, is a fatal neurodegenerative disease caused by the progressive death of MNs, regulating the voluntary movements. It affects about 30,000 patients every year worldwide and the average life expectancy from two to five years.

PD is the second most common neurodegenerative disorder of the central nervous system (CNS) in the U.S. with symptoms that exacerbate as the disease advances. It is known to be caused by the loss of midbrain dopaminergic (mDA) neurons, and its impaired motor symptoms are characterized by muscle rigidity, tremor, bradykinesia, and poor balance in walking. Currently, it is affecting 1 million patients in the U.S. per year, with a total of 10 million patients in the world. The indirect healthcare costs add up to 25 billion per person in a year. The progressive degeneration of mDA is one of the significant pathological causes in PD.

1.2. Limitations of the Current Therapeutic Modalities

Current technology diagnoses ALS about 9-12 months on average to begin noticing the symptoms, while for PD, patients will be diagnosed only after losing 40-70 % of DA neurons during the progression of the disease. The more discouraging fact is that during the delay in diagnosis, patients' condition would progressively get worse over time. Moreover, available approved modalities only mildly relieve the symptoms and, but wouldn't ultimately restore the voluntary muscle function. For instance, ALS patient given with the first approved Riluzole prevents the further loss of MNs by regulating the release of glutamate, but cannot restore the progression of the disease (Petrov, Mansfield, Moussy, & Hermine, 2017).

For both MNDs, fetal grafts have been used as an attempt to restore the disease symptoms. However, due to the lack of viable supply donor cells, associated ethical issues, and high immune response, transplanting grafts lead to failure.

1.3. Cell-based Therapy as an Alternative Approach

Being highly proliferative and having immunomodulation response, myriads of stem cells are being tested to circumvent the ethical issues regarding the usage of fetal grafts from conceived embryos. There are currently 24 registered clinical trials for ALS treatment to transplant different cell sources, intravenously, or intramuscularly (*i.m.*). For cell sources, human spinal cord-derived neural stem/progenitor cells (NSCs/NPCs), Peripheral blood mononuclear cells (PBMC), MSCs secreting neurotrophic factors, astrocytes derived from ESCs, and adipose tissue-derived stem cells have been registered (“NIH Clinical Trials1,” 2019).

Similarly, 12 registered clinical trials for the PD treatment practices the usage of MSCs, NSCs, NSC-derived neurons, and NPCs into the intracerebral cortex (“NIH Clinical Trials2,” 2019). Various cell sources have been explored for this approach: 1) grafting donated fetal tissues; 2) transplanting human embryonic stem cell (ESC)- or iPSC-derived multipotent stem/progenitor cells, including PBMC, mesenchymal stem cells (MSCs), NSCs and NPCs; and 3) implanting autologous cells derived from patients. Especially, stem/progenitor cells derived from mesoderm PBMC, mesenchymal stem cells (MSCs), and adipose-derived stem cells (ADSCs) have been extensively used as a cell source for their highly proliferative capacity (with well-defined proliferation media compositions and characterization markers), easy accessibility, immunomodulatory behaviors, and paracrine effect for secreting tropical effectors.

Cell-based therapy has galvanized its recognition as an alternative modality against treating muscular and neural diseases (MNDs) for cells being identified as independent dynamic machinery, adapting and responding to their surrounding environs. Attributing to these features of cells, researchers hypothesized that implanted cells could expand in a host environment to migrate, proliferate, and mitigate pathophysical responses in congenital abnormalities, diseased or injured tissues by reducing inflammation and secreting tropical effectors. In this aspect, autologous cell replacement therapy has become an ideal therapeutic intervention for the regenerative cell-based therapies with no associated ethical concerns and risks of teratoma formation using pluripotent stem cells (PSCs).

Replacing stem cells or terminally differentiated cells have limited therapeutic potentials attributed to the limited ability to obtain sizable amounts of implantable cells at these target sites. To address this limitation of obtaining therapeutically relevant amounts of cells for autologous cell therapy. Our strategies involve modulating the microenvironmental cues to regulate cell fate decisions (differentiation, reprogramming, and transdifferentiation) by 1) directly converting the cell lineage through targeted transcriptional activation, or 2) mimicking the target cell niche to provide tailored stimuli to cells.

1.4. Objective and Specific Aims

The *objective* of my thesis is to obtain therapeutic cells for regenerative medicine in cell-based therapy and tissue engineering applications by developing a robust technique and an *in vitro* culture platform for altering the transcriptional fate of stem/progenitor and somatic cells. We expect that developing these lineage-specific target cells can lead to realizing the autologous cell-based therapy against MNDs, which currently lacks viable treatment options. We *hypothesize* that employing various environmental cues inspired by the cell's niche would instruct and regulate cell fate outcomes for the neuronal and muscular systems. To validate our hypothesis, we harnessed a targeted transcriptional activation system and biomimetic microenvironmental cues (soluble and insoluble factors) for promoting transdifferentiation and differentiation in the muscular and neuronal systems, respectively. The microenvironmental cues in this study encompass orchestrated signals from the *in vivo* microenvironment, biochemical cues from the supplemented media, and bioelectrical and topographical cues from the substrate. Utilizing these factors, herein, we attempt to mitigate the current processes of expensive, inefficient, and cumbersome *in vitro* expansions of target cells by providing their niche-like environments. Figure 2 illustrates the common theme of the thesis and specific aims developed to guide the cell fate commitment.

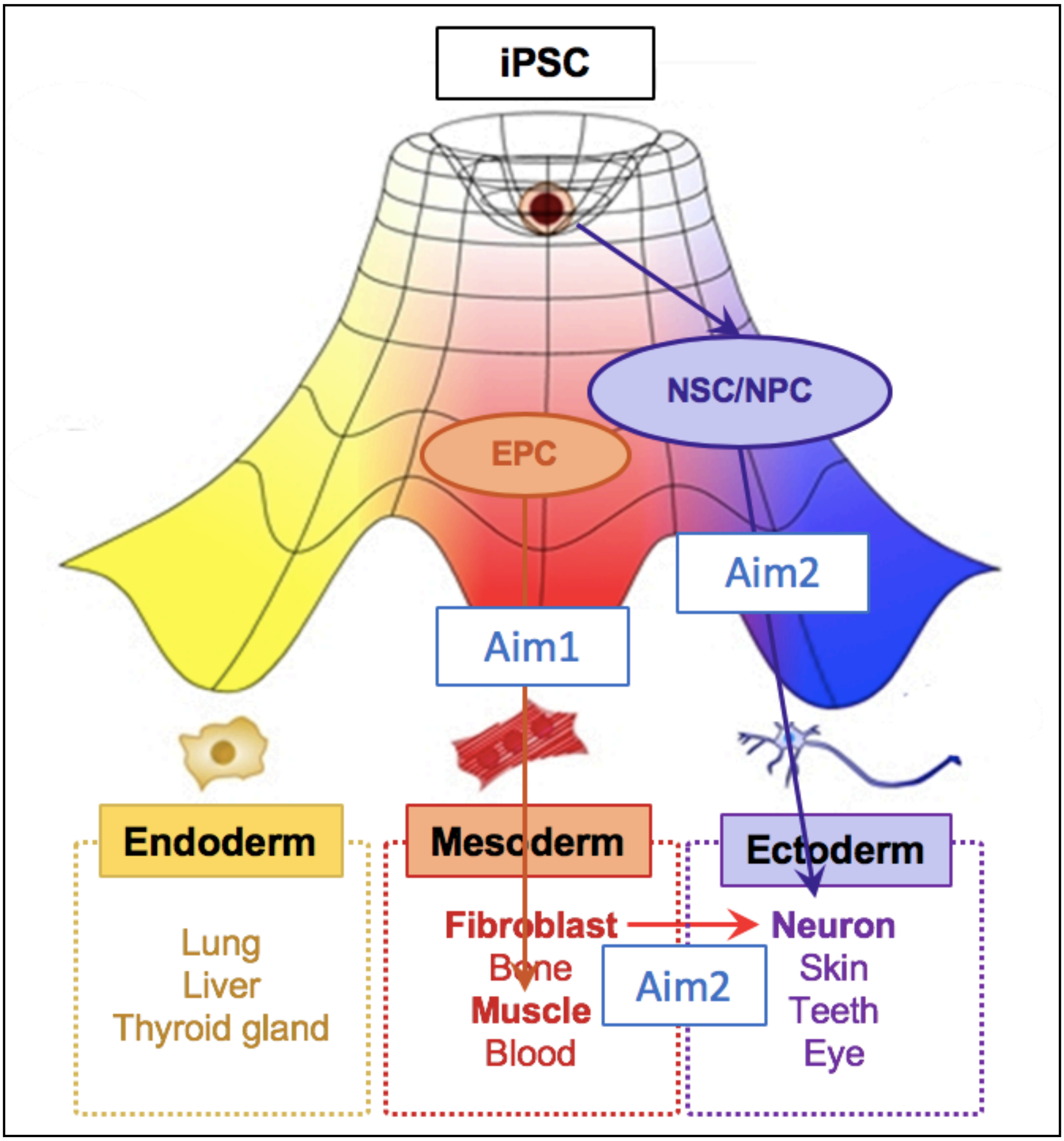

Figure 2. The summarized illustration of inter-lineage cell fate conversions aims to achieve for the thesis. Aim 1 demonstrates the promoted myogenic potential of mesodermal-derived multipotent endothelial progenitor cells (EPC) to SkM, and Aim 2 evaluates to enhance the directed differentiation of iPSC-derived NSC/NPC to specific neuronal lineages and direct conversion of fibroblast to induced neurons.

1.4.1. Specific Aim 1: Harnessing the in vivo host microenvironment for the in situ reprogramming of EPCs using the CRISPR/dCas9 system

i. Establishing reprogrammable EPCs in vitro using the CRISPR/dCas9 system
ii. Evaluating the engraftment and maturation of the reprogrammed EPCs in vivo
iii. Assessing the contribution of the non-reprogrammed cells to neoangiogenesis

---

Hypothesis: Microenvironmental cues from the in vivo host muscle promotes the myogenic potential of transduced EPCs by activation of endogenous MYOD1 using the CRISPR/dCas9 system

In specific aim 1, we employed the clustered regularly interspaced short palindromic repeats (CRISPR)-associated protein 9 (CRISPR/Cas9) gene-editing system to genetically modulate cell commitment. For inducing myogenesis of the primary human endothelial progenitor cells (EPCs), deactivated dCas9 was used to transactivate the target endogenous gene instead of causing a double-strand break. Unlike conventional forced ectopic expression of transcription factors, the CRISPR/dCas9 activation system allows economic and precise control of the transcriptional network with potential for multiplexing.

Utilizing this gene-editing tool, we first established a protocol to obtain reprogrammable EPCs by transducing them with doxycycline (dox)-inducible lentiviruses for delivering CRISPR/dCas9, gRNAs, and m2rtTA. Although optimized gRNA cocktails were used and transduced EPCs were further sorted to select the cells expressing *MYOD1,* our target gene, resulting transduced EPCs had immature skeletal myoblasts *in vitro* even after the long-term induction. Hence, requiring additional biochemical cues that mimics the niche-like microenvironment to further mature to functional skeletal muscle cells.

Based on the limited capacity of cell fate conversion *in vitro*, we hypothesized that the *in vivo* microenvironment would facilitate the cell commitment decisions *in situ*. To increase the survivability, integration, and reprogramming efficiency of transplanted cells *in vivo,* a myotoxin-induced muscle injury model of an immunodeficient mammalian model was selected as a host.

Lastly, as the direct lineage conversion process cannot be 100 % efficient, we assessed the function of non-reprogrammed EPCs to the local neoangiogenesis for ameliorating the injury site.

1.4.2. Specific Aim 2: Employing substrate-mediated bioelectrical and topographical cues to enhance the cell fate-specific to neuronal lineages

i. Promoting the directed differentiation of human NSCs to neuronal lineages
ii. Enhancing the small molecule-mediated direct reprogramming of human fibroblasts to induced neurons

---

Hypothesis: Electroactive substrates offering the topographical and biochemical cues enhances the cell fate decisions to neuronal lineages along with the soluble cues provided by the chemically-defined conditions.

For the specific aim 2, it was hypothesized that we could instruct neural stem/progenitor cells (NS/PCs) to mature and achieve functional neuronal lineages as well as guide fibroblasts to transdifferentiate into induced neurons (iNs) using cocktails of multiple soluble factors synergistically combined with substrate-mediated bioelectrical and topographical cues. This strategy eliminates the usage of transcription factors and viruses to deliver them, allowing for a simple, rapid, cost-effective, and safe method to epigenetically convert cell commitments. Moreover, the usage of chemical cocktails renders a more conducive environment for transformation or maturation to neuronal lineages by remodeling chromatin structures. For the substrate, highly conductive graphene: poly-lactide-*co*-glycolide (PLG) copolymer composite was used to examine the effect of an electroactive substrate on enhancing the adaptation of the neuronal lineage possibly through promoting their cell-to-cell signaling. Furthermore, an anisotropic patterned substrate was assessed for instructing cell alignment, an additional influence on cell phenotype change. For both MN differentiation and neurogenesis of fibroblasts, patterned graphene substrate had the most efficient conversion of cells with higher attachment compared with the control. These findings may advance our understanding of how multifunctional-engineered biomaterials can play a significant role in developing optimal differentiation and transdifferentiation platforms by mimicking the intricacy of natural tissue environments.

Collectively, these findings reveal that specific cell lineage determinations can be tailored by modulating intricate microenvironmental cues, directly, by activating the lineage-specific master regulator gene or indirectly, by exposing cells to chemical, bioelectrical, and topographical cues from their culture conditions (media and substrates). With these culture systems, more autologous target cells of interest may be obtained with less time and effort. These systems may, in turn, serve as emerging cell-based therapies for MNDs or be incorporated into engineered tissues for drug screening and discovery.

1.5. Chapter Overview

The common topic throughout this dissertation is to harness the soluble and insoluble microenvironmental cues (*e.g.,* substrate-mediated biophysical factors and soluble biochemical factors) with a goal to obtain autologous therapeutic cells for *in vivo* applications, and to establish an *in vitro* culturing protocol/platform to realize personalized regenerative medicine against neuronal and muscular injuries/diseases.

Especially, **Chapter 2.** Background information of the dissertation reviews the relevant background information to help understand the research topics. **Chapter 3.** *In situ* reprogramming of EPCs by transactivation of endogenous *MYOD1* using the CRISPR/dCas9 system examines the therapeutic efficacy of utilizing CRISPR/dCas9-mediated targeted transcription for cell fate conversion of human EPCs to induced SkMs (iSkMs) in the niche-like *in vivo* system. While, **Chapter 4.** Enhancing the neural cell fate commitment by deploying biochemical cues and substrate-mediated electrophysical cues attempts to establish an electroactive *in vitro* culture platform to enhance the cell fate conversion to subtype neuronal cell commitment from various cell sources exposed to defined biochemical and physical cues. Collectively, **Chapter 5**: Summarized conclusion and future perspectives highlights the significance of the findings and discusses the future perspectives of the projects presented herein.

Chapter 2. Background information

2.1. Cell Fate Portrayed from the Waddington's Landscape

Scientists have recently estimated the total number of cells to be 37 trillion cells in our body. Although based on age and sex, the number would vary, it is incredible how these cells concomitantly differentiate into more than 200 types of lineages in our body throughout our life to function uniquely at their niche. It is crucial that these committed cells grow and mature as designed. Otherwise, it results in devasting disorders or pathological conditions with the impaired or failed function of the tissue. Therefore, understanding the cell niche during cell development, regeneration, and healthy conditions offer how these environmental signals can engineer cell fate.

The phenomena of the cell-fate specification have been well conceptualized by Conrad Waddington for the first time as a Waddington's landscape, shown in Figure 3. He portrayed the normal development, differentiation, of a pluripotent stem cell as a ball rolling down from a slanted hilltop, which leads to varying landscapes of valleys to the end destination. During the ball dropping process, it can choose different pathways along the way to its final destination (terminally differentiated state), but its pathway could be different. Top to bottom illustrates the gradient of high to low pluripotency state of the cell (the ball). The addition of a robust fate-determining factor, such as lineage-instructive transcriptional factor, attracts the ball to the particular lineage. After the ball drops to such a stable location, it will not move elsewhere due to "epigenetic barriers" around it. This stable state represents an 'attractor state,' which is energetically stable that the ball will not move further unless its transcriptional activity is forced

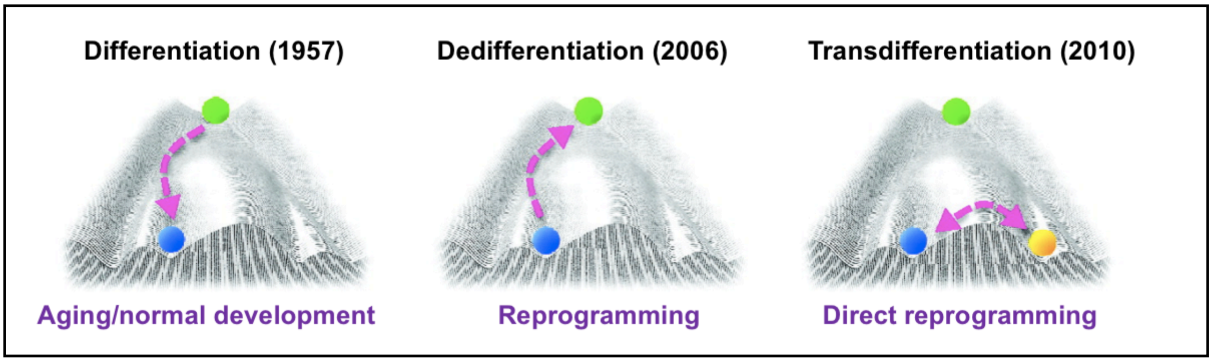

Figure 3. Illustration of the Waddington's Landscape on the 1) normal process of aging, 2) reprogramming, and the 3) direct reprogramming. Top green cell indicates the pluripotent stage of the cell, while blue and yellow indicate the differentiated cell states. Adapted from Takahashi's work (Takahashi, 2012).

to change by external factors. This phenomenon was first proved in 2006 by Yamanaka that the addition of four fate-changing transcription factors, known as OSKM (Oct-4, Sox2, Klf-4, and c-Myc), would revert the ball to the top of the hill, thereby conferring pluripotency to the somatic cells—reversing the aging. Their finding was evolutionary, and these factors were named as Yamanaka factors. Soon in 2010, these epigenetic barriers were proven to be overcome across the germ layer by a mixture of powerful lineage-instructive transcriptional factors. This was first demonstrated in fibroblast-to-myoblast conversion by overexpression *Myod1*(Davis, Weintraub, & Lassar, 1987). Feasibility to repurpose the cell fate via direct lineage conversion offered scientists to avoid the iPSC generation to obtain their target cell of interest, shortening the processing time and expenses immensely. Since then, various transcription factor cocktails (Ambasudhan *et al*., 2011; Caiazzo *et al*., 2011; Cao *et al*., 2016; Han *et al*., 2012; Vierbuchen *et al*., 2010) were identified to drive the lineage-specific direct reprogramming. Furthermore, in conjunction with these fate-changing transcription factors, researchers found the chemically-defined conditions which could further favor the lineage specification to the target fate upon adding soluble factors, such as epigenetic modulators (Ebrahimi, 2015; Zhang, Li, Laurent, & Ding, 2012).

In the later chapters, two strategies will be harnessed for guiding the cell fate of multipotent stem/progenitor cells and somatic cells by changing: 1) the intrinsic transcriptional network mediated by the CRISPR/Cas9; and by 2) exposing cells to the substrate-mediated biophysical cues along with the biochemical cues to epigenetically modulate the gene expression of the donor cells.

2.2. CRISPR/dCas9 System: The Ultimate Gene Editing Toolbox

For our first strategy, the clustered regularly interspaced short palindromic repeat (CRISPR)/CRISPR-associated Cas9 nucleases (CRISPR/Cas9) platform was utilized for genetically modulating the cell fate. Initially, this system was discovered from the defense system of bacteria and archaea. This adaptive immune system relies on the sequence-specific recognition of the single-stranded RNAs to inactivate the complementary sequence found in the invading foreign genetic elements (viral or plasmid DNA), functionally silencing them by inducing double-strand breaks. The sequence information of the foreign invaders gets stored as pre-crRNA (pre-CRISPR RNA) by prokaryotes in the CRISPR loci when the phages attack the foreign sequence. Later, a mature version of this sequence information is used to target the genome loci for complementary base pairing, which leads to cleavage and disruption of the target gene expression. Transactivating crRNA (tracrRNA) is also transcribed by CRISPR loci, which gets hybridized to crRNA, transcribed by RNase polymerase III. The crRNA-tracrRNA dual-RNA guided system has been engineered into a single guide RNA (sgRNA) for sequence-specific Cas9-mediated gene editing (Jinek *et al.*, 2012). Throughout our project, sgRNA will be referred to as gRNA.

Among many Cas9 variants, in our study, bacterial type II CRISPR/Cas9 system from *Streptococcus pyogenes* (SpCas9) was engineered to inactivate the catalytical nucleases by two-point mutations at D10A and H840A (Qi *et al.,* 2013). The new version of catalytically-deficient/dead form of dCas9 is widely used for regulating gene expression, neither replacing the DNA sequence nor causing insertional mutagenesis. For our approach, as shown in Figure 4, dCas9 is further engineered by dual tethering VP64 activation domains at both N'- and C'-terminus of dCas9. VP64 activation domain is composed of four tandem repeats of herpes

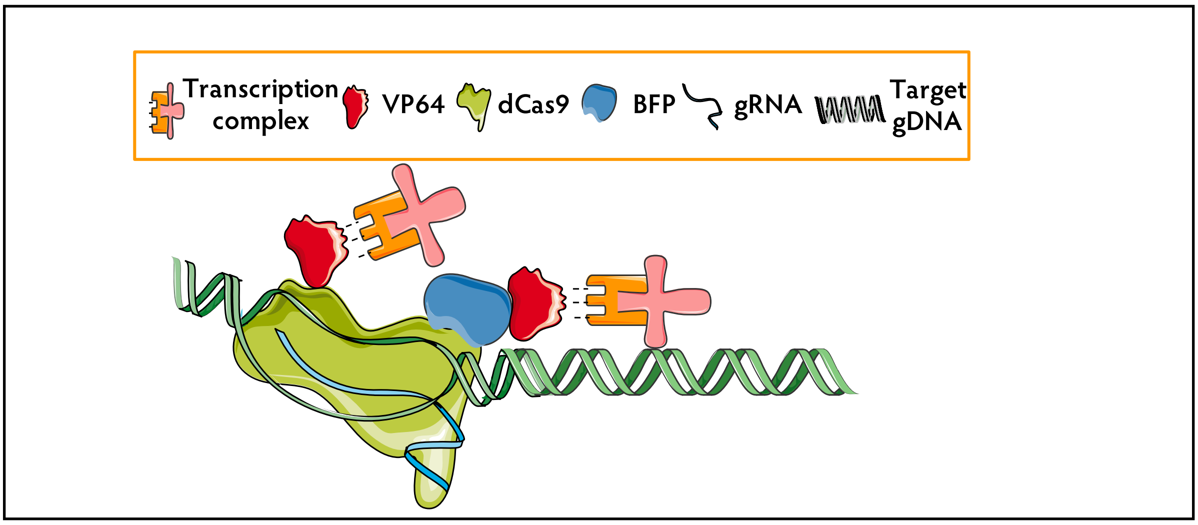

Figure 4. Components of CRISPR/dCas9 system with BFP as a reporter gene, including: 1) the target genomic DNA (gDNA), 2) deactivated Cas9 protein tethered with two VP64 activator domains and 3) chimeric gRNA which guides the dCas9 protein to the target DNA strand for the activation of an endogenous target gene.

simplex viral protein 16 (VP16). VP64 allows transactivation of the endogenous target once another protein domain can bind near the target's promoter. The designed gRNAs, which gets recruited to the target gene loci, shares the sequence information as 5' end -N_{20}-3'end where 'N_{20}' refers to any base sequence in 20 nucleotide (nt) length. This sequence should be complementary to the target sequence, immediately followed by 'NGG,' known as the protospacer-adjacent motif (PAM). PAM sequence allows Cas9 binding to excise 3-4 nt upstream of PAM. This moderate qualification for targeting any organism confers efficient and simple epigenome editing.

2.3. Microenvironmental Effects on Cell Fate Determination

Engineering the microenvironmental signals exposed to cells can affect cell behavior and phenotypes. Cells react to these cues by their cytoskeletal machinery, including intermediate filaments and actin stress fibers. There are the interconnected filaments that link the cell membrane and nucleus from distance to allow efficient and rapid force propagation when cells receive biophysical cues from their microenvironments. Upon transducing concerted signal to nucleus, the gene expression profiles can be altered by chromatin and nuclear lamina (lamins A, B, and C) remodeling, or by the recruitment of epigenetic modulators, which can permit the delivery of transcription factors to the nucleus (Crowder *et al*., 2016; Wang *et al.*, 2009). It is becoming more apparent that the forces—transmitted from the mechanical signaling between the cytoskeleton and the extracellular matrix/substrate—exerted on the nucleus may contribute to the changes in cell shape, growth, and development (Wang *et al.*, 2009; Iskratsch *et al*. 2014; Missirlis, 2016).

For our second strategy, we focus on engineering the microenvironmental stimuli (as shown in Figure 5, inspired by the cell's niche environment as an indirect method of providing a *milieu* of lineage-specific biochemical factors and physical cues. Schofield first postulated the concept of niche as a site that stem cells reside and contribute to the maintenance and self-renewal of neighboring stem cells (Schofield, 1978). Cells are exposed and influenced by various internal and external stimuli, thereby restoring cellular homeostasis or adapting to an altered entity by changing their morphology and gene expressions (Milisav, 2011). For example, metaplasia is a natural adaptive response in the intestine where reversible transformation occurs from an undifferentiated stem/progenitor cell type to another tissue-specific stem/progenitor cells, absent from that same tissue. This cellular adaptation response is triggered by abnormal microenvironmental stimuli, including the change in pH and hormone levels, or an attack from microorganisms (Slack, 2007) as a defense mechanism of cells to produce a repertoire of that transformed tissue.

2.3.1. Soluble factors: growth factors and epigenetic modulators

Utilizing a soluble factor approach for modulating epigenetic signatures of cells offers a safe, rapid, and cost-effective strategy that may allow the full realization of generating therapeutic cells. The clinical translation of conventional transgenic approaches has been hampered due to low efficiency and the risk of viral vectors integrating to the host genome. Therefore, as an alternative approach, small molecule-based lineage conversion would be advantageous as it is non-immunogenic, stable, rapid, cell-permeable, and easy to standardize. Moreover, it allows dose-dependent fine-tuning by modulating the concentration and length of exposure to cells (Ye *et al*., 2016). Because of these advantages, such a strategy could potentially be translated into therapeutic applications (Yu *et al*., 2014). Chemical cocktails can also either activate or inhibit key developmental signaling cascades for global gene alterations, which can be tailored to yield a more permissive microenvironment for cells to specify cell fate (Downing *et al*., 2013).For example, valproic acid is used to induce histone acetylation and reduce epigenetic memory of the donor cell, possibly by activating silenced regulatory gene networks necessary for lineage reprogramming (Kim *et al*., 2010; Vierbuchen & Wernig, 2012). Epigenetic modulators have been shown to enhance the reprogramming efficiency and include transforming growth factor-β inhibitors and Rho-associated kinase inhibitors, which facilitate the mesenchymal-to-epithelial transition (MET) program (Ichida *et al*., 2009).

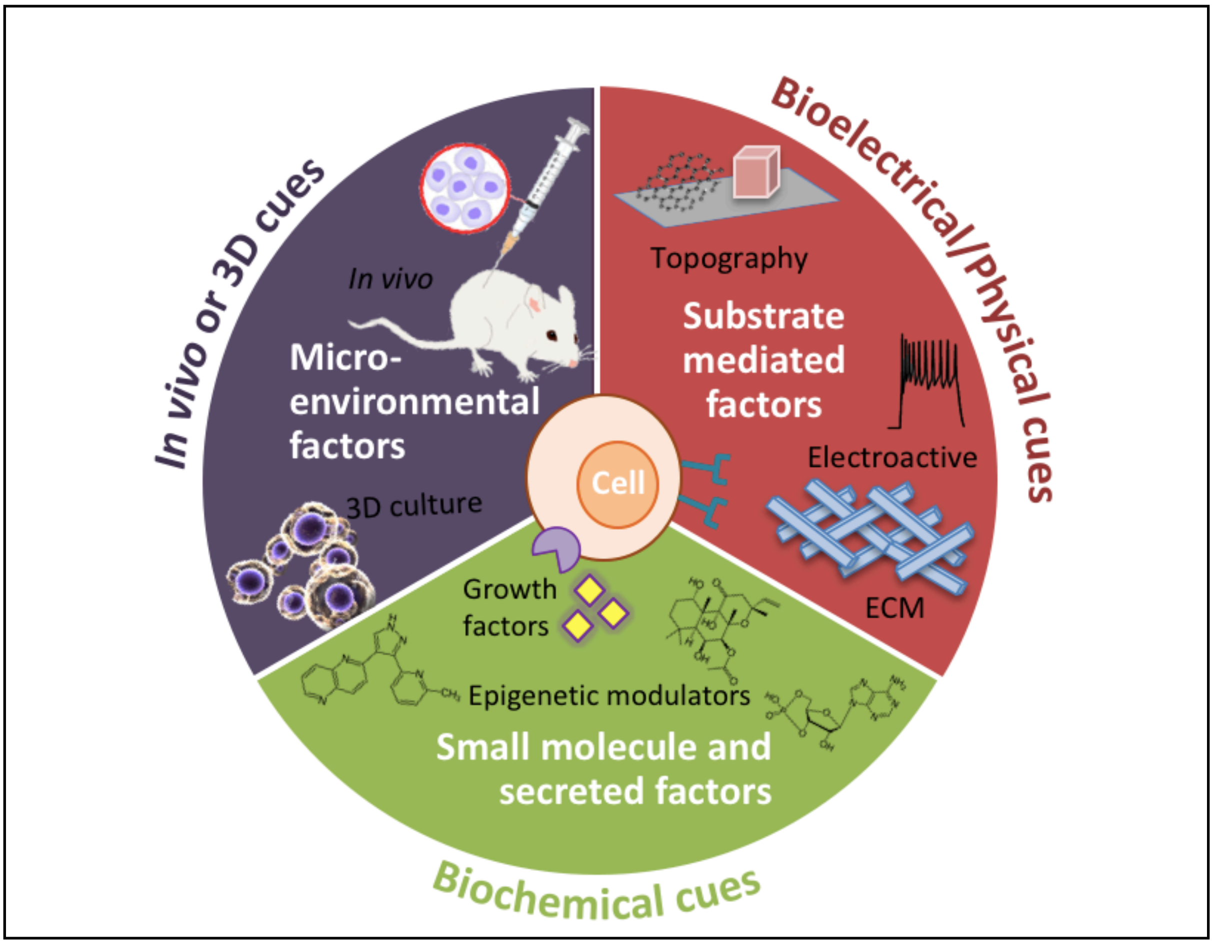

Figure 5. Summarized microenvironmental cues employed in this thesis topic for guiding the cell fate in skeletomuscular and neuronal systems: 1) *In vivo* or 3D cues mimicking the niche-environment of the target cell type; 2) substrate-mediated bioelectrical/physical cues including the topography and ECM compositions; and 3) biochemical cues activated by the addition of growth factors and small molecules.

2.3.2. Substrate-medicated insoluble factors

Along with the soluble factors, engineered biomaterials can exert multiple stimuli on cells, based on the substrate features (roughness, topography, and chemical compositions). Collective signals from the substrate affect cell's mechanotransduction, epigenetic modifications, and MET by their physical network with nucleus and chromatin structure, which finally influence reprogramming by the post-transcriptional (epigenetic) processes (Sia, Yu, Srivastava, & Li, 2016). Moreover, *in vivo*, cells continuously adapt to dynamic microenvironments, including topographical features from neighboring cells, their secreted extracellular matrix (ECM) proteins, and soluble factors ranging from nutrients to hormones (Iskratsch, Wolfenson, & Sheetz, 2014). Based on these tailorable signals, material scientists have attempted to augment cell fate conversion by modulating the spatiotemporal stimuli experienced by cells (cell-substrate and cell-cell interactions and the paracrine effect) as described in Figure 6. Among various strategies to portray niche-like microenvironments in the *in vitro* culture platform, herein, we would only limit our discussion to 4 cell fate modulation strategies: 1) physical cues (regulated by substrate topography and elasticity), 2) biochemical cues from ECM-like adhesive coatings, 3) electrical cues, and 4) three-dimensional cues.

2.3.2.1. Physical cues

Topographical cues enable the modulation of cell's physical confinement (both in nano- and micro-scales) where cells can mechanosense and artificially align themselves to activate intricate signal transduction pathways and subsequently facilitate lineage transitions (Costa, Lee, & Holmes, 2003; Downing et al., 2013; D.-H. Kim et al., 2010a; Kulangara et al., 2014; Yim, Pang, & Leong, 2007; Yoo et al., 2015). For instance, aligned substrates promote the differentiation of mesenchymal stem cells to neurons (Yim, Pang, & Leong, 2007) and the conversion of fibroblasts to neuronal lineages (Kulangara *et al*., 2014; Yim, Pang, & Leong, 2007). These processes are possibly triggered by force transmitted from the mechanical signaling between the cell's cytoskeleton and substrate, deforming the nucleus and rearranging the cytoskeleton (Iskratsch, Wolfenson, & Sheetz, 2014; Missirlis, 2016; Wang, Tytell, & Ingber, 2009). The role of patterned substrates not only enhanced the branched morphology of neurons, but also promoted the mechanical and electrical signal propagation in the cardiac systems (Costa et al., 2003; D.-H. Kim et al., 2010a). Remarkably, a few studies highlight the change of epigenetic landscape by enhancing histone acetylation for promoting mature cardiac differentiation (Morez *et al*., 2015) and somatic cell reprogramming to iPSCs (Downing *et al*., 2013), obviating the need of chemical compounds. In another study, transducing MEF with Ascl1, Pitx3, Nurr1, and Lmx1a on a patterned nanogroove enhanced the direct reprogramming efficiency to functional DA neurons via MET-mediated histone methylation (Yoo *et al*., 2015). The nanotopography spontaneously polarized the cell morphology to develop mature DA neuronal markers and increase neurite branches. Taken together, these findings address the importance of topographical cues on cell fate outcomes by modulating the epigenetic signature. Besides the topography of the substrate, its rigidity/elasticity has also been controlled to guide the cell fate commitment. The pioneering work from Engler and his colleagues first evaluated the role of matrix elasticity on the human MSC fate commitment. Their findings indicated that MSCs exhibited more neurogenic, myogenic and osteogenic potentials when cells were cultured on a soft matrix (0.1-1 kPa in elastic modulus), a medium stiffness matrix (8-17 kPa), and on a rigid matrix (25-40 kPa), respectively (Engler, Sen, Sweeney, & Discher, 2006). Along with their seminal work, later works also confirmed that the stiffness of matrix can provide potent physical cues at the cell-substrate interface leading to dynamic change in cytoskeletal network and consequent signaling pathways to influence cell morphology,

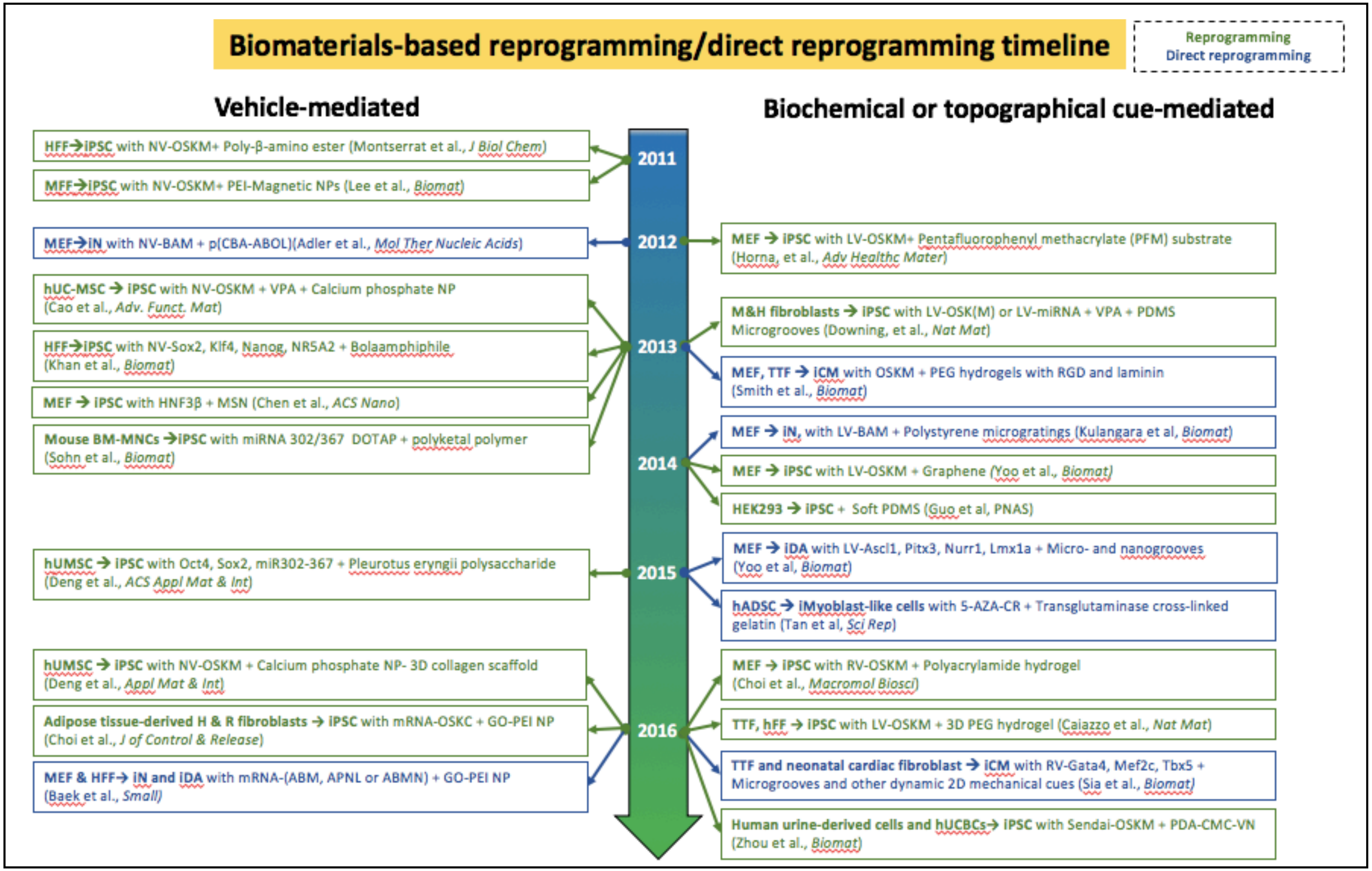

Figure 6. Summarized timeline for biomaterial-mediated cell fate change studies.

differentiation, and maintenance (Engler, Sen, Sweeney, & Discher, 2006; Gilbert et al., 2010; Missirlis, 2016; “Tensional homeostasis and the malignant phenotype,” 2005). The correlation between the substrate stiffness and reprogramming efficiency of MEF cells to iPSCs was confirmed recently by Choi *et al.* Upon using a 0.1 kPa soft polyacrylamide hydrogel, more Oct4+ and Sox2+ cells were expressed with higher alkaline phosphatase^{+}(AP^{+}) colonies compared those cultured on a stiffer (20 kPa) gel via induction of MET (Choi *et al.*, 2016). On the other hand, interestingly, without adding any ectopic transcription factors, Guo et al. first demonstrated that soft PDMS substrate alone could retain dedifferentiation of HEK-293 cells into stem-like cells by forming the embryoid body and exhibiting AP activity via increasing the local actin forces (Paszek et al., 2005). A similar study was done by Tan and colleagues who investigated the effects of matrix rigidities on direct reprogramming of adipose-derived stromal cells (ADSCs) to myoblast-like cells (Tan *et al.*, 2015). With the help of epigenetic modulator, 5-Aza-CR, they developed a 3D tunable transglutaminase cross-linked gelatin (Col-Tgel) system, which can load the chemical stimuli as well as deliver seeded cells for effective transplantation of cells *in vivo*. It was found that 5-Aza-CR sensitized the cells in response to the mechanical microenvironment and the medium stiffness (~15 kPa) of Col-Tgel offered the significant myogenic potential of cultured ADSCs both *in vitro* and *in vivo*. This matrix stiffness mimics the niche of the striated muscles (~8-17 kPa) (Engler *et al.*, 2004). After 14 days of cell transplantation with Col-Tgel scaffold and 5-Aza-CR upon muscle injury, more newly formed muscle fibers with less fibrosis were found compared to the ones without the scaffold or the epigenetic modulator. These results suggested that microenvironmental cues, transmitted from ECM to cells, can epigenetically modulate cell fate and plasticity to promote functional tissue regeneration. Collectively, these data highlight the critical role of substrate-mediated mechanotaxis on stemness retention and cellular reprogramming by explicitly triggering cell shape changes comparable to those using different soluble ligands and factors.

ECM, comprised of various cell-secreted factors, plays a critical role in stem cell niche; it regulates cell function (proliferation and differentiation) and phenotype by supporting cell structure and adhesion to the substrate (Kenry, Lee, Loh, & Lim, 2018). Therefore, coating plays a vital role in cell proliferation and differentiation, as well as improving the substrate's biocompatibility (Tong, Bohm, & Song, 2013). Cell interacts with different types of ECM to trigger downstream signaling pathway, which leads to different cell behaviors, including cell migration, self-renewal, and differentiation (Watt & Huck, 2013). Various bioactive polymer substrates have been developed using different surface modification techniques and subsequent immobilization of target ligand motifs. Using this approach, Horna *et al.* observed 8.5-fold higher number of iPSC-like colonies upon modifying polystyrene surface with pentafluorophenyl methacrylate (PFM) to subsequently tether OSKM encoding lentiviral particles, compared to the standard viral transduction method for murine embryonic fibroblasts (MEF) (Horna et al., 2012). The reactive ester groups from PFM endowed the covalent binding with the amino groups of peptides and proteins, resulting in nearly 100% GFP transduction efficiency after 6 hrs of exposure to the tethered infective particles. Likewise, Amanda and her colleagues developed RGD peptide and laminin(LM)-decorated poly(ethylene glycol)(PEG) hydrogel, which yielded nearly twice as productive reprogramming efficiency as using Matrigel for reprogramming cardiomyocyte-like cells from mouse fibroblasts (Smith *et al.*, 2013). Similarly, Zhou *et al.* utilized vitronectin peptide grafted polydopamine-based substrate for reprogramming human umbilical cord-derived cells and urine-derived cells to iPSCs using Sendai viral plasmids (Zhou *et al.*, 2016). The proliferation and pluripotency of hiPSCs were not only comparable to the results of Matrigel, but also implementing the xeno-free culture platform and non-integrating reprogramming factors offers a clinically more applicable system.

Throughout our study, to facilitate the differentiation of NSCs and transdifferentiation of fibroblasts on the hydrophobic graphene substrates, ECM proteins LM and fibronectin (FN) were used. LM has the RGD motif, which binds to cells through their integrin receptors and selected for its known contribution in neurogenesis, cell migration, axon guidance, and myelination (Forrest et al., 2009; Relucio, Menezes, Miyagoe-Suzuki, Takeda, & Colognato, 2012). Utilizing both adhesive proteins entail cells to strengthen their attachment by positive-reinforcement of secreting more ECM proteins.

2.3.2.2. Electrical cues

Electroactive substrates offer a suitable culture platform for excitable cells, such as neurons and skeletal muscle cells, for their inherent electrical activity. In this regard, highly conductive graphene and its derivatives offer a biocompatible and versatile platform with exceptional chemical, physical, and electrical properties. Graphene is defined as a single atomic layer of carbons arranged in a 2D hexagonal lattice network. Owing to its sp^2-hybridization and thin atomic thickness, graphene forms sp^2 hybrid orbitals with one s-orbital and two p_x- and p_y-orbitals. These hybrid orbitals in the XY plane lead to a single σ bond, while two π bonds form from the perpendicular p_z-orbitals. Therefore, graphene naturally renders a high electrical conductivity. With this feature, graphene-based substrates may contribute to both passive and active electrical stimulation of neighboring neurons, thereby supporting neuronal function and maturation (Park et al., 2011; Shah et al., 2014). Recent studies have demonstrated that graphene and its derivatives can play active roles in enhancing adhesion, proliferation, and differentiation of NSCs (Park et al., 2011; Shah et al., 2014; Yoo et al., 2014). Moreover, graphene enables facile functionalization with biomolecules like ECM proteins through covalent or non-covalent binding owing to its aromatic network (Kenry, Lee, Loh, & Lim, 2018). These unique characteristics brought motivation to use these materials for cell fate conversion. Yoo *et al.* first demonstrated graphene-mediated epigenetic reprogramming of MEF to iPSCs; inducing MET enriched the expression of the methylated histones and increased the occupancy of Oct4 and Nanog (Yoo *et al*., 2014). In another study, Shah *et al.* used the graphene oxide substrate for guided differentiation of rat NSCs to oligodendrocytes without the chemical inducers. Integrin-mediated signaling led to downstream regulation of focal adhesion kinase (FAK). FAK is the primary regulator of integrin-ECM signaling, where it mediates cytoskeletal remodeling and process extension during the development of oligodendrocytes (Forrest *et al*., 2009). Likewise, such a fate-guided conductive platform would be beneficial for the scale-up production of reprogrammed and differentiated cells.

2.3.2.3. 3D environmental cues

Engineered 3D cultural platforms have also been explored to provide physiologically relevant microenvironments to promote cell fate transition, which is unattainable in 2D culture systems. The 2D culture poses limitations in its ability to offer combinations of native milieu (biochemical and physical cues) to cells. Therefore, adherent cells result in a low number of differentiated populations by experiencing less cell-cell signaling and forming connective networks only in a lateral manner (Dingle et al., 2015; Pastrana, Silva-Vargas, & Doetsch, 2011). Moreover, culturing cells on a rigid culture plate, which is about several orders of gigapascal higher than the native brain tissue (ranging from 100 to 1000 Pa) (Elkin, Azeloglu, Costa, & Morrison, 2007) makes cells with native behaviors unattainable in a 2D system.

Several studies have successfully utilized the 3D culture platform to modulate cell fate. Noticeable morphological changes were observed when reprogrammed fibroblasts were encapsulated by 3D poly(ethylene glycol) (PEG)-based hydrogel and accompanied chromatin remodeling and MET transition, essential for initiation of reprogramming (Caiazzo et al., 2016). A similar approach was used for transdifferentiation of MSC to hepatospheres and Schwann cell-like cells using 3D poly(L-lactic acid)-*co*-poly(ε-caprolactone)/collagen nanofibrous scaffold and gelatin-based nerve conduit, respectively (Caiazzo et al., 2016; Uz et al., 2017), undersupplying the growth factors supporting the specific target lineages. When compared to the 2D culture platform, the specific hepatic gene expressions were significantly increased on a 3D nanofibrous scaffold, and the neurite lengths increased around 2.5-fold on 3D nerve conduit with a stiffness of $\sim 0.4 \times 10^6$ Pa. These 3D culture platforms may be a potential tool to quickly generate an adequate amount of target cells for further *in vivo* study by augmenting the transdifferentiation of MSCs. Likewise, the 3D culture platform yields high surface area and lacks the need for chemical dissociation for passaging the cells. This, in turn, preserves and maintains the native behaviors of cells and mimics the native physical environment by secreting their own ECM proteins. However, resulting in heterogeneous populations from the limited diffusional transport of oxygen and nutrients cause batch variations. Therefore, it is imperative to fabricate a 3D culture platform with additional features to synergize the environmental cues for its shortcomings to better simulate the niche-like environments. For our study, instead of utilizing the 3D culture platform, the host environment will be harnessed to mimic the stem niche environs of the skeletal myoblasts.

Chapter 3. *In situ* reprogramming of EPCs by transactivation of endogenous *MYOD1* using the CRISPR/dCas9 system

3.1. Rationale and Significance

In our previous work, *Myod1*—known as a master regulator for initiating the skeletal myogenesis (Weintraub et al., 1989)—was used as a transcriptional target to directly convert murine embryonic fibroblasts into skeletal myocytes (Chakraborty et al., 2014). The *Myod1*-mediated transdifferentiation supported the notion that direct cell fate conversion can be achieved by obviating the need of the intermediate pluripotent cell state through dedifferentiation and going through the normal development as depicted by the Waddington's landscape, described in **Chapter 2.** Background information.

The success of our previous work motivated us to follow-up with the studies presented in this Chapter. We aimed to extend the CRISPR/dCas9-mediated *MYOD1*-transactivation of the primary human origin as a cell source. For having high proliferation capability through clonal expansion, being easily accessible, and being a potential contributor for neovascularization and musculature regeneration, EPC was selected as our cell source. Besides, sharing the same mesoderm origin, cell fate conversion would be more useful for EPCs (J E Ferguson, Kelley, & Patterson, 2005) to skeletal myoblasts—having less epigenetic barriers to overcome (Hendry & Little, 2012).

For achieving inter-lineage conversion, an optimized genetic engineering tool was used for gain-of-function, as shown in Figure 7. For increasing the utility, codon-optimized and humanized CRISPR/dCas9, dual fused with VP64 transactivation domains, was used to target the transcriptional activation of *MYOD1*. Multiple gRNAs were designed to be recruited to the *MYOD1* loci, and co-delivery was further optimized depending on the most elevated target gene expression level. Moreover, the tetracycline-inducible expression system yielded temporal activation of the myogenesis program upon the administration of dox. All elements were co-delivered via lentivirus to establish the reprogrammable EPCs—transduced with CRISPR/dCas9, gRNAs, and m2rtTA.

To augment the therapeutic efficacy from the given number and volume of reprogrammable EPCs, we re-purposed our cells' fate to skeletal myoblasts. Instead of terminally differentiated cells, myoblasts, which self-renews would increase the chance of cell survival and engraftment. Besides, for enriching the CRISPR/dCas9-transduced EPCs to uniform cell populations, flow-assisted cell sorting (FACS)-mediated selection was performed based on its reporter gene, a blue fluorescent protein (BFP), expression. We posited that under the dynamic *in vivo* microenvironmental cues, these cells could reprogram *in situ* and promote the restoration of damaged muscles. *In situ* reprogramming is beneficial as implanted cells can generate target functional cells by interacting with the secreted soluble factors as well as the neighboring cells at the injury sites by recapitulating local microenvironmental conditions. Therefore, along with the type and condition of the neighboring cells, the microenvironmental cues at an injured region may critically determine the identity of reprogrammed cells and their regenerative capacity (Grande et al., 2013; Niu et al., 2013).

Collectively, dCas9-based endogenous transcriptional activation of the target gene allows cell-fate engineering, which mimics the natural development process to instruct stem/progenitor cells to differentiate unlike using the forced ectopic expression induced by transcription factor delivery. Herein, we induce transdifferentiation *in situ* in a native context to provide collective biochemical and physical signals from the niche-like environment *in vivo,* which cannot be provided from *in vitro.* With efficient and versatile features to modulate multiple target loci, dCas9-mediated cell-based therapy would provide broad clinical utility for treating various types of injuries and genetic diseases.

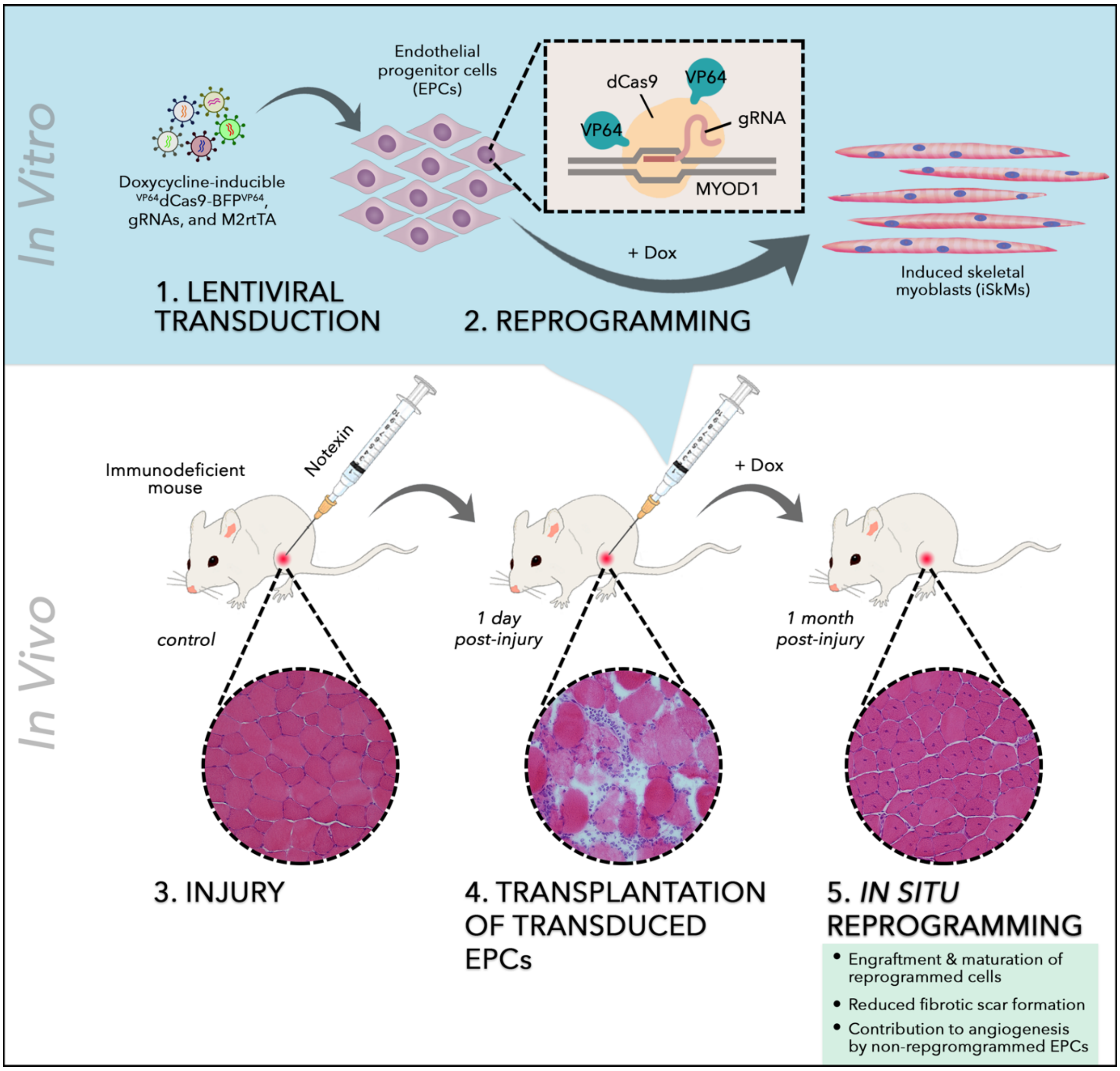

Figure 7. Graphical abstract of summarizing the findings of **Chapter 3. *In situ* reprogramming of EPCs by transactivation of endogenous *MYOD1* using the CRISPR/dCas9 system** for utilizing the *in vivo* microenvironmental cues to achieve *in situ* reprogramming of *MYOD1*-transactivated EPCs to restore the notexin-induced muscle injury.

3.2. Methods

3.2.1. Cell isolation and maintenance

3.2.1.1. Isolation and culture of EPCs from umbilical cord blood (UCB)

As shown in Figure 8, primary EPCs were enriched and populated from the PBMCs, isolated from the human UCB (New York Blood Center) using the well-established density gradient separation protocol (Mead, Prater, Yoder, & Ingram, 2008). Briefly, the day before isolation, a 6-well plate was coated with 1 ml of 50 µg/ml rat tail collagen I per well overnight at 37 °C. On the next day, Histopaque-1077 was used as a density gradient medium for the diluted UCB with Hank's Balanced Salt Solution (HBSS) at the 1:1 ratio. For the PBMC isolation, the diluted blood was slowly added to the Histopaque-1077 at an equal ratio and was centrifuged for 30 min at 740 g with no brake. Then, the PBMC layer from the buffy coat was collected after three rounds of washing steps with the EPC basal media at the ratio of 10:1, followed by the centrifugation for 10 min at 515 g with a high brake. After the final washing step, the PBMCs were resuspended in a fully supplemented culture media, EGM-2 (Lonza, CC-3162), and seeded on a pre-collagen-coated plate. The media was changed daily at the speed of 4-5 seconds/ml for the first week. Then, when the EPC colonies were observed between Day 4 and 14 (varied by the UCB batch), they were propagated accordingly with 0.05 % Trypsin/EDTA and trypsin neutralizing solution (TNS; Lonza) and re-plated on a collagen-coated plate at the density of 3000-5000 cells/cm^2 for further expansions. Throughout all the experiments, EPCs and transduced EPCs were maintained by replenishing EGM-2 media every two days. For freezing them, 40 % of FBS, 10 % of DMSO, and 50 % of media were used.

3.2.1.2. Human skeletal myoblast and iSkM expansion

The protocol for expanding human myoblast cells (Gibco, A12555) was adapted from (Darabi et al., 2012). Firstly, the flasks were coated with 0.1 % porcine gelatin and cells were seeded at the density of 5000 cells/cm^2. The media was replaced for every 2 days with a myogenic induction media, consisted of Iscove's Modified Dulbecco's Medium (IMDM; ThermoFisher Scientific, 12440053) with 15 % fetal bovine serum (FBS; Atlanta Biologicals), 10 % horse serum (HS; Sigma, H1138), 1 % chick embryo extract (Fisher Scientific, 100-163P/10), 50 μg/ml ascorbic acid (Sigma), 4.5 mM monothioglycerol, 10 μM Rho-associated, coiled-coil containing protein kinase (ROCK) inhibitor (for 24 hours; Stemgent, 04-0012-10), and gentamicin (ThermoFisher Scientific,15750060). During the reprogramming, a 1:1 ratio of EGM-2 media and muscle induction media was replenished with fresh 3 μg/ml of doxycycline (dox; Sigma, D3447) every other day. Muscle induction media was composed of DMEM with high glucose (DMEM-HG; ThermoFisher Scientific, 11960044), supplemented with 2 % HS, sodium pyruvate, GlutaMAX, penicillin/streptomycin (P/S), and β-mercaptoethanol. The same passaging method was used as EPC detachment.

3.2.2. Dox-inducible VdC9BV and gRNA designs and constructions

The *MYOD1* locus-specific gRNAs were designed *in silico* similarly as described previously (Chakraborty et al., 2014). Briefly, the UCSC genome browser tracks (Feng Zhang Lab, MIT) were utilized to target the genome within 1000 bases upstream of the *MYOD1* transcription starting site (TSS)—chr11:17,741,110-17,743,678. The following gRNA-targeted sites (from 5’ end to 3’ end) were used in this study:

- gRNA1(+strand chr11:17740194-17740213): TTGACTCAGCACCGCGAGTG - ~ 1000 bps from TSS
- gRNA2(-strand chr11:17740506-17740525): CCGAGACAAACGGGTCGTAG - ~ 600 bps from TSS
- gRNA3(+strand chr11:17740919-17740938): ACCTAGCGCGCACGCCAGTG - ~ 200

bps from TSS

- gRNA4(-strand chr11:17740903-17740922): AGGTCCCCTACCGGGCAGGG - ~ 200 bps from TSS
- gRNA5(+strand chr11:17740836-17740855): GAGGTTTGGAAAGGGCGTGC - ~ 250 bps from TSS

The gRNAs 1, 3, and 5 were selected to target the positive strand of the genome while gRNAs 2 and 4 were selected to target its opposite strand. Among 5 different candidates, the best combination (gRNAs 1, 2, and 4) was selected for the maximum activation of the endogenous *MYOD1* throughout the experiments.

For constructing ^{VP64}dCas9-BFP^{VP64}(VdC9BV), a humanized pdCas9-BFP plasmid was purchased from Addgene (#44247) for the insertional cassette. Two gBlock DNA fragments (Integrated DNA Technologies) were used to fuse dual VP64 transactivator domains: 1) N'-VP64, FLAG-tag, and a linker; and 2) VP64, FLAG-tag, and a nuclear localizing signal (NLS), and a linker. These fragments were cloned into a lentiviral Tet-O-FUW backbone (Addgene, #27152), encoding the tetracycline-inducible expression system, by a four-way ligation reaction. This fused Tet-O-FUW-VdC9BV plasmid was deposited and now available through Addgene (#62195). The insertional cassette of the genomic target sequences was synthesized with human U6 promoter as previously described (Mali *et al.*, 2013) in the form of the U6 promoter + 20 bp gRNA targets (5 sets of gRNAs) + 3 bp PAM sequence for the type II CRISPR system (NGG). The BsmBI restriction site was added to the distal end of the promoter to generate complementary sticky ends. Subsequently, these synthesized gBlocks were individually cloned into the FUGW lentiviral plasmid backbone (Addgene, #14883), double digested with PacI and XhoI to replace the ubiquitin (promoter)-GFP cassette. All ligation reactions were conducted with Q5 High Fidelity DNA polymerase (New England

Biolabs), and cloning primers to PCR amplify and purify the products using the Qiagen PCR purification kit.

3.2.3. Lentiviral production and transduction for engineering reprogrammable EPCs

As described previously (Chakraborty et al., 2014), lentiviral particles, transfected individually with the dox-inducible VdC9BV and M2rtTA, and each U6-gRNA candidate, were produced from HEK293T or HEK293T/17 (ATCC, CRL-11268) cells by the standard transfection method of calcium phosphate precipitation (SignaGen Laboratories, CalFectin™) using the second-generation lentiviral packaging plasmids: psPAX2 (Addgene, #12260) and pMD2.G (Addgene, #12259). Briefly, HEK293T cells were maintained using DMEM-HG, supplemented with 10 % FBS, GlutaMAX, sodium pyruvate, MEM non-essential amino acids (NEAA), and P/S. To transfect the plasmids of interest (VdC9BV, M2rtTA, and gRNA candidates), HEK cells were cultured on 0.1 % porcine gelatin-coated T-75 flasks (coating for at least an hour) to maintain a sheet of even HEK293T population. An hour before plasmid transfection, a sufficient amount of media was replenished to prevent serum starvation. In a T-75 flask, each plasmid of interest was prepared for lentiviral packaging by diluting 9.5 µg of the plasmid of interest, 3.3 µg of PMD2.G and 6.2 µg of psPAX2 into 625 µl of DMEM-HG basal media. Likewise, 58.5 µl of CalFectin was diluted with 625 µl of DMEM-HG. Diluted CalFectin was added to diluted plasmids mix and incubated for 15 min at room temperature (RT) after rigorous vortexing to be added to each flask drop by drop. After 5 hours of incubation, fresh media was replenished to remove calcium residues from the media and media was collected in three consecutive days, starting from 28 hours post-transfection. Collected lentiviral supernatant was centrifuged at 1000 rpm for 5 mins at 4 °C for removing cell debris. Subsequently, the supernatant was filtered by a 0.45 µm-filter and a Luer-lock syringe and concentrated (up to 50 times) with Amicon Ultra-15 centrifugal filter unit (MilliporeSigma, UFC910024) at the speed of 3400 rpm for 20 mins at 4 °C. Concentrated virus was aliquoted and stored at -80°C until future use.

For assessing the viral titer, qPCR Lentivirus Titration Kit (Abm, LV900) was used by following the manufacturer's procedure to detect the signal based on the 5'LTR region of the lentiviral plasmid backbone. Accordingly, the multiplicity of infection (MOI) was calculated based on optimized after 5 days post-transduction to improve its efficiency while not significantly affecting the cell viability. Based on the results, human EPCs were transduced one day after seeding with the viral concentrates (M2rtTA, VdC9BV, gRNA1 through 5) and 4 µg/ml of polybrene (Sigma) at the MOI of 40, 10, and 10 for VdC9BV, M2rtTA, and gRNAs, respectively. After a day, fresh media was supplied and cultured accordingly based on the analysis.

3.2.4. In vitro characterization of EPCs and enriched iSkMs

3.2.4.1. Immunophenotyping of isolated EPCs

The immunophenotypes of the isolated EPCs were confirmed by the FACS CantoII flow cytometer (BD Biosciences). The surface antigen markers and isotype controls were all purchased from BioLegend: human APC-CD31 (303115), human PE-CD144 (348505), human FITC-CD14 (325603), human PE-CD45 (304007), mouse PE-IgG1, κ (400111), mouse FITC-IgG1, κ (400109), mouse APC IgG1, κ (400119), and mouse PE IgG2a, κ (400213). For further validation, EPC characterization kit (Lonza) was also used to confirm the expressions of EPC markers, including anti-mouse CD31, anti-mouse CD146, anti-rabbit Flk-1, and anti-rabbit vWF by following the standard staining protocol. Briefly, it uses 4 % paraformaldehyde (PFA) to fix the cells, permeabilize cells using 0.2 % Triton X-100, blocking with 10 % goat serum (GS), and subsequently staining with the primary antibodies overnight and fluorescent-labeled secondary antibodies in the following day along with DAPI. Fluorescent images were all taken with Nikon TE2000 fluorescent microscope or Nikon A1 confocal laser microscope system using the NIS-Elements software.

3.2.4.2. gRNA optimization for promoting reprogramming efficiency

After transducing EPCs with VdC9BV and M2rtTA, cells were infected with various combinations of gRNAs with 5 days of dox induction for analyzing the gene expression using qRT-PCR and RT-PCR. Eleven combinations were tested against the negative control, EPC ectopically forced to express murine *Myod1* transcription factor. To conduct qRT-PCR, RNeasy Mini Kit (Qiagen, 74104), iScript cDNA synthesis kit (BioRad), and SYBR green chemistry (BioRad, 172-5272) were utilized. The optimized gRNA mix (as designed from *3.2.2.*) was selected based on the highest endogenous *MYOD1* expression level relative to the control using the $2^{-\Delta\Delta CT}$ method. The primer sets used for endogenous *MYOD1* were: CTTTGCTATCTACAGCCGGG (forward) and GAGTGCTCTTCGGGTTTCAG (reverse); and GGAGCGAGATCCCTCCAAAAT (forward) and GGCTGTTGTCATACTTCTCATGG (reverse) for GAPDH (throughout **Chapter 3.** *In situ* reprogramming of EPCs by transactivation of endogenous *MYOD1* using the CRISPR/dCas9 system and **Chapter** 4. Enhancing the neural cell fate commitment by deploying biochemical cues and substrate-mediated electrophysical cues studies). Upon optimizing the gRNA combinations, primers in Table 1 were used for RT-PCR analysis for testing the profiles of the myogenic regulatory factors after 5 days of dox-added iSkMs compared to control (transduced EPCs in the absence of gRNA cocktails) where GAPDH was used as a reference gene for normalization.

3.2.4.3. Evaluation of the flow-assisted cell sorting-mediated selection of iSkMs

After optimizing the gRNA cocktail targeting the locus of endogenous *MYOD1*, to further promote the reprogramming efficiency, FACS was utilized for selecting the VdC9BV and M2rtTA transduced EPCs. After 5 days of dox induction, transduced EPCs were sorted by the expression of BFP using the BD Influx^{TM} cell sorter (BD Biosciences). This was followed by subsequent transduction of gRNA cocktails and proliferated up to passage 13 for all the *in vitro* and *in vivo* experiments. Transduced cells were cultured with fresh dox in the low serum differentiation media every other day up to a month for examining the reprogramming potential to develop iSkMs.

After establishing reprogrammable EPCs—transduced with VdC9BV, M2rtTA, and gRNA combinations—, their reprogramming efficiency was analyzed by immunostaining the reporter genes encoded by VdC9BV. iSkMs were induced for 7 days and stained with FLAG (Cell Signaling Technology; 14793S) to identify its co-expression with DAPI. A total number of %FLAG^{+} cells were analyzed using ImageJ. After another week of dox induction, MYOD1 (Pierce; MA1-41017; 1:50) and BFP expression was evaluated compared to the original EPC using FACS CantoII and FACS AriaII™ flow cytometer (BD Biosciences), respectively. All the FACS data analysis was performed using FlowJo (Tree Star) and Microsoft Excel.

Expression of the lineage-specific mature marker was additionally assessed for a long-term *in vitro* induction in the presence of dox. iSkMs were stained with muscle-specific marker, MHC (Developmental Studies Hybridoma Bank, MF20; 1:100) and MYOD1, and EPC marker, anti-rabbit vWF (Dako, A0082; 1:200) both in the absence and presence of dox. The gene expression level of iSkMs was also compared with other cell types, including EPC control (negative control) and human skeletal myoblasts (positive control). Primers used for the long-term *in vitro* the direct reprogramming of EPC were shown in Table 2 and as a reference gene, 18s rRNA was used for normalization.

Table 1. List of primers for verifying the optimized gRNA cocktails

GAPDH	Forward: GGAGCGAGATCCCTCCAAAAT
	Reverse: GGCTGTTGTCATACTTCTCATGG
TNNC1	Forward: ACCTCTTCCGCATGTTTGAC
	Reverse: GACTCAGCTGGAGTTGGAGG
MYOD1	Forward: CTTTGCTATCTACAGCCGGG
	Reverse: GAGTGCTCTTCGGGTTTCAG
ENO3	Forward: TGACTTCAAGTCGCCTGATGATCCC
	Reverse: GCGTCCAGCAAAGATTGCCTTGTC
DES	Forward: CCTACTCTGCCCTCAACTTC
	Reverse: AGTATCCCAACACCCTGCTC
MYH1	Forward: ATAGGAACACCCAAGCCATC
	Reverse: TTTGCGTAGACCCTTGACAG

Table 2. List of primers to characterize iSkMs

18s rRNA	Forward: CGGCTACATCCAAGGAA
	Reverse: GCTGGAATTACCGCGGCT
CD31	Forward: ATTGCAGTGGTTATCATCGGAGTG
	Reverse: CTCGTTGTTGGAGTTCAGAAGTGG
CD105	Forward: ACGCTCCCTCTGGCTGTTG
	Reverse: GCCCTTCGAGACCTGGCTAG
MYOD1	Forward: CTTTGCTATCTACAGCCGGG
	Reverse: GAGTGCTCTTCGGGTTTCAG
dCas9	Forward: AGGGATTAAGGAGCTCGGGT
	Reverse: AGGAAGCTCTGAGGGACGAT
DESMIN	Forward: GAAGCTGCTGGAGGGAGAG
	Reverse: ATGGACCTCAGAACCCCTTT
TNNT1	Forward: ACCTGGTCAAGGCAGAACAG
	Reverse: CTGTGATGGAGGCAGCCAG
MYH2	Forward: TCTCCAAAGCCAAGGGAAACC
	Reverse: AACTGAGACACCAGAGCTTCC

3.2.1.1. *RNA-Seq analysis*

The library and genomic mapping were done from the Columbia genome center upon submitting the triplicate samples of isolated total RNA from human myoblasts, EPCs, and 5-day dox-induced iSkMs. The Venn diagram was prepared based on the differential gene expression profile between the experimental groups against the donor cell, performed with DESeq2 using the counts files obtained from genomic mapping. Utilizing these results of the differential expression analysis, we performed a gene ontology analysis to determine which gene ontologies were altered in each experimental group as compared to the original undifferentiated cells. The normalized enrichment score (NES), nominal *P*-value, and false discovery rate (FDR) were indicated in each enrichment plot.

3.2.2. *Animal care and cell transplantation*

3.2.2.1. *Breeding and validation of the immunodeficient NOD scid mice model*

In vivo study was conducted following the animal care and experimental guidelines approved by the committee at Dankook University (DKU), Korea. Followed by the protocol (#15-047), all animals were bred and housed in a level 2 biosafety animal facility with a specific pathogen-free environment, and they received food and water *ad libitum*.

Total 4 male and 17 female NOD.CB17-$Prkdc^{scid}$/J (NOD *scid*) mice were purchased from JAX (#001303) at the age of week 6. They were mated at the ratio of 1:3 or 1:4 (male: female) per cage for a week. After a week, male mice were isolated from the female mice for a week to verify their pregnancy. Once the mouse was pregnant, it was separated from other mice until her offspring reached 4-weeks-old and segregated based on their identified sex. After isolating pups from their mothers, mothers were not mated for a month to provide them a break. The mating process started at the female age of week 7, repeated only twice in their lifetime, and sacrificed as they aged. Each mouse was traced by the ear tag and cage number to prevent the inbreeding, leading to a genetic defect or premature death of the animal. Each cage supported up to 5 female or 4 male mice and bedding was replaced twice a week. Following this inhouse breeding schedule, all experiments were conducted with 8- to 12-week-old female mice (up to F3 generations) for having less complement activity (Shultz et al., 1995) and a lower rate of myogenesis than male mice (Manzano *et al.,* 2011).

To test the feasibility of the injection protocol and the 2-week xenograft study, a preliminary study was conducted with 0.5 million transduced EPCs (suspended in 15 µl of saline), injected into the right hindlimb while saline was injected into the opposite intact tibialis anterior (TA) muscle ($n = 3$). Cell injection protocol and immunostaining analysis of the cryosectioned-muscles were followed, as explained below in detail (*3.2.5.3.* and *3.2.6.,* respectively). Based on these preliminary results, to further increase the survivability and engraftment efficiency of the injected cells, the cell number was increased to 1 million, and the affected lesion site within the myofibers was enlarged by insulting the muscle with systemic injection of myotoxin.

3.2.2.2. Establishment of the myotoxin-induced skeletal muscle injury in vivo model

For the muscle injury model, two different myotoxins were tested following the same injection protocol. Mice were anesthetized by the inhalation of 1-5 % isoflurane/O_2. For injecting myotoxins, a 26.5-gauge syringe was used for the injection at the speed of 20 µl/min. Either 50 µl of 0.5 % bupivacaine (Tokyo Chemical Industry, B3925) or 50 µl of 2 µg/ml Notexin (Latoxan, L8104) was diluted in saline and injected *i.m.* at both sides of the TA muscle.

3.2.2.3. Cell transplantation

A day after myotoxin injection, 1 million cells (suspended in 15 µl of saline) of either transduced EPCs or human myoblasts were injected *i.m.* along the length of TA muscle to evaluate their *in vivo* therapeutic potentials (engraftment and maturation into skeletal myotubes). All mice were anesthetized as mentioned above and all cell injections were conducted with the 33-gauge Hamilton syringe concurrently with needle withdrawal at the speed of 2 µl/min. A needle was initially injected into the lower end of the TA muscle and longitudinally pushed through until 3 mm below the proximal end of the tendon. Then, the syringe was pushed across the muscle as it was withdrawn. One or both legs were injected with either cells or saline (for the control group). Total groups were: 1) saline-injected group as a negative control; 2) human myoblasts-injected group as a positive control ($n = 6$); 3) transduced EPC-injected group with dox as a treatment group ($n = 8$); and 4) transduced EPC-injected group without dox as a control ($n = 8$). For a month, either 7.5 % sucrose water with or without dox was given to the reprogramming and control groups, respectively. Both types of water were replenished twice a week.

3.2.3. TA muscle isolation and analyses

3.2.3.1. Muscle extraction and cryosectioning process for preparing histological analyses

TA muscles were harvested 4 weeks after cell injections and the mice were euthanized by CO_2 inhalation as a primary method followed by cervical dislocation. Collected TA muscles were all processed by snap-freezing them in liquid nitrogen-cooled 2-methylbutane (Sigma) for 3 seconds and storing in -20 °C for cryosection, or in liquid nitrogen for RNA extraction later. For cryosection, one-thirds of the TA muscle was perpendicularly embedded into the O.C.T. compound (Sakura® Finetek) and sliced immediately without fixing the muscle. The cryostat (Leica) was used to obtain 10 µm transverse muscle sections serially at -25 °C. Each cryosection was mounted on silane-coated glass slides for further histology and immunocytochemistry analyses.

3.2.3.2. Morphometric evaluation of the fibrosis, myogenesis, and myofiber regeneration

Prepared cryosections were stained with Hematoxylin and Eosin (H&E) and Sirius red (Abcam, ab15068) for the histological assessments and quantification of fibrosis followed by the manufacturer's protocol. Hematoxylin stains for the nuclei and chromatin (in blue/violet and dark blue/black, respectively) and Eosin stains for the cytoplasm, muscle fibers, and red blood cells (in pink, deep pinky red, and in red, respectively). Sirius red stain intercalates into the protein structure of collagen (types I and III) fibrils in red and stains muscle fibers and cytoplasm in yellow.

For evaluation of the fiber number and total fiber area, average fiber size (obtained by fiber number divided by the total fiber area) and %regenerative fibers (obtained by counting the percentage of the centronucleated myofibers amongst total fiber numbers), three nonconsecutive sections of H&E stained slides were selected and images were taken at three random microscopic fields (200X) per muscle. As myofiber shapes were not in a perfect circle, instead of measuring the wider diameter size of the myofibers as other previous studies quantified, myofiber area was estimated. Such quantification was performed by drawing individual fibers with the drawing pad pen and going through multiple rounds of threshold and masking tools to exclude void areas and blood vessels using the programmed Image J macros. All the fibers at the edges were excluded for both counting and area measurements. Similarly, for quantifying the %area of fibrosis, 2-3 microscopic fields (100X) were randomly selected and analyzed by quantifying the percentage of the deposited collagen fiber (in red) over the total myofiber area (in yellow). All image analyses were taken with the bright-field microscopy and conducted with 3 biological replicates analyzed by Image J and Wacom drawing pad

(CTH-470) to set the boundary of myofibers for the morphometric evaluation.

3.2.3.3. Immunofluorescent staining for cryosectioned-muscle tissues

Tissues mounted on silane-coated glass slides were fixed in 4 % PFA for 10 mins at RT, rinsed with PBS for 5 min. Next, glass slides were applied with rubber cement to prevent the overflowing of liquids during the staining process. In addition to the normal staining procedure, to reduce the background autofluorescence of the cryosectioned-muscle tissues, they were incubated with 0.4 % pepsin (in 10 mM HCl) for 10 min at RT. Then, the tissue was permeabilized with 0.3 % Triton X, rinsed with PBS twice for 5 min, blocked with 2 % normal GS for 1 hr at RT, and stained with primary antibodies at 4 °C overnight followed by the staining of secondary antibodies and DAPI the next day. The primary antibodies used are anti-rabbit FLAG (Cell Signaling Technology, 14793S; 1:400), anti-mouse human nucleus (hNu; MilliporeSigma, MAB1281; 1:100), and anti-rat laminin (Abcam, Ab2466; 1:50). The secondary antibody (1:200) used were all purchased from ThermoFisher Scientific: Alexa Fluor 488 goat anti-mouse/rabbit IgG (A-11001/A-11008), Alexa Fluor 594 goat anti-rabbit/mouse IgG (A-11037/ A-11032), and Alexa Fluor 647 goat anti-rabbit IgG (A-21245).

For evaluating the contribution of non-reprogrammed EPCs on neoangiogenesis, muscle cryosections were additionally stained with the endothelial cell markers, anti-mouse CD31 (Santa Cruz; SC1506; 1:200) and anti-rabbit vWF. The percent or area density of capillary was quantification by measuring the total number of cells or the cross-sectional area (mm^2) occupied by the numbers of $CD31^+$ or vWF^+ cells using Image J. Total 4 random microscopic fields (200X) were enumerated to analyze the data.

3.2.4. Statistical analysis

All analyzed data were represented as the mean ± standard deviations (stdev), and statistical analyses were performed by a two-tailed unpaired student *t-test* for the comparisons between two groups. For comparing multiple groups, either one-way or two-way analysis of variance (ANOVA) was used with the *post hoc* analysis of Tukey's or Sidak's multiple comparison tests, respectively, using GraphPad Prism 6. Statistical significance was denoted as: * for $p < 0.05$, ** or ++ for $p < 0.01$, *** or +++ for $p < 0.001$, and **** or ++++ for $p < 0.0001$.

3.3. Results and Discussion

3.3.1. Isolation and characterization of EPCs from UCB

The UCB was used as a systemic source of primary human EPCs using the density gradient separation protocol, as depicted in Figure 8 and characterized by immunophenotyping. Based on this result, it was confirmed that the isolated EPCs express EPC lineage-specific markers, including CD31, CD144, CD145, Flk-1, and vWF, while not expressing CD45 and CD14 (Figure 9)(Mead, 2008).

3.3.2. Constructing dox-inducible VdC9BV and gRNAs to engineer reprogrammable EPCs

Lentivirus, encoding ^{VP64}dCas9-BFP^{VP64}(VdC9BV), M2rtTA, and combinations of gRNAs to activate endogenous *MYOD1* upon dox induction, were produced as previously explained (Chakraborty 2014) and as shown in Figure 10. The tetracycline-inducible expression system was used to design the dCas9 plasmid to confer a temporal control of activating the gene of interest. In contrast, five gRNA sequences were designed with the continuous expression of to target different positions proximal to the endogenous *MYOD1* transcription start site and tested for the best combinations by qRT-PCR. With the "G8" gRNA combinations (combinations of gRNAs 1, 2, and 4), *MYOD1* was activated around 130-fold higher than the control EPCs (Figure 11A) after 5 days of dox induction. Thus, this combination was used throughout all the experiments in **Chapter 3.** *In situ* reprogramming of EPCs by transactivation of endogenous *MYOD1* using the CRISPR/dCas9 system. Transduction with these gRNA cocktails was also qualitatively assessed with RT-PCR to confirm the upregulation of other skeletal muscle-associated markers (Figure 11B). Once the myogenic fate was validated for iSkMs by the

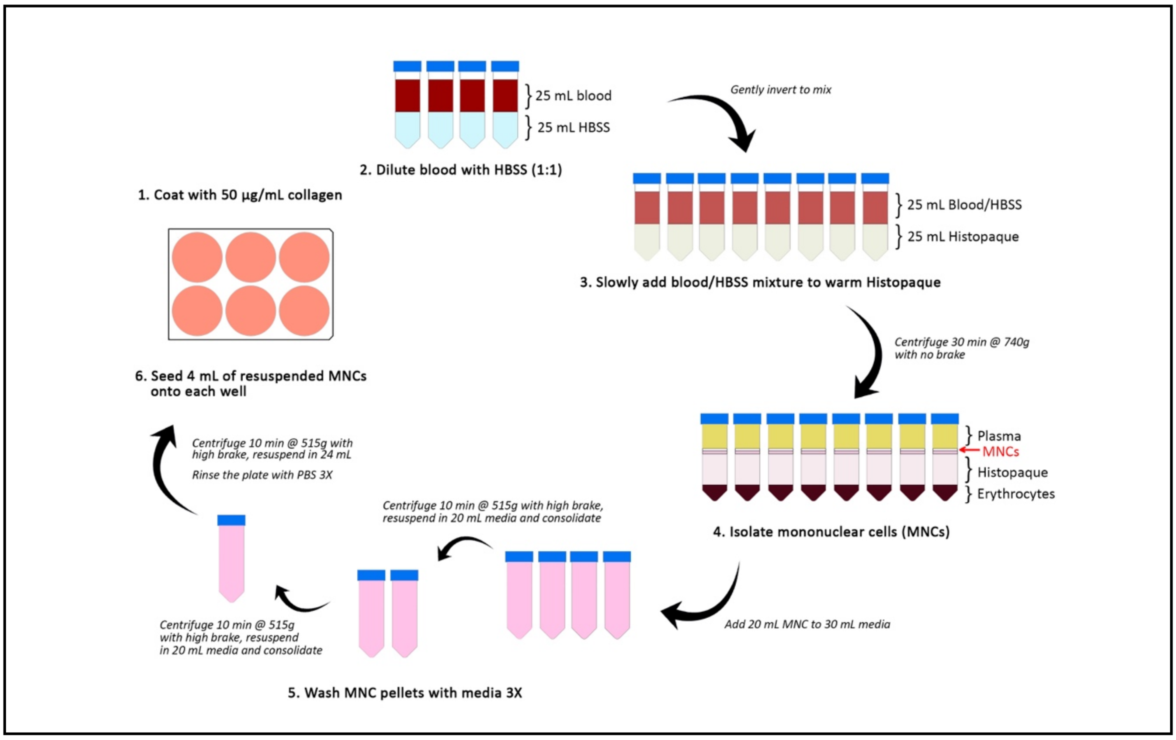

Figure 8. Schematic diagram of isolating EPCs from the UCB using a density gradient separation protocol .

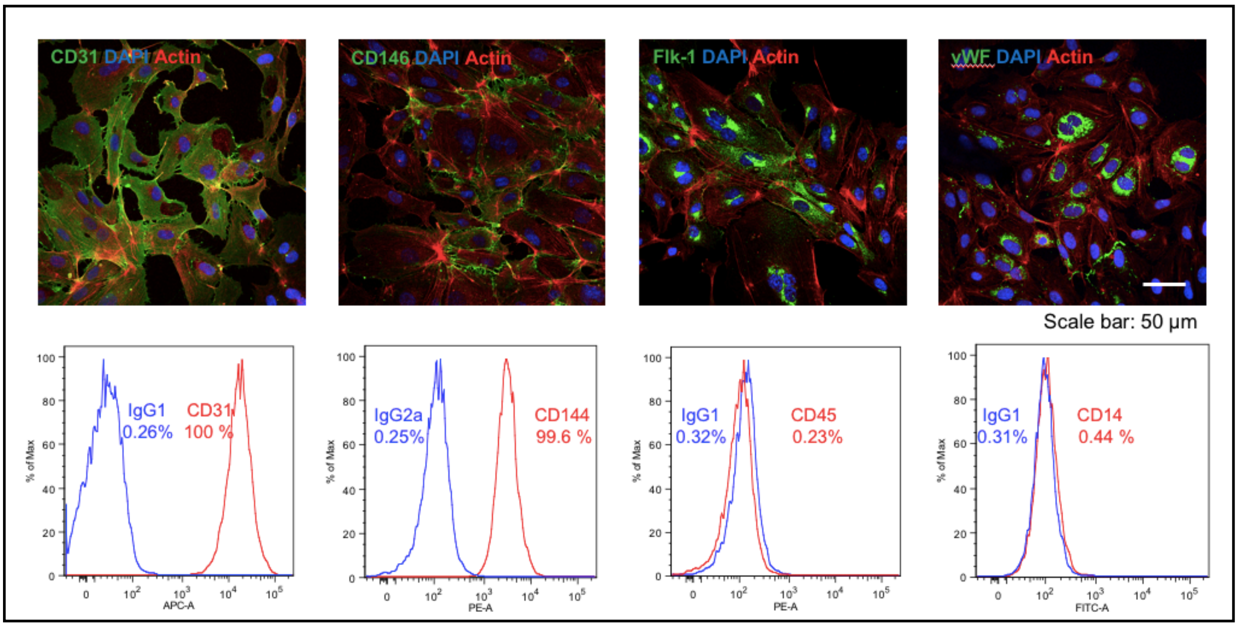

Figure 9. Isolated primary human EPC express EPC-specific markers. Immunophenotyping of EPCs using immunostaining (top) and flow cytometry (bottom).

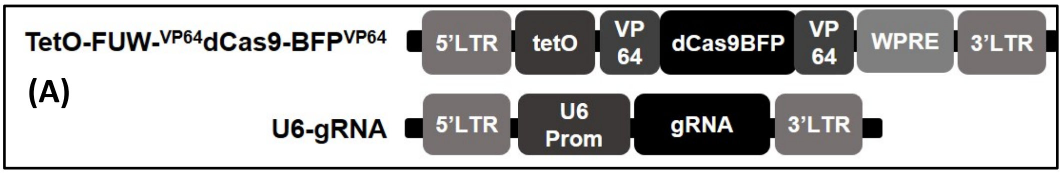

Figure 10. Constructed lentiviral plasmids for establishing reprogrammable EPCs. Plasmid maps of VdC9BV (top) and gRNAs (bottom) in a lentiviral plasmid vector driven by CMV and U6 promoter, respectively.

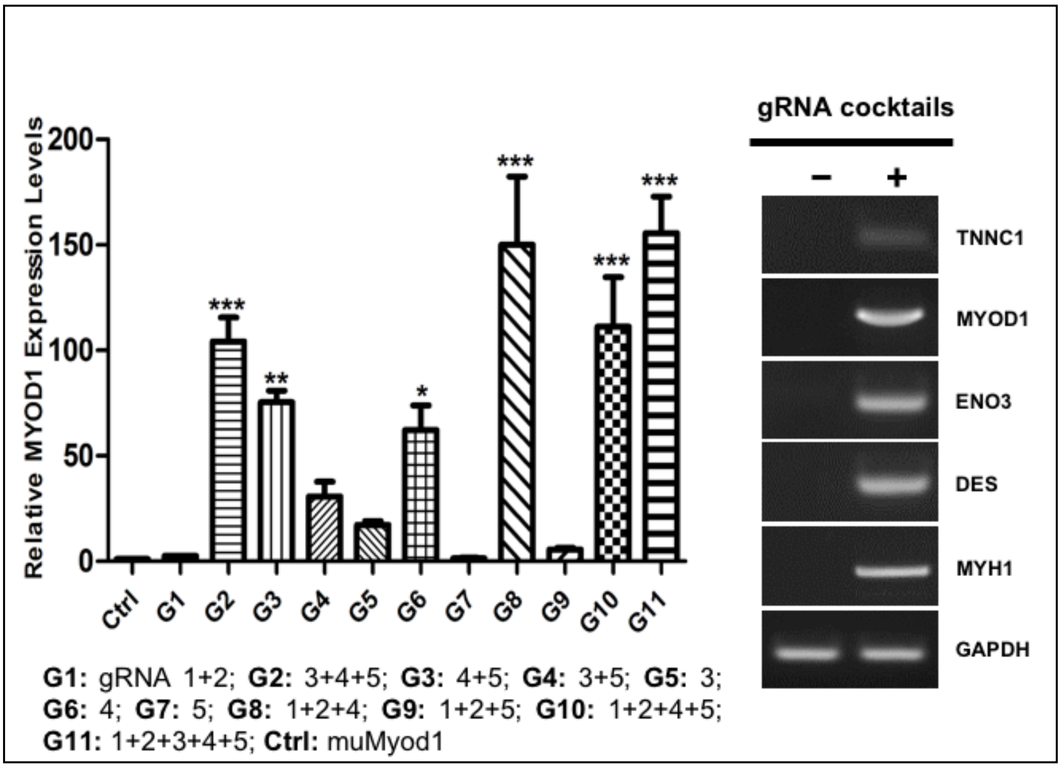

Figure 11. Confirming the activation of the myogenic differentiation program, initiated by the transactivation of the *MYOD1* in EPCs. Optimizing the gRNA cocktails based on the expression of endogenous *MYOD1* in tranduced EPCs, induced with dox for 5 days (A) using qRT-PCR and validating the expression of other myogenic-associated markers using RT-PCR (B) upon transducing the EPC with G8 gRNA cocktail. *: $p < 0.05$, **: $p < 0.01$,and ***: $p < 0.001$.

expression of *MYOD1*, VdC9BV and M2rtTA-transduced EPCs were sorted using the BFP (Figure 12A) reporter gene from the VdC9BV construct and expanded for further studies. A sorting step was necessary as transduction efficiency was low (4.06 %), presumably due to the large size of the VdC9BV plasmid (13.8 kb) with the co-delivery of gRNA mixtures using the lentiviral delivery system (Figure 12B and C). For validating reprogramming efficiency of the BFP-sorted EPCs, they were fed with an equal ratio of skeletal myoblast induction media and the EPC media in the presence of dox until the cells were characterized (Figure 13).

3.3.3. Short-term in vitro characterizations of the MYOD1 transactivated-EPCs

3.3.3.1. Immunofluorescence and flow cytometry analysis

For staining, FLAG epitope (DYKDDDDK) was used to trace the VdC9BV-transduced EPCs for being expressed twice as much in the VdC9BV construct compared to the BFP (Figure 10). With 7 days of continuous dox induction, approximately 30 % were FLAG$^+$ cells (Figure 14), while the intensity of BFP expression was low under the fluorescent microscope (data not shown). An additional week of dox induction increased the expression of *MYOD1* 30 times more than the control group (cells without dox), and 51 % of cells expressed BFP (Figure 15). Upon initiating the transdifferentiation process by adding dox, it significantly elongated the cell morphology as shown from the steeper slope of the SSC vs. FSC graph, which resulted in the heterogeneous cell population.

3.3.3.2. RNA-Seq analysis

To further corroborate and quantify the committed iSkMs, global gene expression patterns were analyzed for 25,560 genes. The iSkMs had 1903 genes overlapping with those expressed by the skeletal myoblasts (Figure 16A). Among all genes expressed by iSkMs, 8127 genes

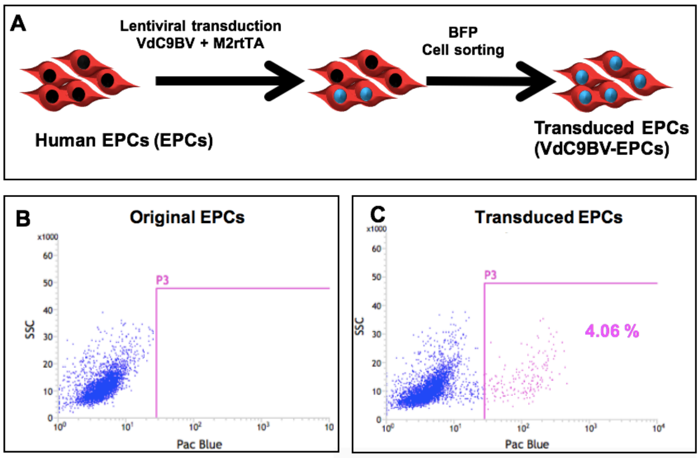

Figure 12. Sorting of VdC9BV-transduced EPC using BFP. Schematic diagram of the cell sorting process (A). Before (B) and after (C) BFP sorting of the transduced EPCs.

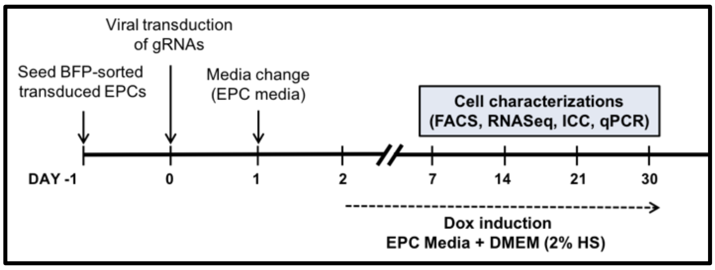

Figure 13. *In vitro* reprogramming schedule for myogenic transdifferentiation of EPCs

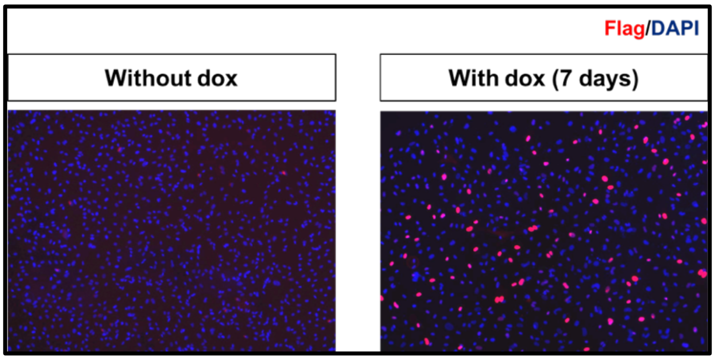

Figure 14. The expressions of FLAG-tag$^+$ cells with and without dox induction for 7 days.

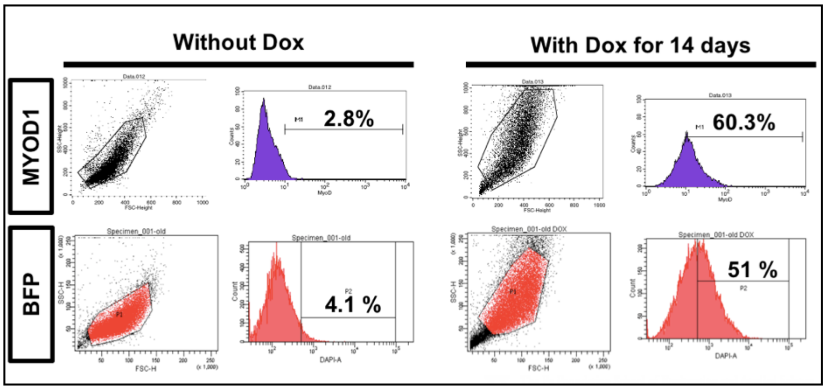

Figure 15. Expressions of *MYOD1* and BFP on the transduced EPCs without and with dox for 14 days.

were significantly different from the donor EPC genes ($p < 0.05$) and from them, skeletal myoblasts gene sets of the genetic regulatory network (GRN) were selected from the significantly downregulated or upregulated ones against the original EPCs. These downregulated and upregulated genes by the skeletal myoblasts were negatively (NES = -6.56) and positively enriched (NES = 11.44) by iSkMs, respectively (Figure 16B). This indicates that iSkMs have similar global gene expression pattern as our positive control, skeletal myoblasts. Among these gene sets of GRN, the most upregulated and downregulated genes were represented as a heat map (Figure 16C). Among all genes, *MYOD1* was the most elevated (230-fold) gene expressed, which signifies the activation of a master regulator for myogenesis to convert the EPC fate to the myogenic state. Owing to the early phase (day 5) of the lineage conversion, other mature myogenic transcripts were not significantly activated yet, but it was noticed that the EPC-specific markers, such as vWF and CD34, were downregulated compared to the parental ones. Additionally, distinctive transcriptional signatures of the original donor cells (EPCs), iSkMs at day 5, and the target cells (skeletal myoblasts) were exhibited in four quadrants by the PCA. As represented by dotted arrows, significant dimensional separation across different groups exemplified the transition of iSkMs diverging away from the donor cells and moving towards the target cells (Figure 16D). However, it was noticeable that the gene expression profile within the same sample group clustered similarly, representing low variability among triplicates. Collectively, RNA-Seq results confirmed the early transactivation of the *MYOD1* (within 5 days of dox induction), known to lead the activation of downstream myogenic-associated genes consequently.

3.3.4. Long-term in vitro characterizations of the MYOD1 transactivated-EPCs

After confirming the activation of *MYOD1* during the initial reprogramming process

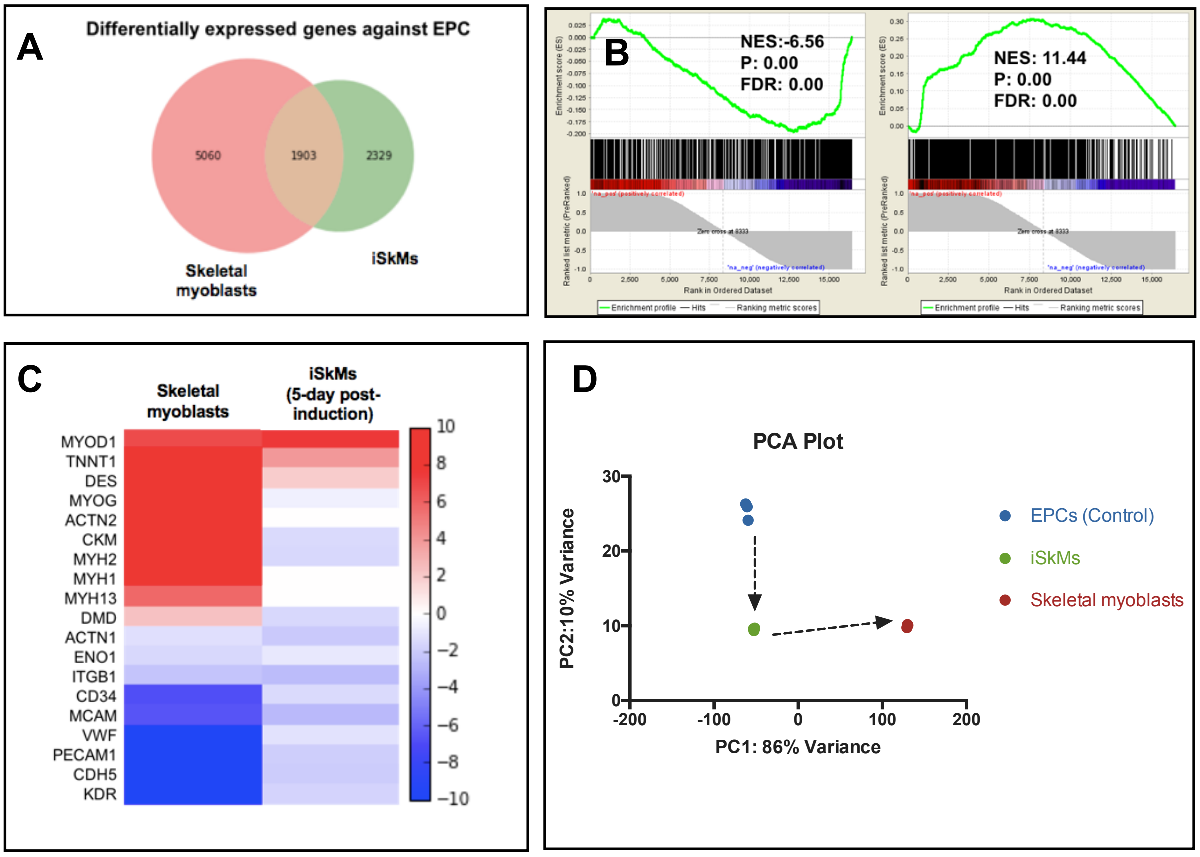

Figure 16. Comparing the transcriptomes of EPC, 5-day dox-induced iSkMs, and skeletal myoblasts. Differentially expressed genes for skeletal myoblasts and iSkMs against the original EPC (A). Both negatively (left) and positively (right) enriched global gene expression patterns of iSkMs. Heat maps representing the changes of gene expression levels for the skeletal myoblasts and iSkMs days of post-induction compared to original EPC (C). The PCA of whole genome expression profiles of EPC control (blue), iSkMs (green), and skeletal myoblasts (red) demonstrated the directed shifts of phenotypes toward the target cell type. n = 3 was used for each group (D).

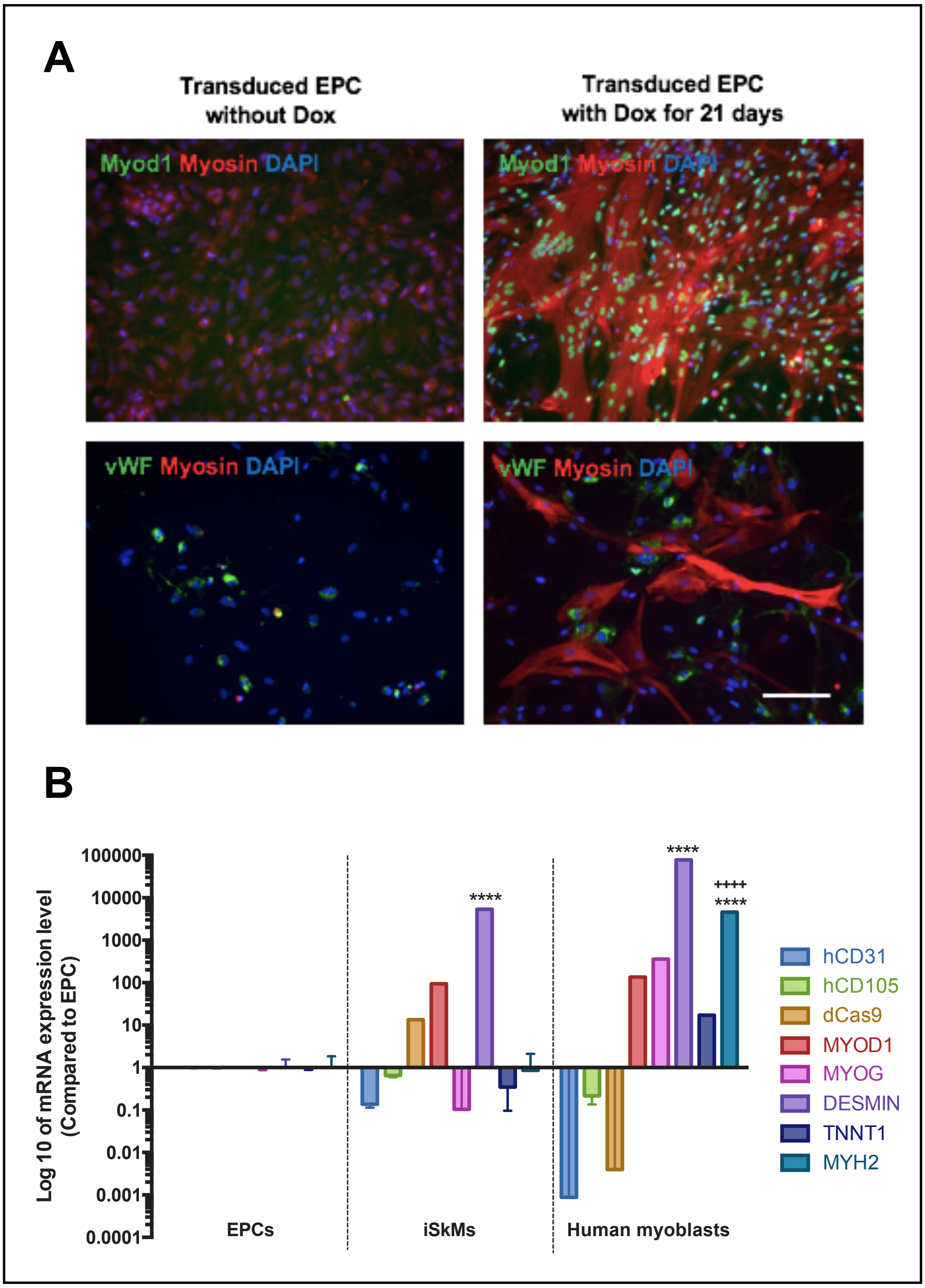

Figure 17. Long-term iSkMs express mature skeletal muscle cell-associated markers *in vitro*. Expressions of skeletal muscle cell-associated markers for a 3-week activation of *MYOD1 in vitro* with dox compared to the transduced EPC without dox (A). Scale bar represents 200 µm. Relative change in gene expressions compared with EPCs for EPCs, iSkMs (dox-induced for a month), and human myoblasts in a log scale of 10 (B). The symbols **** and ++++ indicate *p <0.001* when compared with parental EPCs and with iSkMs, respectively.

(Figure 11, Figure 15, and Figure 16C), the myogenic potentials of the transduced EPCs over a long-term dox induction (3 weeks) was confirmed by the expression of a mature myogenic marker, myosin heavy chain (Myosin)(Figure 17A). Their cell morphology was also signified by the multinucleated cell fusions with elongated morphology, whereas the transduced EPCs in the absence of dox lacked the *MYOD1* activation, thereby maintaining the EPC-specific, cobblestone-like morphology. This was further confirmed by the gene expression of iSkMs after a month-long dox induction compared to the parental EPCs and human myoblasts as positive control by qRT-PCR (Figure 17B). As expected, EPC markers (*CD31* and *CD105*) were downregulated for both transduced EPCs and human myoblasts compared to original EPCs, while another skeletal muscle associated marker expression was also elevated upon the transactivation of *MYOD1*. However, the mature skeletal muscle marker, myogenin, was not overexpressed in iSkMs even after a month of reprogramming, denoting that they were not fully matured in the *in vitro* setting. Thus, implying the limitation of providing the niche-like environment in a 2D setting for the complete myogenesis of EPCs by merely transactivating *MYOD1* in a low serum condition.

3.3.5. Validation of an immunodeficient NOD scid mice model

To fully promote the myogenic potentials of VdC9BV-transduced EPCs, our strategy was to expose them to the orchestrated *in vivo* biochemical signals similar to the native microenvironments by injecting reprogrammable EPCs to immunodeficient host (Figure 18). These signals may include secreted proteins, similar extracellular matrix compositions, and the elasticity of the tissue, which could further enhance the cell fate commitment to skeletal myoblasts. For the host, NOD *scid* transgenic mice were chosen for being immunodeficient (*i.e.,* harboring impaired innate immune activity) with low leakiness and its simplicity in breeding homozygous strains in house. The NOD background confers defective cytotoxic

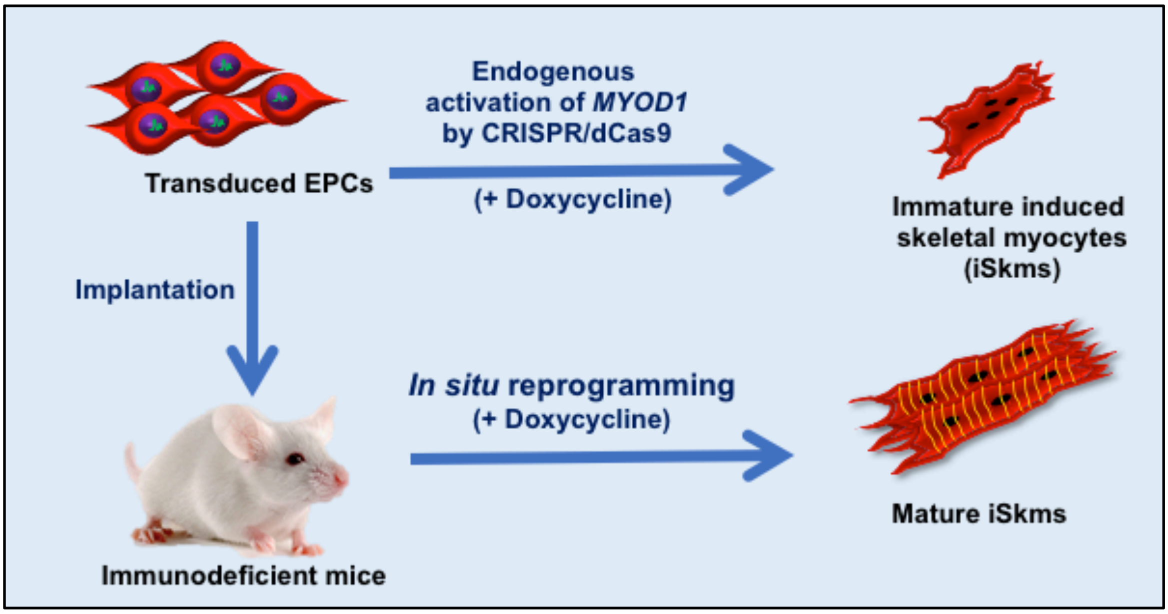

Figure 18. Schematic diagram of the first approach: using microenvironmental cues to facilitate *in situ* reprogramming of EPCs to mature iSkMs.

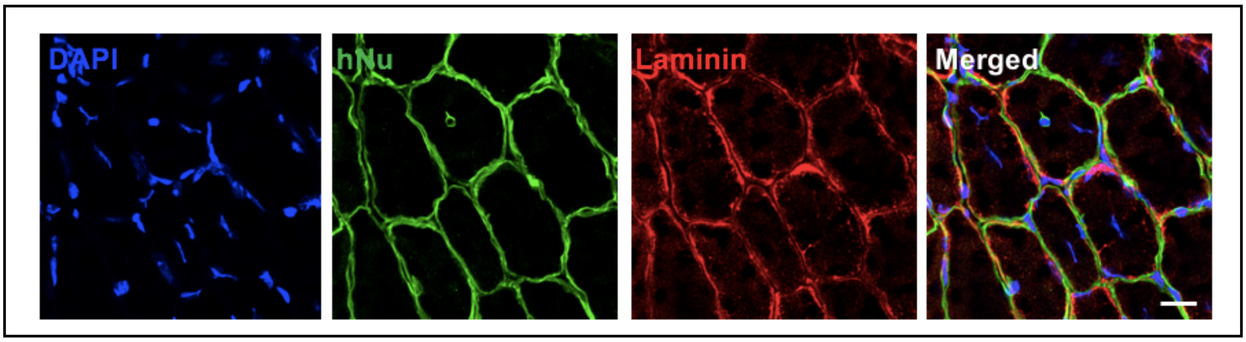

Figure 19. Two-week survival and engraftment of the transduced EPCs in the host TA muscle of the healthy murine NOD *scid* model. HNu stains for human origin cell and laminin stains for the basal lamina enclosing myofibers and capillaries. Scale bar indicates 20 µm.

activity of natural killer cells and additional *scid* mutation (athymic) yields impaired development of mature T and B lymphocytes, affecting the adaptive immunity.

Before accessing the maturation of the reprogrammable EPCs *in situ,* the survival and engraftment of the transduced EPCs were tested in a healthy model of the immunodeficient NOD *scid* mice ($n = 3$) and muscles were harvested after two weeks. As shown from Figure 19, immunostained muscle slice validated the survival and functional integration of the injected cells to the host tissue, determined by a centronucleated myofiber. Unlike other centronucleated myofibers stained by DAPI only, the cell co-immunostained with DAPI and hNu staining indicated the implanted cell among other infiltrated host's cells. While injection took place in the absence of the chemically-induced muscle injury, it was hypothesized that during the injection process, the large needle diameter would have damaged the host's intact myofibers. Among 0.5 million injected cells exposed to the *in vivo* microenvironmental cues, only a few of them were engrafted for several potential reasons: 1) localized myofiber damage, only limited to the needle injection path; and 2) low number of injected cells available to migrate towards the injury site, thereby, making the engrafted iSkMs challenging to track. Nonetheless, comparing the muscle moist weight between the control (saline) and the cell-injected groups ($n = 3$) both without dox showed a significant difference ($p = 0.0116$): 36.53 ± 0.50 and 34.23 ± 0.75 mg, respectively. This may denote the inadequate length of the study (2 weeks) for restoring the damage caused by the invasive injection process. To address these limitations collectively, we examined the pathologically-relevant *in vivo* microenvironment of the host for increasing the regeneration capacity of the injected iSkMs.

3.3.6. Establishment of the notexin-induced skeletal muscle injury in vivo model

To better mimic the pathophysiological conditions of the injured muscle *in vivo*, various injury models were assessed based on the established methods, using: 1) physical injury (*e.g.,* laceration or crush), 2) chemical-based injury (*e.g.,* cardiotoxin, notexin, or bupivacaine), and 3) cryoinjury (*e.g.,* liquid nitrogen). For yielding a consistent, controllable, and reproducible injury model across each host, the chemically-induced procedure was chosen. At first, 0.5 % of bupivacaine was tested, but from the preliminary results after a month of post-injury, no significant difference in average fiber size was observed across the treated and non-treated (saline control) mice groups (data not shown). To induce more severe insult than bupivacaine, stronger chemical notexin, isolated from snake venom, was selected for our study.

To detect the extent of damage, notexin-injected muscles were harvested after a day to compare the associated pathological changes to its control. The color, myofiber structure, and the fibrotic scar formation all indicated a significant difference between the intact and injured sites at one-day post-injury (Figure 20). Injecting notexin destroyed the sarcolemma structures of the muscle fibers, while immune cells subsequently were recruited to repair the affected site.

After establishing a notexin-induced injury model, one million cells were transplanted one-day post-injury using a stereotaxic syringe pump installed with the Hamilton syringe to regulate the speed of injection. Until the TA muscles were harvested after a month of injury, water with or without dox was delivered orally to different groups of NOD *scid* mice to elicit *in situ* reprogramming at the injured site (Figure 20). A day of the interval was given after the chemical and invasive injury induced by notexin and the needle to deliver transduced EPCs for preventing them from getting exposed to an acute proinflammatory microenvironment, where orchestrated signals of proinflammatory cytokines (*e.g.,* TNF-α and IL-1β) are secreted by the necrotic myofibers and muscle satellite cells. These danger signals serve as chemoattractants to recruit immune cells (macrophages and monocytes) for the skeletal muscle repair (Chazaud et al., 2003). At the same time, it was kept as short as possible to prevent the host's muscle satellite cells—competing entity against iSkMs—to rapidly enter the mitotic cycle to

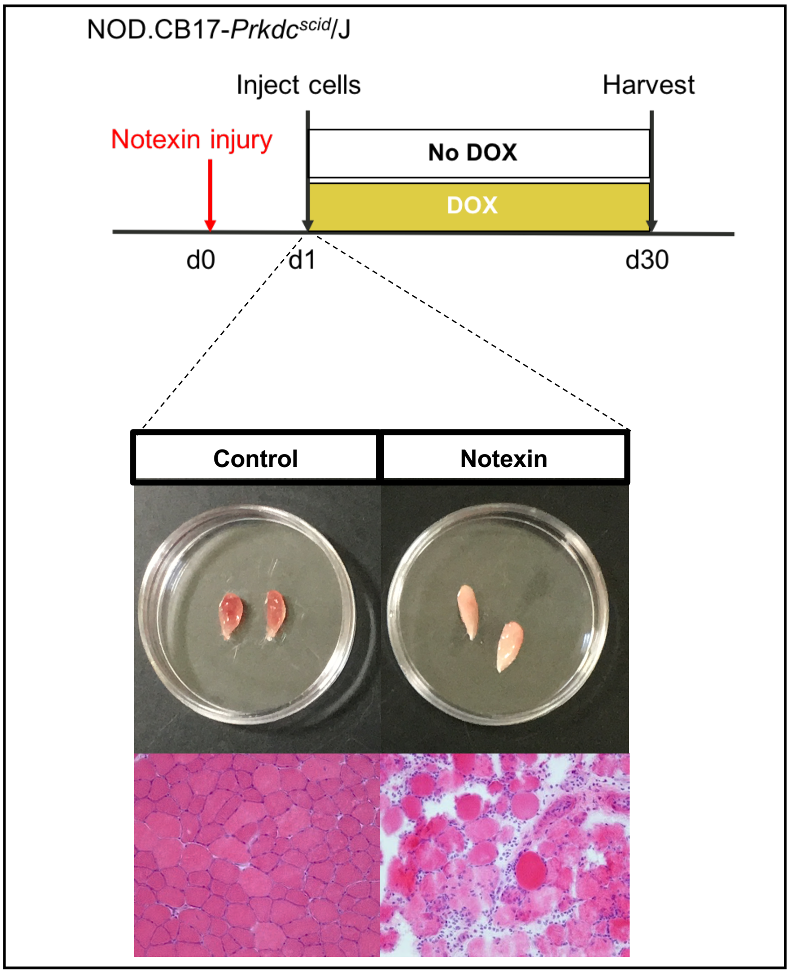

Figure 20. The establishment of the notexin-induced TA muscle injury model. Schematic diagram of the *in vivo* study scheduled for the NOD *scid* mice model (top) and the variation in muscle phenotypes (morphology and H&E stained results) of the intact muscle (control) and injured one at 1 day post-injury (bottom).

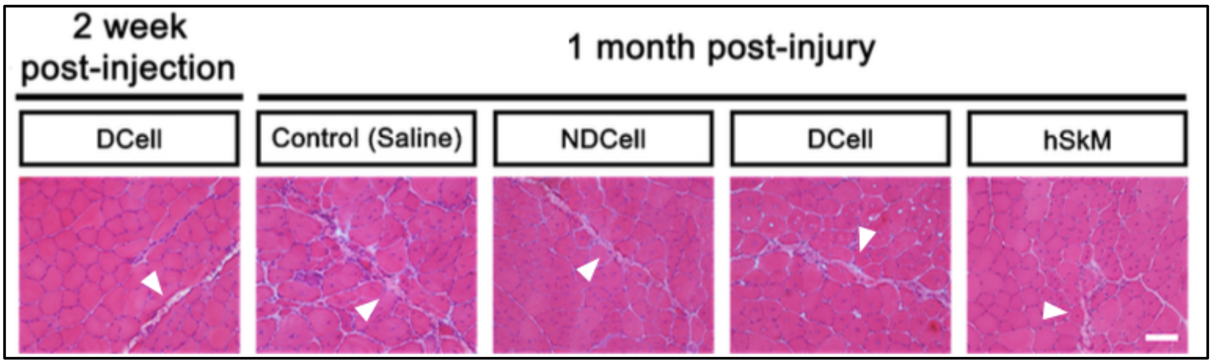

Figure 21. Histological evaluation of the regenerated injected sites (white triangle) for both intact muscle (2-week post-injection) and notexin-insulted muscle (1 month post-injury). Abbreviations: DCell, dox-given cells; NDCell, no dox-given cells; hSkM, human skeletal myoblasts. Scale bar indicates 100 μm.

participate in the myogenic repair pathway for re-establishing the muscle structure and its function (Collins et al., 2005; Le Grand & Rudnicki, 2007).

As described in *3.3.5.*, compared to the intact muscle model with localized invasive myofiber damage, more severe and broader myofiber damage was observed for the notexin-injury model, although the study duration lasted two weeks longer than the preliminary engraftment study (Figure 21). More centronucleated myofibers were observed near the injection sites (indicated by white triangles) for all the groups in the injury model compared to the intact one. This may have increased the engraftment efficiency of iSkM by driving the myogenic potential of the transduced EPCs *in situ*, thereby enhancing the reconstitution of the damaged myofibers. Lacking the proper setup, it was not feasible to conduct the muscle functional recovery test. Besides, it was challenging to discern the muscle regeneration efficacy based on the locomotion of mice as skeletal muscles are highly adaptive tissue (Abresch, Walsh, & Wineinger, 1998). Therefore, by one week of post-injury, all mice seemed to adapt to their injury by delegating the force applied to the TA muscle and restoring the normal movement. Therefore, for the quantitative comparisons of the therapeutic effect across the treatment groups, morphometric evaluations were performed by analyzing 2 to 3 random microscopic fields per three animals per group.

3.3.7. Morphometric evaluation of the fibrosis, myogenesis, and myofiber regeneration

3.3.7.1. Pathohistological assessments of engrafted iSkMs for regenerating damaged myofibers

Tracing the regeneration of injured muscle after a month, it was observed that injured muscle fibers were reconstituted with diverse recovery efficiencies based on the groups implanted with saline (negative control), human skeletal myoblasts (hSkM; positive control), transduced EPCs induced with dox (DCell), and transduced EPCs without dox (NDCell). It was noted that the saline control and NDCell had severe necrotic fibers (purple myofibers), which suggested the incomplete myogenesis. However, more centronucleated myofibers, representing the recently regenerated ones, were observed from the groups injected with hSkM or DCell with no signs of necrotic tissue formation (Figure 22A).

Unlike the intact muscle, even after a month of regeneration, not all muscle fibers were fully restored to its original state in terms of its number and size. Notexin insult destroyed the myofibers, which rendered a void space for immune cells and muscle satellite cells to mitigate the inflammatory response and activate the myogenesis for regenerating mature myofibers, respectively. During this process, the microenvironment of the stem cell-niche dynamically changes. To secure the anatomical position of the damaged myofiber structure, the fibrillar structure of ECM proteins get deposited mainly from mesenchymal stromal cells until myofiber debris get cleared and myofibers re-establishes (Bentzinger, Wang, Dumont, & RUDNICKI, 2013). Along with the deposition of the ECM proteins, one of the mesenchymal stromal cells, fibroblast adipogenic progenitor cells expand upon injury and secretes IL-6 for promoting the myogenic differentiation (Joe et al., 2010).

As a result, more than 100 myofibers with small fiber diameters differentiated to fill the void gap for a month during the recovery phase. The non-treated groups (saline control and NDCell) demonstrated impeded reparative myogenesis (Figure 22A), resulting in significantly smaller average fiber sizes compared with the treated groups (DCell and hSkM). Nonetheless, owing to the expansion of the host's muscle stem cells, the total fiber area of the non-treated groups comparable to the intact muscle (Figure 22B and Table 3). These trends were in line with the accumulation of excessive ECM protein (mostly collagen) and visualized by consecutive slides stained with H&E and Sirius red (Figure 22C); the less fibrotic scar was formed for the treated groups, while more collagen deposition was observed from the non-

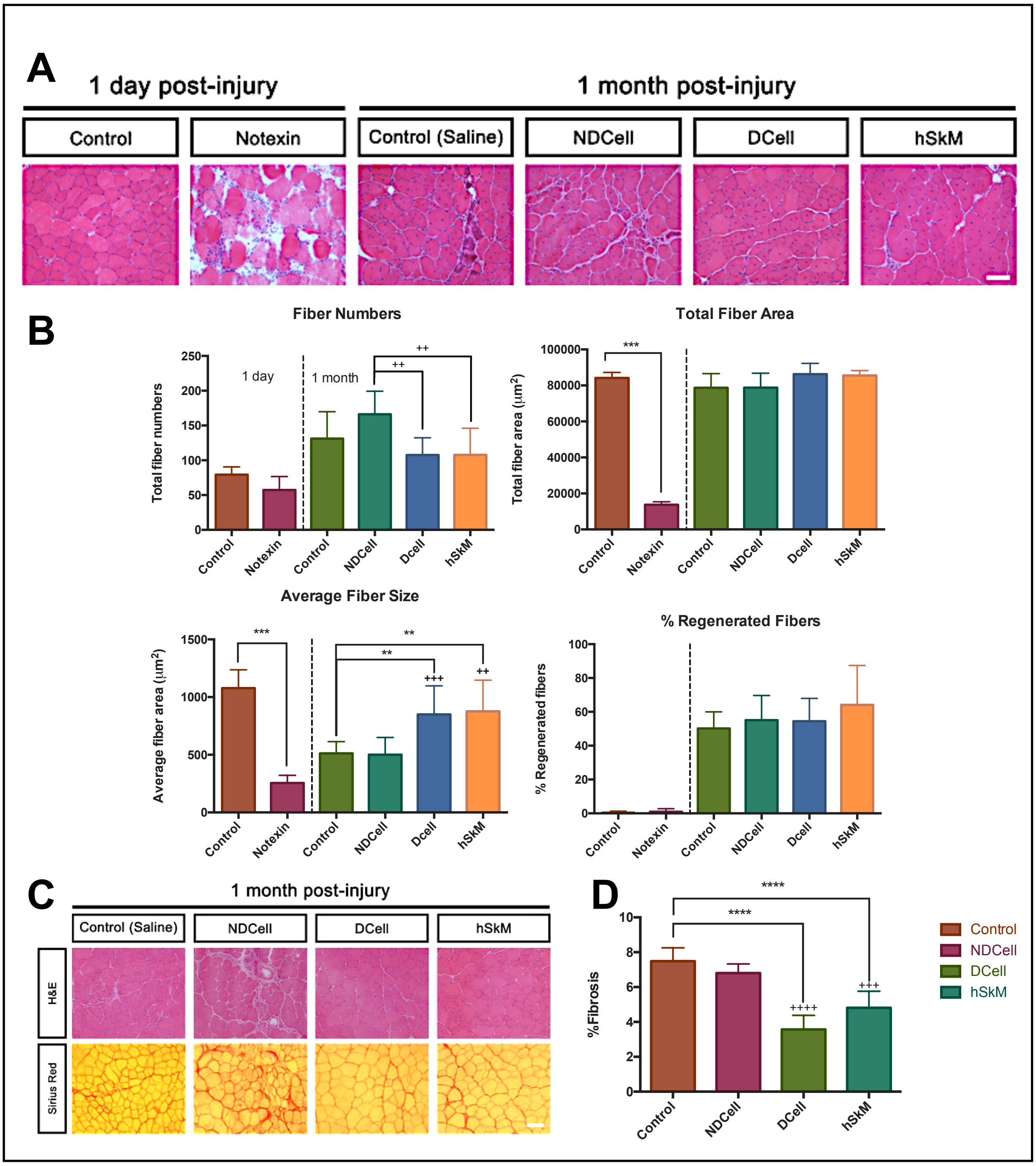

Figure 22. Morphometric evalution of the implanted cells in notexin-induced muscle injury model. H&E-stained TA muscle sections with the established notexin-induced muscle injury model (1 day) and the injury sites after a month compared to its saline control (A). Quantitative analyses based on the H&E-stained TA muscles, including the total number of fibers, total fiber area computed by Image J, the average fiber size — calculated from dividing the fiber area with the fiber number — and the % regenerated fibers. Control for the one day post injury was used as an intact muscle while control for one month post injury, saline control was used. All data are represented as means ± standard deviations. ** denotes $p < 0.01$, and *** denotes $p < 0.001$ compared to control of each time point, and +++ denotes $p < 0.001$ compared to NDCell group (B). Consecutive H&E- and Sirius red-stained TA muscle images (200X) a month after injury. All scale bar represents 100 μm (C). Average percent fibrosis calculated from different treatment groups compared to the control (saline) group after a month of injury (D).

Table 3. Summary of quantified morphometric evaluations of the regeneration of notexin-injured muscle. All data are represented as means ± standard deviations. ** denotes $p < 0.01$, and *** denotes $p < 0.001$ compared to control of each time point, and $^{+++}$ denotes $p < 0.001$ compared to NDCell group.

Experimental endpoint	**Groups**	**Fiber Number**	**Total Fiber Area (µm²)**	**Average Fiber Size (µm²)**	**%Regenerated fibers**
1 day (Notexin)	Control	78 ± 11	83924 ± 1778	1098 ± 147	0 ± 1
	Notexin	57 ± 8	13709 ± 6247***	256 ± 17***	1 ± 1
4 weeks (Notexin)	Control	159 ± 33	78725 ± 7506	512 ± 98	50 ± 10
	NDCell	166 ± 21	78796 ± 7633	501 ± 108	55 ± 13
	DCell	108 ± 13^{++}	86235 ± 2281	850 ± 81$^{**/+++}$	54 ± 6
	hSkM	108 ± 28^{++}	85491 ± 1785	877 ± 221$^{**/++}$	64 ± 22

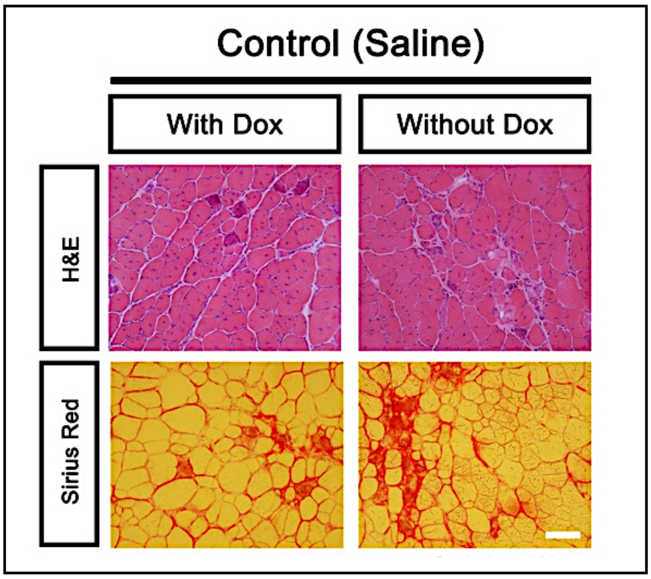

Figure 23. Pathohistological analyses for dox having no therapeutic effect on saline controls. Scale bar represents 100 µm.

treated groups. Another therapeutical aspect to note was the increase in average muscle moist weight for both control and treatment groups compared with the 2-week intact muscle model. This illustrates the enhanced muscle regeneration after 2 more weeks of recovery corresponding to the muscle weight of control (saline) without dox, NDCell, and DCell to 39.34 ± 1.93, 42.32 ± 1.63, and 37.94 ± 6.68 mg, respectively.

Quantitative analysis of %fibrosis also supported the delayed repair of muscle injury and necrotic tissue formation of non-treated groups, while both treated groups indicated significantly less %fibrosis compared to the non-treated groups (Figure 22D). For having the highest %fibrosis, the saline control group was further examined to evaluate the effect of dox administration to the host. As shown from Figure 23, similar inflammatory responses (*e.g.,* necrotic tissue formation and collagen deposition) and the slow recovery of the affected sites were observed from both control groups, irrespective of the addition of dox. Muscle moist weight data were in line with the insignificant effect of dox addition on muscle phenotypes; the muscle moist weight of the saline control in the absence and presence of dox were measured as 39.34 ± 1.93 and 40.93 ± 6.17 mg, respectively.

3.3.7.2. Immunocytochemistry analysis for cryosectioned-muscle tissues

The immunohistochemistry results also demonstrated that the transplanted cells contributed to the stem cell niche by fusing to the damaged host muscle fibers and contributing to their recovery (Figure 24). iSkMs expressed both hNu for being human origin cells as well as FLAG for being transduced with the VdC9BV construct. Therefore, both markers were co-localized with DAPI at the nucleus for the DCell group, committed to myogenic lineage and transdifferentiated to iSkMs. Conversely, cells without dox (NDCell group) expressed hNu, but lacked FLAG expression as they were not committed to skeletal myocytes while maintaining the signatures of the donor cells. Therefore, injected NDCells were located near

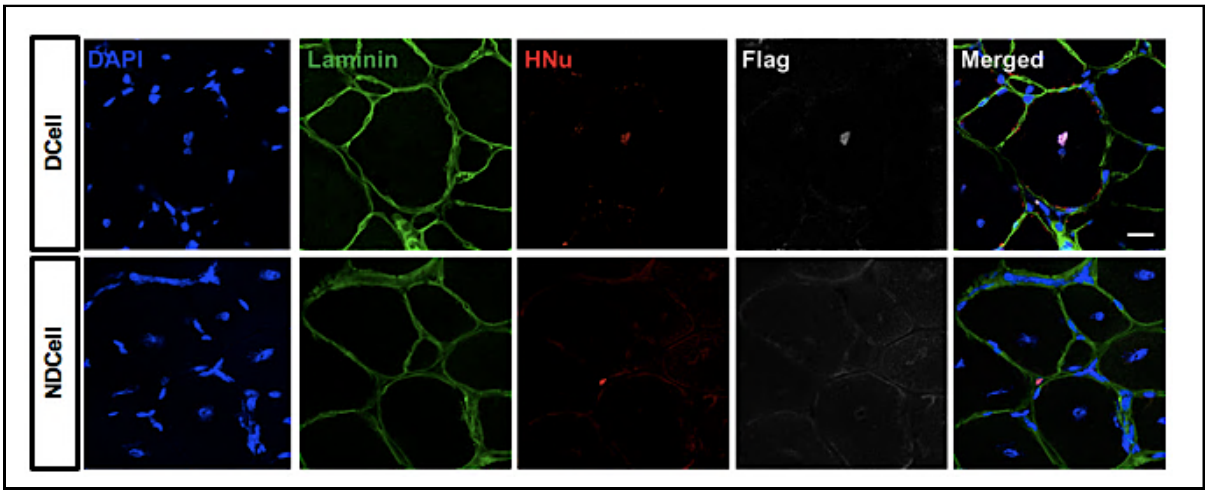

Figure 24. Transverse cryosections of the cell-transplanted TA muscle indicating the engraftment of iSkM *in situ* after a month of injury. Scale bar indicates 20 μm.

the quiescent muscle satellite cells beneath the basal lamina, indicating no partaking in the regeneration of myofibers. Unlike inactive HNu$^+$ NDCells, surrounding centronucleated myofibers with muscle satellite cells have higher reparative contribution rate for injury restoration.

Muscle satellite cells (skeletal myoblasts) are also known as muscle stem cells. In a typical matured myofiber environment, they stay quiescence beneath the myofiber's basal lamina (Schmalbruch & Lewis, 2000). Such cells self-renews in asymmetrical cell division and provides heterogeneous cell types in the satellite cell niche: a mixture of committed myogenic progenies and uncommitted cells, which remains as mother cells (Bentzinger et al., 2013). Between these two groups, only actively proliferating myoblasts express *MYOD1*, which mimics the phenotypes of our committed (DCell). The reason for the total fiber area and the %regenerated fibers to be insignificant across the groups was also due to the expansion of the host's myoblasts, which led the active formation of newly differentiated centronucleated myofibers. In order to thwart the faster regeneration rate of the host's myoblasts, few studies utilized radiation to ablate them. Exposing mice with 18 Gy γ-irradiation before cell injection formed a significantly higher number of myofibers of implanted cell origin (Gross, Bou-Gharios, & Morgan, 1999). However, for our study, as the radiation facility was inaccessible, it was not feasible to regulate the differentiation rate of the murine myoblasts and better control the therapeutic effects of the control groups (saline control and NDCell). For proper assessment, γ-irradiated genetically modified animal models, such as dystrophin-lacking *mdx* model, should be used for future experiments.

3.3.7.3. Assessing the contribution of the transplanted cells on neoangiogenesis

Efficiency is a known limitation of direct reprogramming, owing to the retention of the donor cell's epigenetic memory (K. Kim et al., 2010b; Vierbuchen & Wernig, 2012). Therefore, we speculated that some portion of the DCell group might have remained as EPCs, even with the administration of dox. Since EPCs are known to play a regulated role in neovascularization — a process involving proliferation, migration, and adhesion to remodel pre-existing vasculatures (Kamei, Atesok, & Ochi, 2017)—, we extended our goal to assess the contributions of non-reprogrammed cells to host neoangiogenesis during the regeneration process by CD31$^+$ and vWF$^+$ expression patterns. From the immunostained-tissue sections, differences were apparent between the negative control and the DCell group: CD31 was expressed significantly more from the DCell group, demonstrating the enhanced vascularization at the environs of the injured tissue compared to control (Figure 25). As shown in Figure 26, the ratio (A) and the average number per area of CD31$^+$ capillaries and vWF$^+$ EPCs (B) were also quantified for comparison. From both analyses, more capillaries were formed by DCell group compared with the control group and as EPC plays a crucial role in angiogenesis, a higher density of EPC correlated with the higher number of local capillaries. However, for the global contribution of transplanted cells on the host microenvironment, the relative gene expression pattern should be analyzed for the future studies.

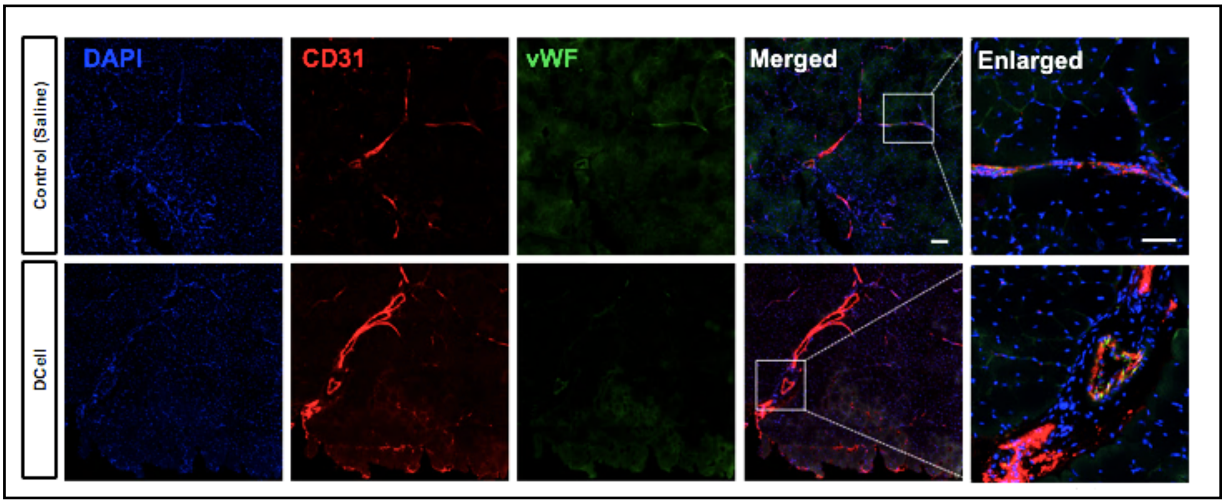

Figure 25. Contribution of iSkMs on local neoangiogenesis compared to saline control at the muscle injury site. Scale bars indicate 100 and 50 μm for the DAPI/CD31/vWF and merged images (200X), and enlarged images (400X), respectively.

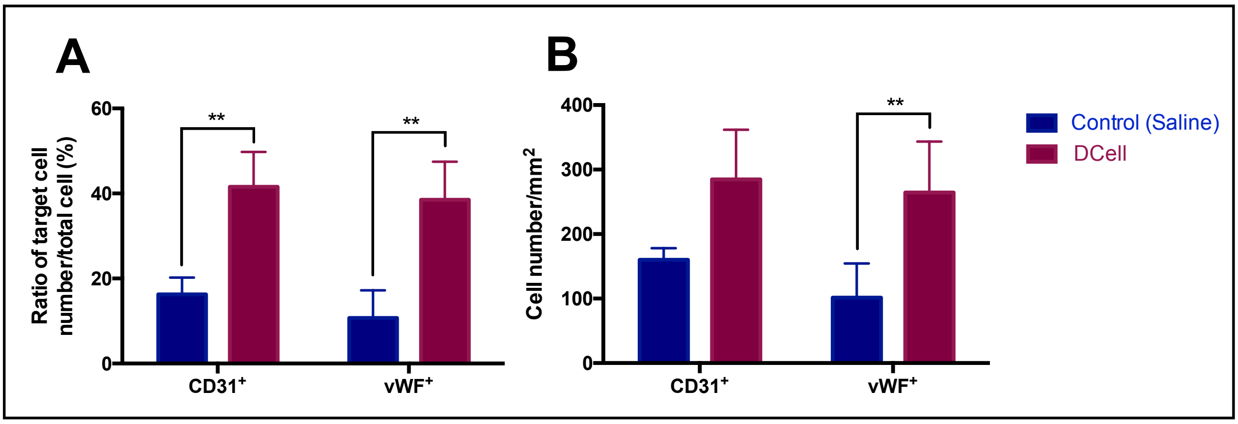

Figure 26. Quantified ratio and average number of CD31+capillaries and vWF+ angiogenic endothelial cells after 1 month post-injury for control and DCell groups. ** indicates $p < 0.01$

Chapter 4. Enhancing the neural cell fate commitment by deploying biochemical cues and substrate-mediated electrophysical cues

4.1. Rationale and Significance

In this section, we focus on substrate-mediated microenvironmental stimuli combined with biochemical cues, which can epigenetically modulate cell fate by activating the intricate mechanotransduction pathways of cells. We hypothesized that the combination of graphene-based substrates with the biochemical factors would assist the promotion of directed differentiation and transdifferentiation of neuronal stem/progenitor cells and somatic cells to neuronal lineages, respectively.

Surface characteristics of the substrates can help govern cell fate and their behaviors. Researchers have engineered the substrate-mediated cues for guiding the cell fate by manipulating the substrate rigidity, roughness, topography, and other biophysical features. For example, engineering the topography of substrates (both nano- and micro-scales) can offer forced confinement for cells to artificially align themselves on a patterned/aligned substrates, which have been documented to facilitate the directed differentiation (human MSCs to neurons (Yim *et al.*, 2007) and adult heart-derived progenitor cells to cardiomyocytes (Morez *et al.*, 2015)), reprogramming (MEF and human dermal fibroblasts to iPSCs (Downing *et al.*, 2013)), and transdifferentiation (somatic cells to various neuronal lineages (Kulangara *et al.*, 2014;

Yoo *et al.*, 2015)).

For the substrate, we chose an electroactive graphene-based substrate with aligned micropatterns to evaluate whether it guides subtype neuronal differentiation and transdifferentiation processes. Graphene-based materials have exhibited excellent biocompatibility and capabilities in facilitating cell adhesion, proliferation, neural differentiation, and axonal outgrowth of MSCs, NSCs, and iPSCs. It is known to support the growth of neuronal lineages for its robust surface chemistry and excellent mechanical properties, but the molecular mechanism of how graphene supports the cell-cell or cell-matrix interactions is not yet elucidated. Because of its hydrophobicity, pretreatment with oxygen plasma treatment is necessary for ECM protein coatings, but the bulk property of conductivity is not affected by the protein coating.

The rationale behind using highly conductive graphene originates from the notion that electrical stimulation can facilitate NSC/PCs migration to target sites and differentiate them into neurons *ex vivo* (Huang, Li, Chen, Zhou, & Tan, 2015). Moreover, in pre-clinical studies, the potency of electrical stimulation on enhancing neurogenesis has been documented.

The addition of eight small molecules allows rapid, transient, efficient, economic, and finely-tuned regulation of cell fate change. As we use epigenetic modulators (inhibitors and activators of key cellular regulation pathways), the microenvironment exposed to cells is more permissive to neurogenesis and survival of NS/PCs. Eliminating the usage of viral vectors and transcription factors, and any associated risks for insertional mutagenesis are avoided upon using soluble factors. This provides a potent means of inducing neurons from easily accessible and robust cell sources, such as fibroblasts. For our purpose, as graphene is non-transparent, to track their morphology, fetal human dermal fibroblasts expressing GFP (fHDF-GFP) was used. As a first demonstration, our work illustrates the graphene-based substrate with high conductivity (> 650 S/m) can promote the human neuronal lineage from varying cell sources:

NSCs, NPCs, and fHDF-GFP. In other studies, instead of graphene, graphene derivatives (graphene oxide or reduced graphene oxide) are utilized to replace for graphene's strong hydrophobicity. This completely removes or reduces graphene's natural feature of the highly conductive substrate, thereby losing the rationale behind using the electroactive substrate. Along with its high conductivity, the graphene substrate is fabricated from a graphene paint, mixed with a medical-grade poly-lactide-co-glycolide (PLG) at the ratio of 60:40 (in Volume %) mixed in organic solvents to make them into a paste. The viscosity is maintained for enabling it to push through a piston for 3D printing. Such a method of substrate fabrication allows rapid, simple, and versatile means for fabricating any polymer-based composites.

4.2. Methods

4.2.1. Fabrication and surface modifications of the graphene-based substrates

To fabricate the graphene:PLG composites, established method was used as previously mentioned in Jakus et al. (Jakus et al., 2015). Briefly, 60 % graphene inks in volume were synthesized by thoroughly mixing PLG copolymer (85:15; Boehringer Ingelheim), graphene powder (38 atomic layers thick, 520 µm long and wide; Graphene Laboratories Inc), and a 10:2:1 by mass mixture of DCM (Sigma), ethylene glycol butyl ether (Sigma), and dibutyl phthalate (Sigma), where 0.6 g of dibutyl phthalate was added for every 2.2 g (1 cm3) of graphene. Graphene comprised 60 % of the solid additions in volume, while PLG comprised the remaining 40 % in volume. Inks were allowed to thicken to a viscosity of 3035 Pa.s., as determined through the use of a Brookfield DV-E rotational shear viscometer, through evaporation under ambient conditions before 3D printing. Pure PLG inks were also prepared using the same protocol.

The grooved structures of graphene:PLG composites and PLG were fabricated using a 3D BioPlotter (EnvisionTEC GmbH). The 200 µm diameter polyethylene tips (Nordson EFD) was used throughout the study. Both PLG inks and the graphene-PLG inks were 3D-printed onto a smooth, polytetrafluoroethylene-coated substrate. The speed of the XY motion ranged from 10 to 45 mm/s based on the features of the printed objects. They could be directly removed from the substrate and handled immediately after printing. All ink syntheses and printing were performed at RT. The grooved substrate was printed using 200 µm diameter polyethylene tips and approximately 180 µm spacing between fibers. The printed grooved substrates were all kept at 4 °C till future use to maintain their features.

Two types of graphene:PLG mixed substrates were used for the study along with the conventionally used negative control as a glass disc. Both were produced and generously provided by our collaborators, Prof. Shah and Dr. Jakus, from the University of Chicago and Dimension Inx LLC, respectively as published (Jakus *et al.*, 2015): 1) graphene:PLG-cast sheet and 2) monolayer 3D-printed grooved graphene:PLG substrate (3DG), fabricated with a diameter of 250 µm extrusion tip, thereby having the aligned patterns with approximately 200 µm widths. All tested substrates were punched with two different sizes (8 mm and 12 mm) of biopsy punches, rinsed with 70 % ethanol for at least an hour on a rocker and rinsed with autoclaved distilled water for three times. After completely drying the substrates, they were placed in the oxygen plasma cleanser (Harrick Plasma Inc.) for conferring hydrophilicity. Upon functionalizing the surface with oxygen for 1 min at a ‘high’ setting, substrates were sterilized under UV exposure for 20 mins and subsequently coated with 0.01 % poly-D-lysine (PDL; Sigma, P7405) overnight at 4 °C.

On the next day, following the original protocols, various types of protein coatings were utilized for the directed differentiation to MN and DA neurons and direct reprogramming to induced pan-neurons. For MN differentiation, substrates were coated with LM (20 ng/µl; Millipore Sigma, L2020) overnight at 4 °C. For DA neuron differentiation, substrates were coated instead with 15 µg/ml poly-L-ornithine (PLO) overnight at 4°C and on the following day, 5 µg/ml of FN (Sigma, F2006) and 4 µg/ml of LM were mixed and diluted with DPBS to be coated overnight at 4°C. For direct conversion to induced neurons, oxygen plasma-treated substrates were coated with 0.1 % porcine gelatin (Sigma) for at least an hour at 37 °C before seeding fHDF-GFP. For preventing the discrepancy of cell seeding number, cells were plated at the center of each substrate at least three hours before media was added to provide them enough time to attach to the coated culture platforms.

4.2.2. Characterization of the graphene-based substrates

Both graphene:PLG composites were prepared for the FE-SEM analysis by sputter coating the samples with platinum and micrographs were captured at the magnification of 300X using Zeiss Sigma 500. For visualizing the electric flow through the graphene:PLG composite, the apparatus was set up by contacting/disconnecting the sample with a wire in series with a green LED probe. The XRD patterns were measured with Ultima IV (Rigaku) in the diffraction angle (2θ), ranging from 5 to 60°, at a rate of 2°/min with an interval step-width of 0.02° using Cu-K_α radiation at 40 kV and 40 mA. The conductivity was measured in triplicates with a conventional method using a 4-point probe from NWU collaborators. The wettability of each substrate was measured by the contact angle between a water droplet and the graphene interface with and without the oxygen plasma treatment. The angles were measured from triplicates of each sample using Image J.

4.2.3. Cell maintenance and media compositions

Two iPSC-derived NSCs and NPCs were used for specific neuronal (MN and DA neurons, respectively) differentiation and for pan-neuronal direct reprogramming, fHDF-GFP was used.

The iPSC-derived NSCs (MTI-GlobalStem, GSC-4311) were proliferated on 1:200 diluted Geltrex (ThermoFisher Scientific, A1413302)-coated substrates with the NSC growth medium: Knockout DMEM/F12 (ThermoFisher Scientific, 12660-012), N2 (ThermoFisher Scientific, 17502048), bFGF (20 ng/ml; ThermoFisher Scientific, PHG0264), EGF (20 ng/ml; ThermoFisher Scientific, PHG0311), NEAA, and P/S. For the experiment, all NSCs were used under passage 6. The MN priming media was composed of: DMEM/F12 (ThermoFisher Scientific, 11330-033), supplemented with 15mM HEPES, GlutaMAX, N2, bFGF (10 ng/ml), heparin (2.5 μg/ml), LM (1 μg/ml), and niclosamide (0.125 μM); and the maturation media was composed of DMEM/F12, supplemented with 15 mM HEPES, GlutaMAX, and B27

(ThermoFisher Scientific, 17504044).

Professor Bin Xu's lab from the Columbia University kindly provided the iPSC-derived NPCs following the induction process of iPSCs to NPCs using the optimized dual SMAD-inhibition-based floor plate induction protocol (Kriks et al., 2011; Tomishima, 2012). NPCs were proliferated on the Matrigel-coated (1:100 diluted with a basal media) substrates with the proliferation media composed of DMEM/F12 (ThermoFisher Scientific, 11330-033) and neurobasal media (NBA; ThermoFisher Scientific, 21103-049) at 1:1, supplemented with N2, B27 (ThermoFisher Scientific, 12587010), NEAA, GlutaMAX, β-mercaptoethanol, and P/S. DA neuron differentiation media was based on neurobasal media, supplemented with GlutaMAX, B27, P/S, BDNF (20 ng/ml, Peprotech, 450-02B-10), ascorbic acid (200 μM), GDNF (20 ng/ml, Peprotech, 450-10B-10), cyclic adenosine monophosphate (cAMP; 500 μM; Millipore Sigma, 28745), TGF-β3 (1 ng/ml, Peprotech), DAPT (10 μM; R&D Systems, 2634/10), and CHIR99021 (3 μM; only added for the first 3 days of the induction process). Upon passaging both NSCs and NPCs, Y-27632 (10 μM) was added for the first 24 hrs to improve the single cell viability.

For direct lineage reprogramming to induced neurons (iNs), primary fHDF-GFP (P9) was kindly provided by Prof. Shim's group at DKU. These cells were maintained with DMEM-HG (ThermoFisher Scientific, 11995040), supplemented with 10% FBS, GlutaMAX, P/S, and β-mercaptoethanol. Additionally, following small molecule cocktails were used for this study as previously established in Hu *et al.* (Hu et al., 2015): Valproic acid (VPA; 0.5 mM; Calbiochem, 676380), CHIR99021 (3 μM; BioVision, 1677), Repsox (1 μM; BioVision, 1894), Forskolin (10 μM; Sigma, 3917), SP600125 (10 μM; Sigma, S5567), Gö 6983 (5 μM; Sigma, G1918), Y-27632 (5 μM), and Dorsormorphin (1 μM; Cayman, 11967). For abbreviation, only the first letter of each chemical name was used for denoting the chemical cocktails. Neuronal induction medium (NIM) was composed of a mixture of VCRFSGY in DMEM/F12

(ThermoFisher Scientific, 11330-032) and NBA at 1:1, supplemented with N2, B27 (ThermoFisher Scientific, 17504044), cAMP (100 μM), bFGF (20 ng/ml), and P/S. Neuronal maturation medium (NMM) was composed of CFD in DMEM/F12:Neurobasal media (1:1), N2, B27, cAMP (100 μM), bFGF (20 ng/ml), BDNF (20 ng/ml), GDNF (20 ng/ml), NT3 (20 ng/ml; Peprotech, 450-03-10) and P/S. All neural stem and progenitor cells were passaged with Accutase and used up to P6 for all the experiments.

4.2.4. Verification of cell viability and fate transitions of donor cells on in vitro culture platforms

The CCK-8 cell viability test (Dojindo) was conducted at the dilution of 1:10 with media to check the proliferation of NS/PCs on various substrates after 2 days. Upon 3 hours of incubating the live cells with CCK-8 dye at 37 °C, the plate reader was used to measuring the intensity of the formazan dye.

To check the cell morphology on graphene-based or PLG-based nontransparent substrates, differentiated MNs were fixed after 11 days and added with cold 2.5% glutaraldehyde for 120 mins. Then, it was post-fixed in 2% osmium tetroxide (EMS) for 60 mins and dehydrated using gradually increased concentrations of ethanol. Specimens were then dried under the chemical hood for overnight and sputter-coated with 5 nm gold/palladium. Cells were examined by SEM (Sigma VP, Zeiss) at 20 kV accelerating voltage.

4.2.5. Generation of terminally differentiated MNs and DA neurons and chemically iNs

For each differentiation or transdifferentiation protocol, lineage-specific chemically defined conditions with varying cell density were used to guide the cell fate to their target lineages, as depicted in Figure 29.

To yield MN differentiation, 100,000 to 150,000 cells were seeded for 12 mm-sized substrates. After 2-3 days of stabilization on the substrate, MN priming media was given for 4 days, followed by the maturation media for 2-9 days until analysis.

For obtaining DA neurons from iPSC-derived NPC cells, they were passaged from day 11 and seeded at the density of 150,000 to 200,000 cells per 12 mm-sized substrates. NPCs were replenished every other day with DA neuron differentiation media for at least two weeks until further analysis.

Initially, fHDF-GFP was seeded at the density of 12,000 cells per 12 mm-sized substrates and chemically iNs were generated by feeding fHDF-GFP with NIM for 8 days and replenishing it every 4 days. Then, NMM was given for the next two weeks and half-changed every other day until further analysis.

4.2.6. Assessment of differentiation and reprogramming efficiency

4.2.6.1. Confirming target neuronal signature by immunofluorescent staining and qRT-PCR

All staining procedure (8% PFA) was processed as mentioned above. The primary antibodies used here were anti-mouse Tuj1 (Covance, MMS-435P), anti-rabbit HB9 (Abcam, ab92606), and anti-mouse TH (Chemicon, MAB318) and anti-chicken MAP2 (Abcam, ab5392). The same secondary antibodies were used as mentioned in *3.2.3.3.* Images were taken by Nikon A1 confocal laser microscope system using the NIS-Elements. Quantitative image analyses were performed in 3 random view fields from the image using the Neurite Tracer extension from Image J.

For isolating total RNA, cells were detached from each (12 mm-sized) substrate by incubating 300 µl of Accumax for 30 mins followed by addition of 300 µl of collagenase IV for 30 mins. Detached cells were collected after centrifugation at 1000 rpm for 5 mins. Upon aspirating the supernatant, 300 µl TRIzol (ThermoFisher Scientific) was added to the cell pellets and the remainder of the substrate for extracting total RNA using the Quick-RNA Microprep Kit (Zymo Research). Subsequently, an equal volume of 70 % ethanol was added and thoroughly mixed loading the mixture to the column and follow the manufacturer's manual. The cDNA was synthesized from 500 ng of extracted RNA using the iScript cDNA synthesis kit (BioRad). As mentioned in *3.2.4.1,* qRT-PCR was conducted with the primers listed in

Table 4.

Table 4. The qRT-PCR primers used for identifying the maturation of MN and DA neurons

18s rRNA	Forward: GTA ACC CGT TGA ACC CCA TT
	Reverse: CCA TCC AAT CGG TAG TAG CG
MAP2	Forward: TTG GTG CCG AGT GAG AAG AA
	Reverse: GGT CTG GCA GTG GTT GGT TAA
OLIG2	Forward: GTTCTCCCCTGAGGCTTTTC
	Reverse: AGAAAAAGGTCATCGGGCTC
NKX6.1	Forward: GAGATGAAGACCCCGCTGTA
	Reverse: GACGACGACGAGGACGAG
ISL1	Forward: AGCAGCCCAATGACAAAACT
	Reverse: CTGAAAAATTGACCAGTTGCTG
HB9	Forward: GTCCACCGCGGGCATGATCC
	Reverse: TCTTCACCTGGGTCTCGGTGAGC
ChAT	Forward: ACT GGG TGT CTG AGT ACT GG
	Reverse: TTG GAA GCC ATT TTG ACT AT
TBR2	Forward: CACCGCCACCAAACTGAGAT
	Reverse: CGAACACATTGTAGTGGGCAG
GBX2	Forward: AAAGAGGGCTCGCTGCTC
	Reverse: ATCGCTCTCCAGCGAGAA
OCT4	Forward: GTGGAGGAAGCTGACAACAA
	Reverse: ATTCTCCAGGTTGCCTCTCA
NANOG	Forward: AAGGTCCCGGTCAAGAAACAG
	Reverse: CTTCTGCGTCACACCATTGC
OTX2	Forward: CAT GCA GAG GTC CTA TCC CAT
	Reverse: AAG CTG GGG ACT GAT TGA GAT
FOXA2	Forward: GGA GCA GCT ACT ATG CAG AGC
	Reverse: CGT GTT CAT GCC GTT CAT CC
LMX1A	Forward: ACG TCC GAG AAC CAT CTT GAC
	Reverse: CAC CAC CGT TTG TCT GAG C
NURR1	Forward: ACC ACT CTT CGG GAG AAT ACA
	Reverse: GGC ATT TGG TAC AAG CAA GGT
TH	Forward: GGG CTG TGT AAG CAG AAC G
	Reverse: AAG GCC CGA ATC TCA GGC T
PITX3	Forward: CCT ACG AGG AGG TGT ACC CC
	Reverse: CCC ACG TTG ACC GAG TTG A
DAT	Forward: TTT CTC CTG TCC GTC ATT GGC
	Reverse: AGC CCA CAC CTT TCA GTA TGG
EN1	Forward: GAG CGC AGG GCA CCA AAT A
	Reverse: AAT AAC GTG TGC AGT ACA CCC
GIRK2	Forward: CAC ATC AGC CGA GAT CGG AC
	Reverse: GGT AGC GAT AGG TCT CCC TCA

4.2.6.2. Quantification of neurite directionality and elongation by ImageJ

To quantify the alignment of the chemically induced neurons across each substrate, their directionalities were measured. Briefly, the fluorescent images of the fHDF-GFP, taken at the magnification of 4X, were used for each time point at Days 4, 8, 12, 16, and 20. Three or four microscopic fields around the center were used for analysis. Each image was converted to 8-bit greyscale and analysis was conducted by running the "Directionality" plugin (from ImageJ) using the Fourier component analysis (Liu, 1991) with the bin size of 90. Angle measurement was defaulted to measure in the direction from the positive x-axis to the positive y-axis. Collected massive data was plotted in a scatter plot in GraphPad Prism 6.

Total neurite length and average neurite length per cell were measured using "Morphology" and "Neurite tracer" plugins from Image J. This plugin has an excellent interface to perform neurite length measurements. Briefly, a black background will be saved in a working directory/folder to offset the background. As the neurites from the Tuj1$^+$ cells and from the DAPI$^+$ nuclei were measured, all the split channeled images were re-labeled based on the designed macro: "beta3Tublin_" and "DAPI_," respectively. Upon changing the name, all the added raw files were added to the working directory and the threshold size of the nuclei was set to avoid counting the artifacts throughout the analysis. After setting up the lower and upper threshold values, the analysis started and the system automatically found the neuronal cells extending neurites in various directions for tracing, which was later summed up for the total count of cells for quantifications. Post-analysis was conducted using Microsoft Excel.

4.2.7. Validation of cell functionality

4.2.7.1. Evaluating the functionality of the induced neurons via electrophysiology

In order to verify our differentiation protocol, the functionality of the motor neurons was evaluated by co-culturing them with the primary mouse astrocytes treated with cytosine arabinoside (Ara-C). Ara-C was used to prevent microglial contamination and the proliferation of astroglial cells. For this procedure, the P2 mouse astrocytes were kindly provided by Dr. Saera Song from Dr. Goldstein's lab. First, the 100,000 primary mouse astrocytes were seeded on a gelatin-coated 15 mm discs (as mentioned in *4.2.1.*) and fed with the same DMEM-HG media condition as used for culturing fHDF-GFP cells (as mentioned in *4.2.2.*) in a 12-well plate. Then, 10 µM of Ara-C was added to each well and replaced with fresh media on the next day. After cells were differentiated for 51 days, they were detached using the Accutase + Collagenase IV method (as described in *4.2.6.*) and 30,000 cells were seeded at the center of the astrocyte-seeded discs and cultured for 2 more additional weeks with the same differentiation medium. For the first day of co-culture, Rock inhibitor was added.

The electrophysiology test was conducted by Dr. Damian Williams from Dr. Boland's lab. The membrane potential recordings were performed using a Multiclamp 700B amplifier and a Digidata 1550 digital-to-analog converter (both from the Molecular Devices). Signals were filtered at 10 kHz with a low pass Bessell filter and digitized at a 10-kHz sample rate. The patch pipettes were constructed with a P-97 pipette puller (Sutter Instruments) using 1.5 mm outer diameter and 1.28 mm inner diameter filamented capillary glass (World Precision Instruments). The pipette resistance was 2 to 5 MΩ when filled with its recording solution. The external one was made of 145 mM NaCl, 5 mM KCl, 10 mM HEPES, 10 mM glucose, 2 mM $CaCl_2$, and 2 mM $MgCl_2$. The pH was maintained at 7.3 using NaOH and the osmolality was set to 325 mOsm using sucrose. The pipette solution consisted 130 mM CH_3KO_3S, 10 mM CH_3NaO_3S, 10 mM EGTA, 10 mM HEPES, 5 mM MgATP, 1 mM $CaCl_2$, and 0.5 mM Na_2GTP. The same pH was maintained as the external solution, but the osmolality was adjusted to 305 mOsm.

The experiments were all performed at RT and during recordings, current was injected to hold the cells at approximately -60 mV. The liquid junction potential across the pipette and external solutions was calculated empirically and the correction was applied before the experiment. The resting membrane potential (RMP) was measured immediately following the establishment of the whole-cell patching apparatus. Membrane resistance and capacitance were both calculated from the changes in membrane potential in response to hyperpolarizing current injection step, which increased incrementally by -4 pA, for 1 sec. Action potentials (APs) were evoked using 1-sec duration depolarizing current steps that increased incrementally by 4 pA. An AP was defined as a transient depolarization of the membrane, which had a minimum rise rate of more than 10 mV/ms and reached a peak amplitude of more than 0 mV. AP characteristics were measured from the first AP at rheobase. The AP threshold was measured at the point where the voltage increases at a rate higher than 10 ms/mV. The AP duration was calculated from the full width at the half-maximum voltage and the amplitude was measured from the threshold to the maximum potentials. The maximum number of AP was measured from a 1 sec current step. The amplitude of the step depended on the individual cell. Quantification was carried out using customized scripts for Igor Pro version 6 (Wavemetrics) and R version 3 (www.R-project.org). The electrophysiology results were based on randomly selected 19 cells from the control group.

4.2.7.2. Assessing the functionality of mDA neurons by dopamine release

After 35 days of DA neuron induction, to quantify the extracellular dopamine concentration from the media, two sets of differentiated cells were incubated with and without 300 µl of L-DOPA (reconstituted in 0.1 M of HCl and diluted in DMEM/F-12 medium supplied with N2 and B27) for 45 mins in the dark. For the untreated group, as a control, same basal media was added with equal volume as the L-DOPA treated group. After incubating for 45 mins, the media was aspirated, each well was rinsed with PBS twice, and incubated with 100 µl of Tyrode's salt buffer with 40 mM KCl for 5 mins. Then, 95 µl of the sample was collected and mixed with 0.2 M perchloric acid (Sigma) in a 1:1 ratio to protect the oxidization of released dopamine and stored at -80 °C for later use.

To measure the intracellular dopamine release, 50 µl of fresh Tyrode's salt buffer with 40 mM KCl was added to each well. Then, each well was triturated with the pipette and transferred to a tube. Additionally, 50 µl of fresh Tyrode's salt buffer was added to wash the well and transferred to a tube. The collected supernatant was divided in half: 1) from the first half of the sample, an equal volume of 70 µl of 0.2 M of perchloric acid was added, and 2) from the other half, 20 µl of the sample was collected for conducting the Picogreen DNA detection assay to normalize the dopamine concentration by the DNA content. To remove the cell debris, 1) sample was incubated on ice for 10 mins and spun down (at 10,000 *g*) for 5 mins at 4 °C. Then, the supernatant was collected and stored at -80 °C for later use. Both samples were stored for measuring extracellular and intracellular dopamine release utilizing the reversed-phase HPLC with electrochemical detection within 2 weeks of the collection, as described previously under the blinded condition (Steinbeck et al., 2015). All the experiments were conducted by Moshe Wilner at Prof. Eugene Mosharov's lab.

For visualizing cells on non-transparent graphene substrates, NSCs were transduced with pLV-hSyn-RFP (Addgene 22909), encoding lentivirus by following the established protocol (previously mentioned in ***Chapter 3.2.3***.). For lentiviral production, HEK293T/17 (ATCC, CRL-11268) was used. After testing the titer of the virus, the MOI test was conducted with and without protamine sulfate (4 µg/ml) as polybrene (8 µg/ml) was too toxic for NSCs to survive. Different concentrations of MOI were tested and the expression level of DsRed was also quantified using the following primer pairs normalized to the values of 18s rRNA:

- DsRed Forward: AGGACGTCATCAAGGAGTTC
- DsRed Reverse: TCTGGGTGCCCTCGTAG

4.2.8. Statistical Analysis

For statistics, all the values were presented as means ± stdev unless otherwise mentioned. For comparison, one-way or two-way ANOVA was used for comparing multiple groups with the *post hoc* analysis of Tukey's or Sidak's multiple comparison tests, respectively, using GraphPad Prism 6. Statistical significance was denoted as: * for $p < 0.05$, ** or ++ for $p < 0.01$, *** for $p < 0.001$, and **** for $p < 0.0001$.

4.3. Results and Discussion

4.3.1. Directed differentiation of iPSC-derived NS/PCs to MNs and DA neurons using physical and biochemical factors

4.3.1.1. Physical and biochemical factors to tailor cell fate to specific neuronal subtypes

To evaluate the effect of cell fate determination, highly electroactive substrates with two different features were fabricated using the 3D-printed method, as briefly illustrated in Figure 27A. This method allows economic, easy, and rapid fabrication of substrates at RT with varying patterns and materials. For mimicking the native features of neurons, two different substrates were utilized: 1) graphene:PLG cast sheet and 2) grooved 3DG with aligned patterns. For graphene's hydrophobic nature, oxygen plasma treatment was necessary prior to ECM protein-coatings for conferring hydrophilicity. ECM protein-coatings were utilized to mimic the niche-like conditions and support the cell's viability and subsequent directed differentiation process for both NS/PCs. Measuring the contact angles before and after oxygen plasma treatment confirmed the decrease in wettability (Figure 27B and Figure 27C) and subsequent ECM protein-coatings with PDL-LM and PLO-LM/FN (Figure 27D) were verified by LM staining for both sheet and 3DG. As the bulk property of graphene does not alter by surface modification with ECM proteins, the electroactive features were maintained even after the coating. Surface conductivity did not significantly change for the non-coated, LM-coated, and PDL-LM coated graphene substrates and maintained around 700 S/m (Figure 27E).

The physical and electroactive features of graphene:PLG sheet and 3DG substrates were verified by the FE-SEM, open/closed circuit test, and their XRD patterns (Figure 28). For confining the cell features to elongated morphology, aligned 3DG was utilized, as shown in Figure 28A. Unlike 3DG, graphene:PLG sheet portrays the random organization of graphene flakes on the cast sheet. However, as both substrates contain electroactive graphene flakes,

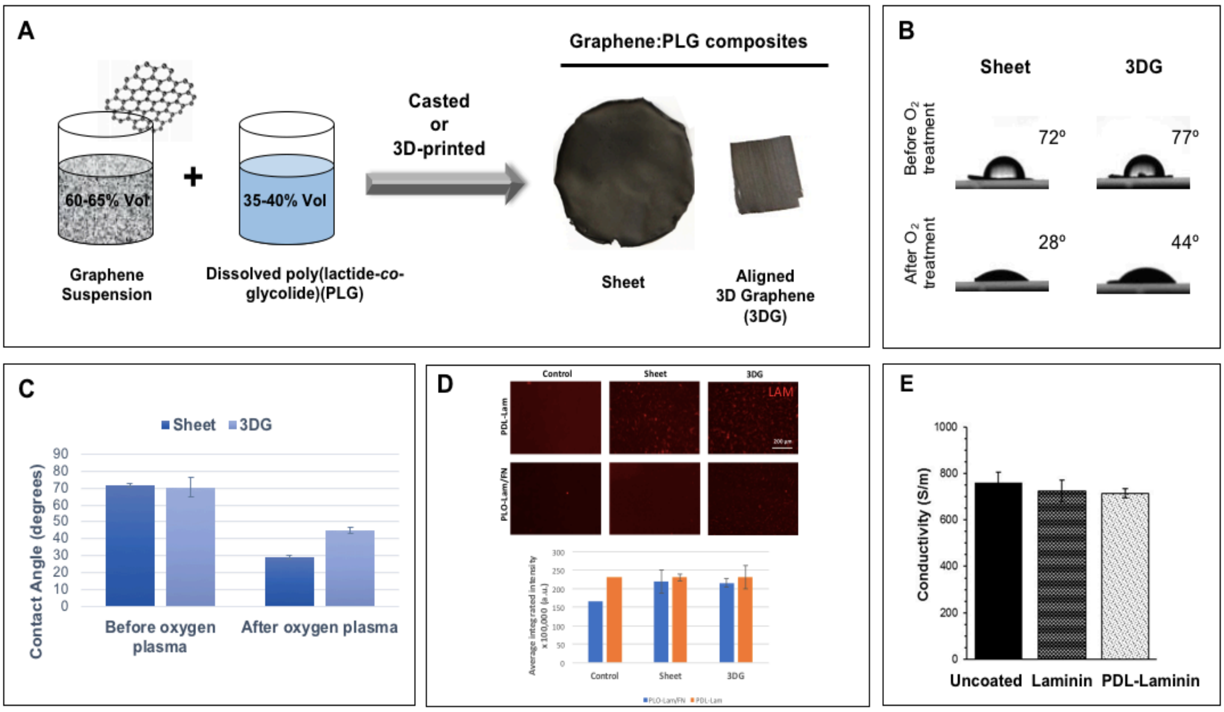

Figure 27. Fabrication and ECM protein coating of graphene substrates. Two different Graphene:PLG composites were used for the study: graphene:PLG-ink cast sheet, and 3D-printed 3DG sheet (A). Prior to protein coating, graphene:PLG composites were exposed to oxygen plasma to confer hydrophilicity (B). The contact angles before and after the oxygen plasma treatment were compared for both substrates (C). PDL-LM and PLO-LM/FN coatings were treated and quantified for the LM intensity compared to glass substrate (D). Change in substrate conductivity was measured before and after the LM or PDL-LM coating to confirm the change is not significant (E). LAM denotes LM. *n* = *3* for all the studies.

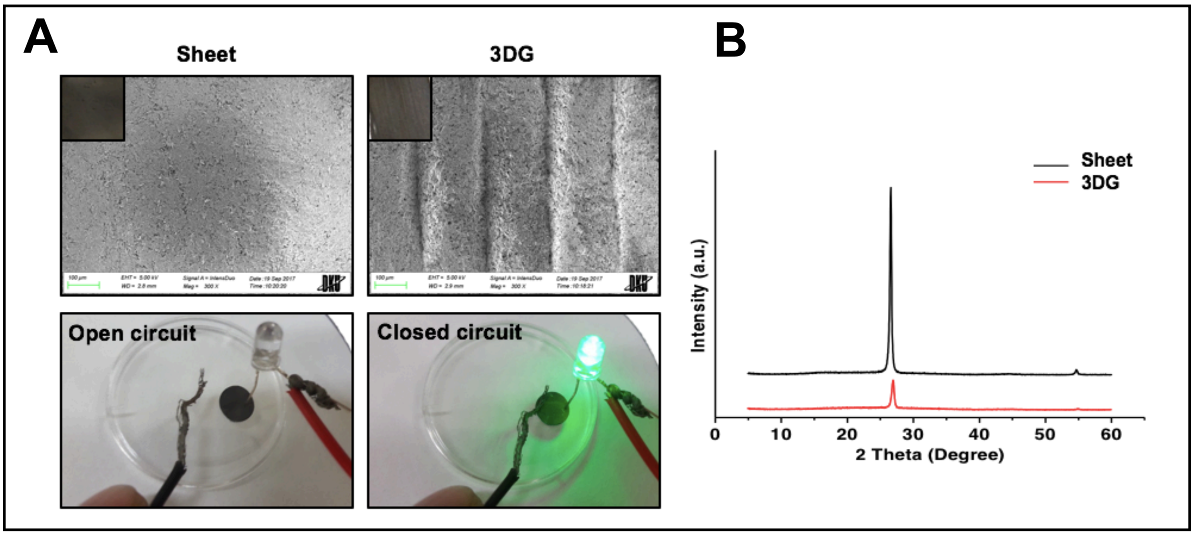

Figure 28. Characterization of graphene:PLG composites. FE-SEM analysis (top) to verify the patterns on each substrate and open/close circuit analysis to test the conductivity of the substrates with LED (bottom)(A). XRD patterns recorded for both substrates (B).

the LED light turned on when the wires were connected through the graphene composites in a closed circuit, indicating their high electric conductivity. Besides, the XRD patterns of both graphene composites were similarly indexed to the characteristic diffraction peaks of graphite, based on the Joint Committee on Powder Diffraction Standards card No. 12-0212, where prominent peaks are visible at $2\theta = 26.43$ and 54.51°. No additional noticeable diffraction patterns were observed, indicating the high purity of the fabricated graphene-based substrates.

With these culture platforms, we hypothesized that substrate-mediated biophysical cues along with soluble extrinsic factors could guide the uncommitted iPSC-derived NSCs and NPCs to target neuronal (MNs and DA neurons) subtypes, respectively (Figure 29). Preparation and formulation of biochemical cocktails and differentiation protocols were adapted accordingly from Jordan *et al.*, 2009, Natarajan *et al.*, 2014, and Kriks *et al.*, 2011.

Both donor cells for MN and DA neurons started from iPSC donor cells. For increasing the motor neuron specification, iPSC-derived NSCs were primed for 4 days with FGF, heparin, LM, and niclosamide (STAT3 inhibitor). The addition of niclosamide is known to block the activation of STAT3, thereby decreasing the astrocyte marker and increasing the MN-specific markers (Natarajan *et al.*, 2014).

After iPSCs were induced to NPCs, their genetic profile was identified to verify the plasticity/maturity level of NPCs, as shown in Figure 30. As the addition of biochemical factors was to obtain mDA neurons, instead of maintaining the pluripotent characters (OCT4 and NANOG), series of chemical cocktails upregulated the DA neuron-specific transcription factors compared to the control cells. This modified dual-SMAD inhibition (by exposing to LDN193189 and SB431542) protocol also led to the co-expression of FOXA2, the floor-plate marker, and LMX1A, the roof plate marker. Then, the treatment with purmorphamine and SHH is known to the downregulate FOXA2 and inhibits the expression of LMX1A. Upon the addition of CHIR99021 (GSK3 inhibitor), the WNT signal was activated and it upregulated

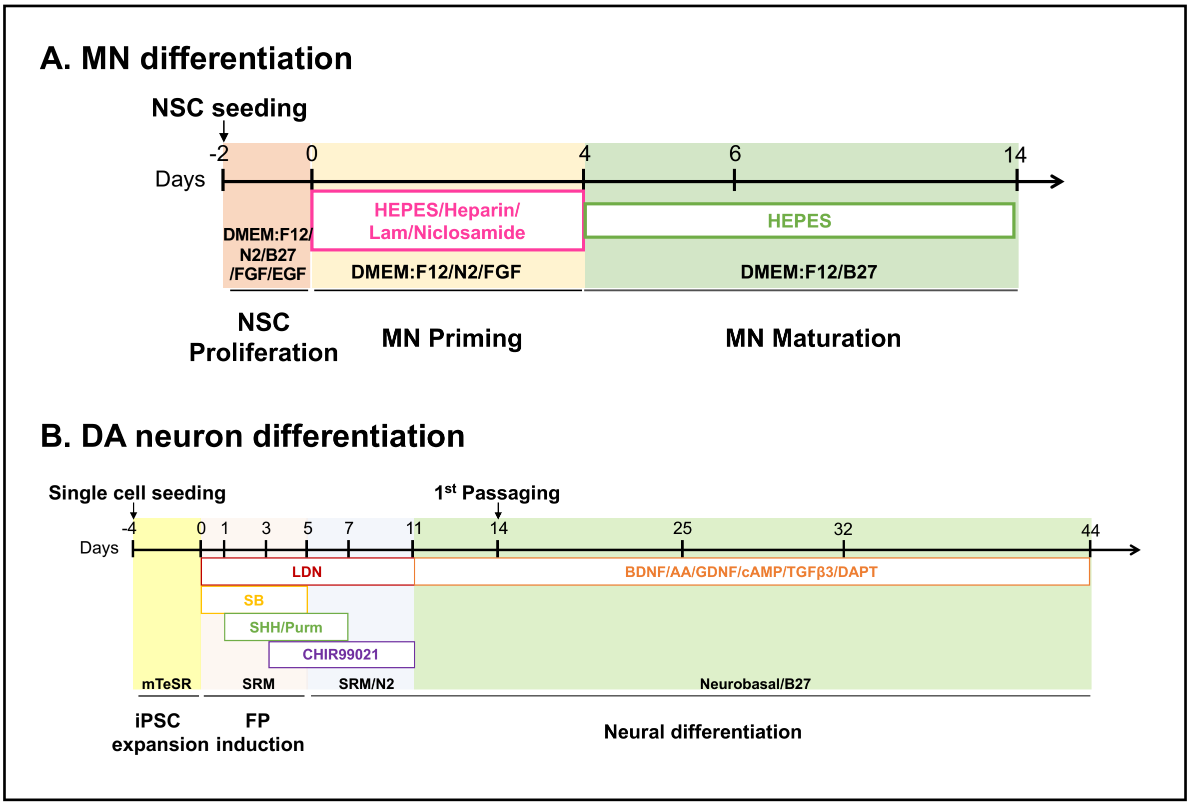

Figure 29. Soluble factors-mediated directed differentiation of iPSC-deirved NSCs to MNs (A) and iPSC-derived NPCs to DA neurons (B).

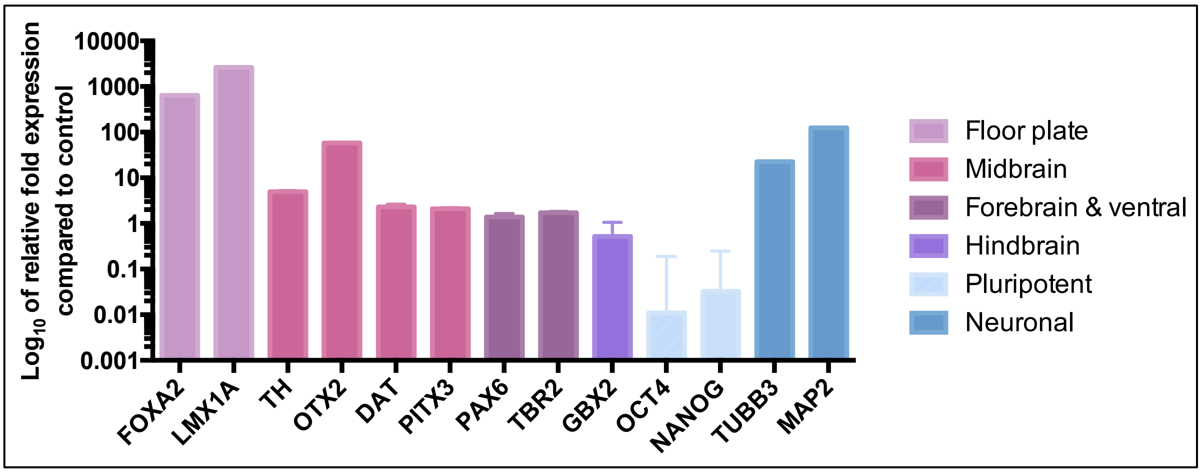

Figure 30. Relative gene expression level of the induced NPCs derived from iPSCs for a week compared to parental cells. Expression level was normalized with GAPDH. Abbreviations: FOXA2, Forkhead Box A2; LMX1A, LIM homeobox transcription factor 1 alpha; TH, tyrosine hydroxylase; OTX2, Orthodenticle Homeobox 2; DAT, dopamine transporter; PITX3, Paired Like Homeodomain 3; PAX6, paired box protein 6; TBR2, T-Box Brain Protein 2; GBX2, Gastrulation Brain Homeobox 2; OCT4, octamer-binding transcription factor 4; NANOG, homeobox protein NANOG; TUBB3, neuron-specific class III beta-tubulin; MAP2, microtubule-associated protein 2.

the anterior marker OTX2.

4.3.1.2. Cell viability and changes in cell morphology on various substrates

After fabricating the graphene:PLG composites and modulating the surface, the NS/PC viability and neural cell morphology were assessed using the CCK8 cell viability assay (Figure 31) and various microscopy techniques (light and fluorescence microscopes and SEM; Figure 32), respectively. After two days of cell seeding, no significant change in cell viability was observed for neither NSCs nor NPCs cultured on various culture platforms (Figure 31A). As graphene:PLG composites are non-transparent, the changes in cell morphology over time were observed for both directed differentiation to MN and DA neurons cultured on control TCPS substrates. As established from previous works, extrinsic factors led to a change in distinct cell morphology over time for both MN and DA neurons (Figure 31B).

Unlike DA neurons, for MNs, as the directional growth is pivotal for migrating electrical signals and reestablishing the neighboring neuronal connections (Shin *et al.,*2003), its morphology on graphene:PLG composites was confirmed using the FE-SEM (Figure 32). After 2 weeks of exposure to soluble factors and electroactive substrates, more mature neurons with thicker neurites were formed on graphene:PLG composites compared to the control. Interestingly, on the 3DG substrate, a higher density of processes outgrew with sophisticated connectivity and it was more structured along the patterns of 3DG. In contrast, on the sheet and control substrates, immature neurons were randomly organized with membrane protrusions, such as lamellipodia and filopodia.

For the non-electroactive substrate controls (PC and PA), cell viability was substantially lower, and a higher number of cell debris was observed compared to electroactive substrates. From the CCK8 assay, cell survival was verified for up to 2 days in the proliferation media. However, the long-term culture (2 weeks) of NSCs on the PLG-based substrates exhibited poor biocompatibility for MN differentiation and eliminated for further analyses.

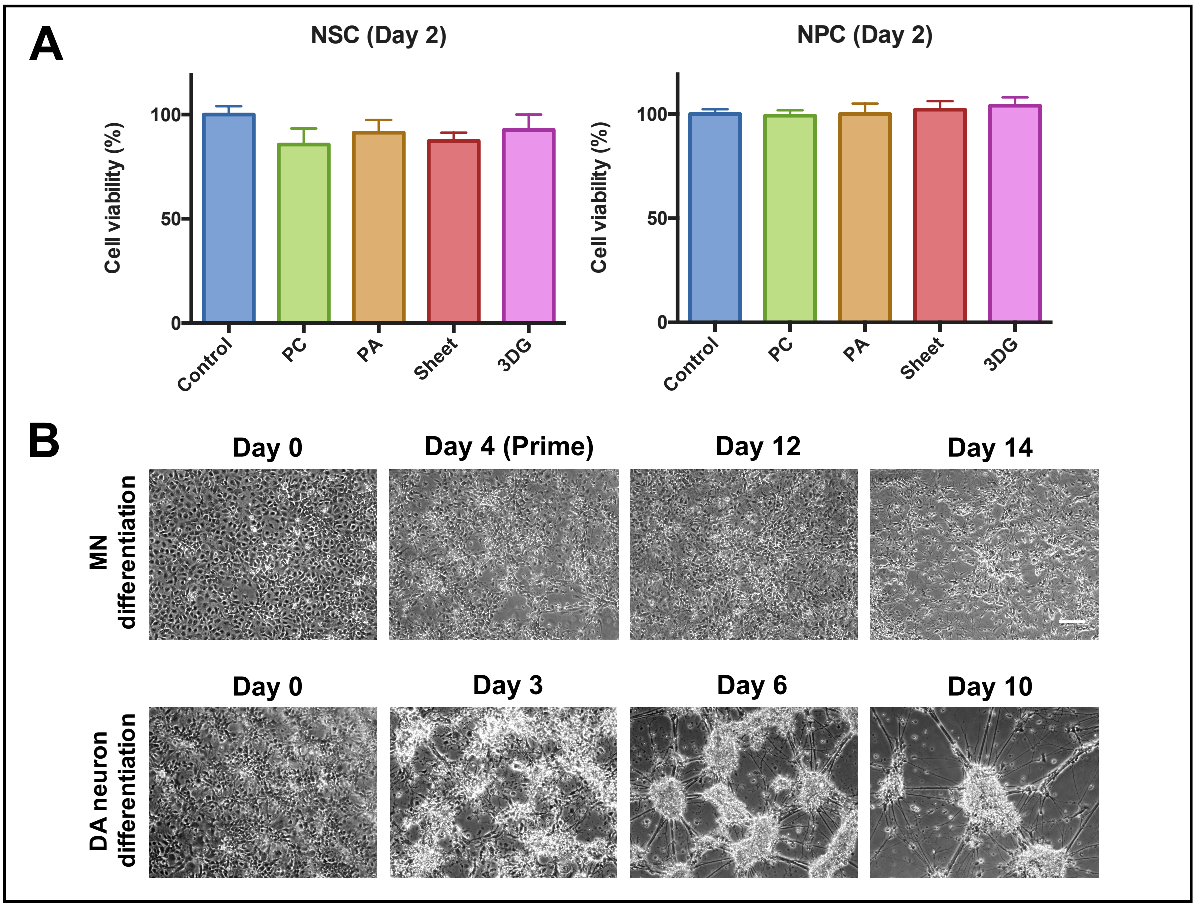

Figure 31. Cell viability and change in morphology for directing differentiation process for MN and DA neurons on various substrates. CCK-8 cell viability tested on different substrates over two days (A). Changes in cell morphology over time during the differentiation process on glass and TCPS for MN and DA neuron differentiation, respectively (B). Scale bar indicates 100 μm.

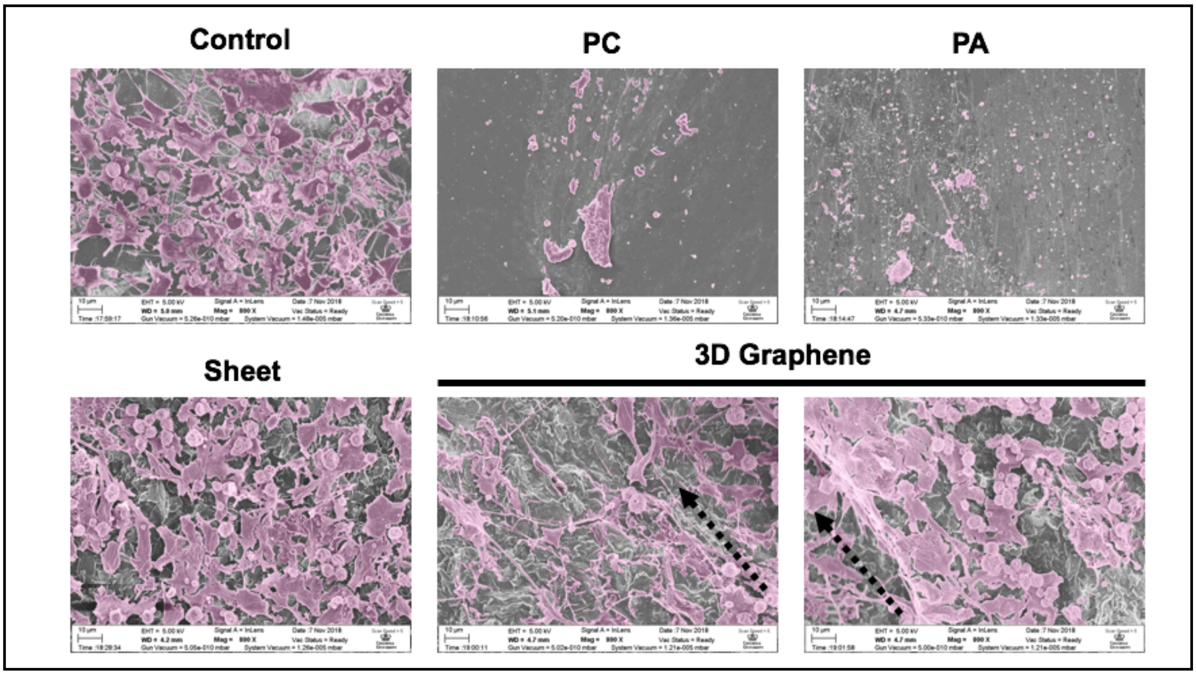

Figure 32. Pseudo-colored FE-SEM micrographs of differentiated MNs (in purple) for 14 days on various substrates. Dotted arrows indicate the direction of 3DG alignments.

4.3.1.3. Characterization of differentiated MNs and DA neurons

For verifying the identities and maturity levels of the differentiated subtype neurons, both immunofluorescent imaging and qRT-PCR analysis were evaluated.

After 6 days of differentiation, graphene substrates demonstrated more adhered Tuj1$^+$/HB9$^+$ mature MNs compared to control (Figure 33). Enhanced cell attachment was also well noted from the 3D-rendered video when MN aggregates were formed along the microgrooves of the patterned 3DG (Figure 34). Although both sheet and 3DG substrates are electroactive, much fewer cells were attached on the sheet (Figure 34A) compared to 3DG (Figure 34B). From the magnified image of the neural aggregates, it was observed that more adhesive contacts with neighboring cells were formed from the NSCs differentiated on 3DG (Figure 34C). As demonstrated from the SEM micrographs (Figure 32), extended neurite projections with the formation of axon-like features were identified in Figure 34D. It is not well known how cell density and substrate-mediated cell-cell interactions (contact cues from neighboring cells) instruct NSCs to mature neural subtypes, but it would be worthy of further investigation in the future. This would help to optimize the seeding density of the differentiation protocol for tailoring to the specific neuronal cell fate.

For immunofluorescent studies, MNs were matured up to 14 days to evaluate the effect of substrate-mediated physical cues on the cell fate conversion. As shown from Figure 35, compared to glass control, 0.4- and 1.9-fold more NKX6.1$^+$ cells, 2.8- and 9.5-fold more HB9$^+$ cells, and 3.6- and 10.2-fold more ChAT$^+$ cells were identified on sheet and 3DG, respectively. Based on the upregulation of these three somatic motor neuronal markers, 3DG exhibited a significantly more effective generation of mature MNs compared to that of the sheet.

Similarly, the 14-day of differentiated MNs cultured on highly conductive platforms were compared to their donor cells for verifying their gene expression signatures. All expression levels of MAP2, Olig2, NKX6.1, ISL-1, HB9, and ChAT markers were

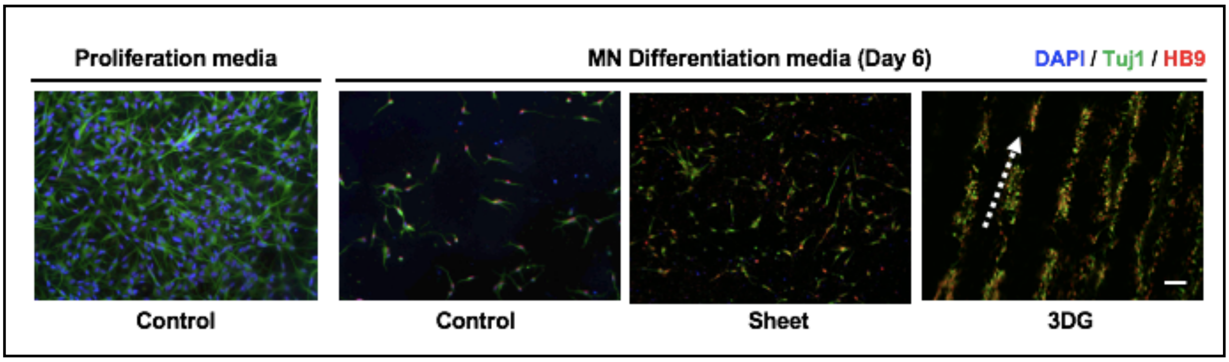

Figure 33. 3DG substrate supports cell adhesion and MN maturation. Scale bar indicates 100 µm. *Arrows indicate the direction of 3DG alignments

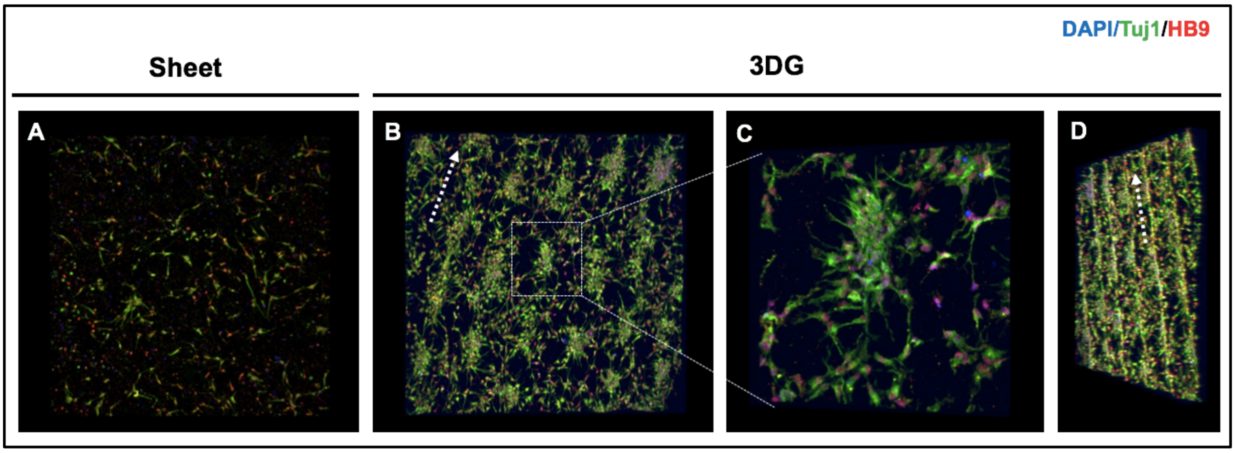

Figure 34. 3D-rendered images for the differentiated MNs cultured on graphene-based composites. Differentiated MN cultured on graphene sheet (A), and aligned 3DG (B) for 6 days. Englarged motor neuronal network on 3DG (C) and aligned neuronal network across the aligned 3DG (D). Dotted arrows indicate the alignment of the substrate

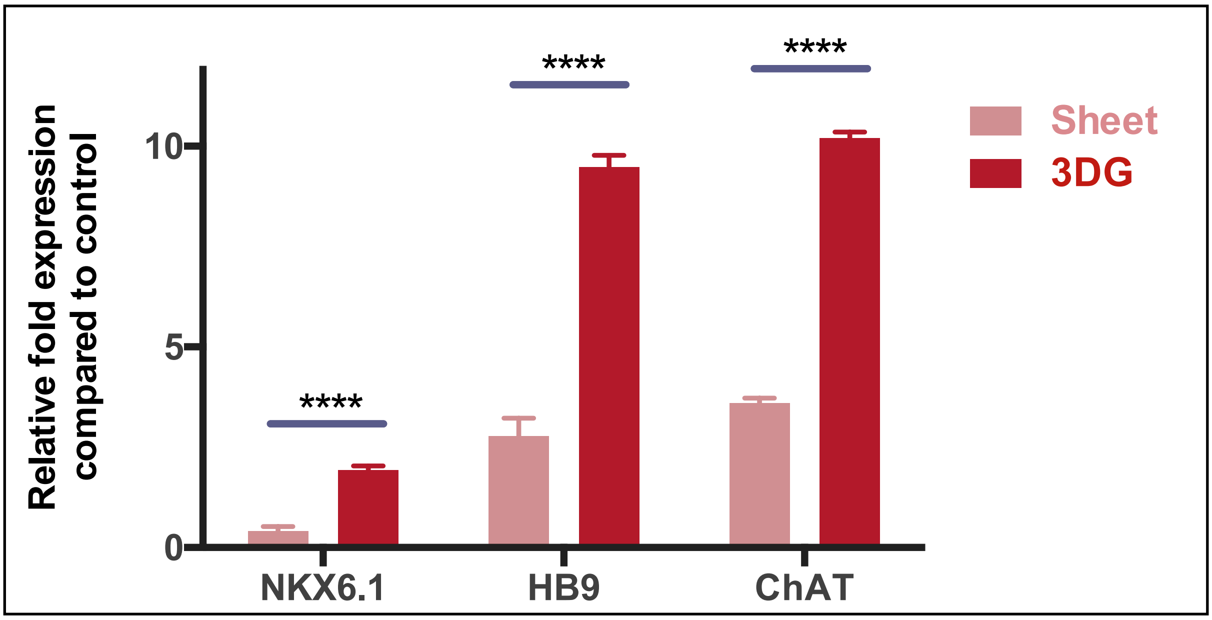

Figure 35. The relative gene expression level of differentiated MNs for 14 days compared to the control substrate (glass).

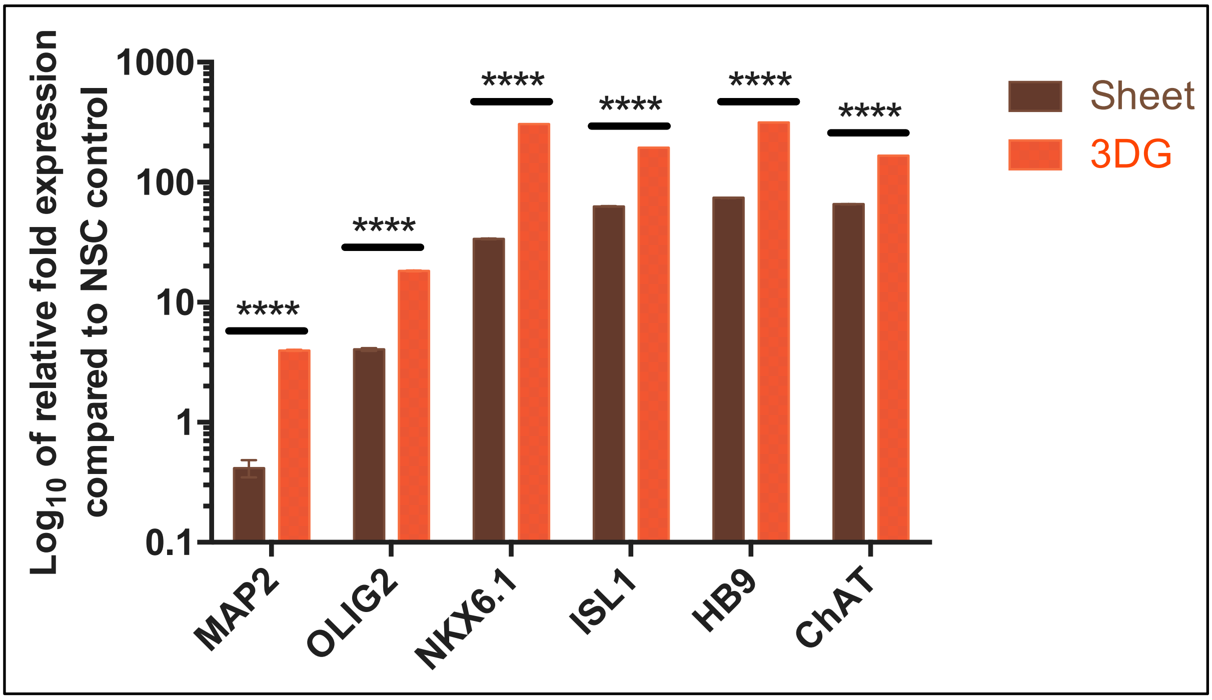

Figure 36. The relative gene expression level of differentiated MNs for 14 days compared to the original cell in log scale. Abbreviations: OLIG2, oligodendrocyte transcription factor 2; NKX6-1, NK6 homeobox 1; ISL1, ISL LIM homeobox 1; HB9, homeobox HB9; CHAT, choline o-acetyltransferase. **** indicates $p < 0.001$.

significantly upregulated in 3DG compared to the sheet (Figure 36). From this data, it can be speculated that the patterned substrate elevated the expression of both early and mature markers of MNs, thereby activating the MN program and increasing the differentiation efficiency. Moreover, the results suggested a greater influence of micropattern-mediated physical cues on the maturation of MNs compared to culturing the cells on a highly conductive substrate (sheet).

Similarly, the effect of substrate-mediated biophysical cues was examined for the directed differentiation of NPCs to DA neurons. While they naturally exist as 3D spheres in their niche environment, to investigate the feasibility of using the electroactive culture platform instead of the traditional platform, Kriks' protocol was adapted (Kriks *et al.*, 2011). After confirming the morphology change by adding the biochemical factors (Figure 31B), 11-day differentiated DA neurons were characterized with their mature marker, tyrosine hydroxylase (TH) and mature neuronal marker MAP2 (Figure 37). Unlike the alignment of MN aggregates along the microgrooves of 3DG, DA neurons did not seem to get influenced by the microgroove-mediated physical cues. As shown in Figure 37, the white dotted arrow indicates the direction of the microgrooves. Rather than forming structured neurites along the arrow, DA neurons formed a web-like structure with the neighboring cells throughout the 3DG substrate, which resembled the sophisticated connectivity and neurite extension patterns from the other substrates (control and sheet). However, TH^+ DA neurons were only observed on the electroactive substrates (Figure 37). Moreover, compared to cells cultured on the TCPS control, 18-day differentiated mDA neurons cultured on graphene:PLG composites possessed the genetic profile (both expressing early and late markers of mDA neurons) of mDA neurons (Figure 38). Similar to the results from the MN differentiation, for DA neuron differentiation, 3DG significantly reinforced the cell fate conversion of NPCs to mDA neurons compared to the sheet by 3.75-fold.

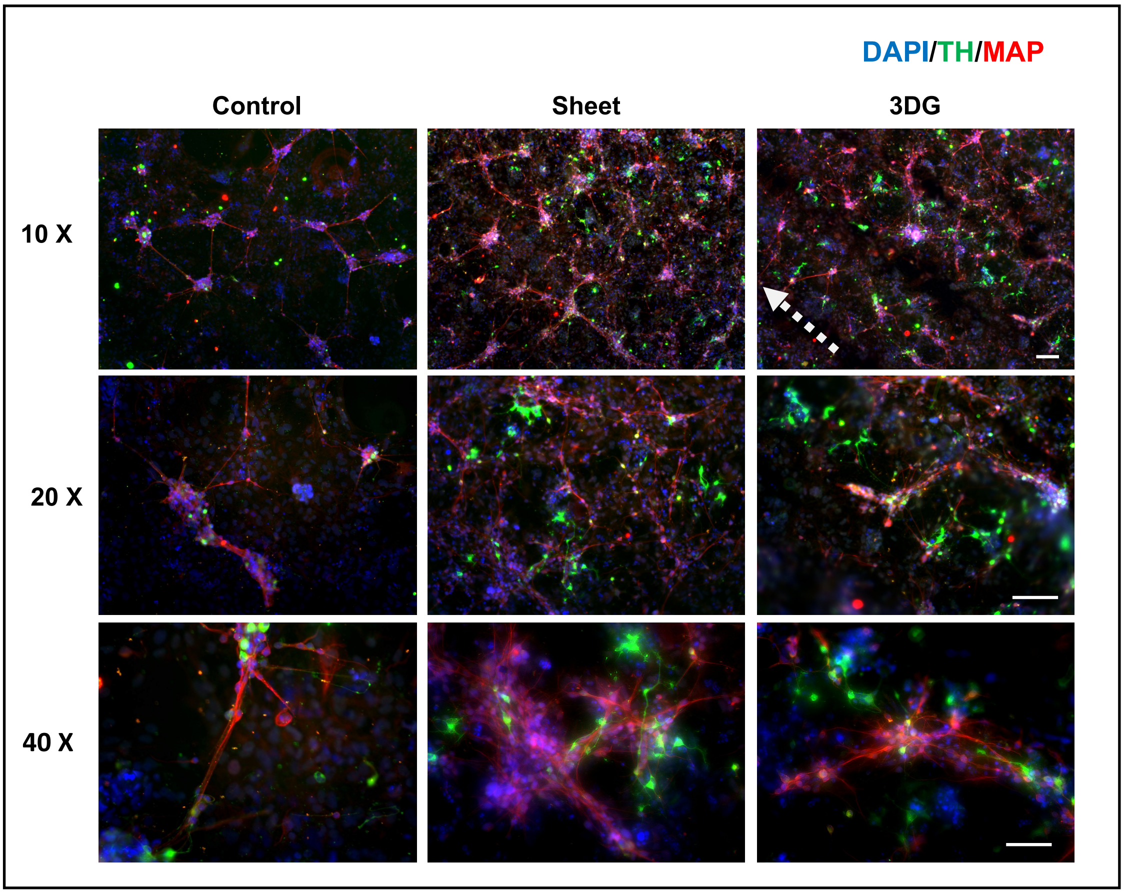

Figure 37. Mature marker expression of differentiated DA neurons for 11 days on various substrates. White dotted arrow indicated the alignment of the substrate. Scale bar indicates 100 µm for top two and 50 µm for bottom.

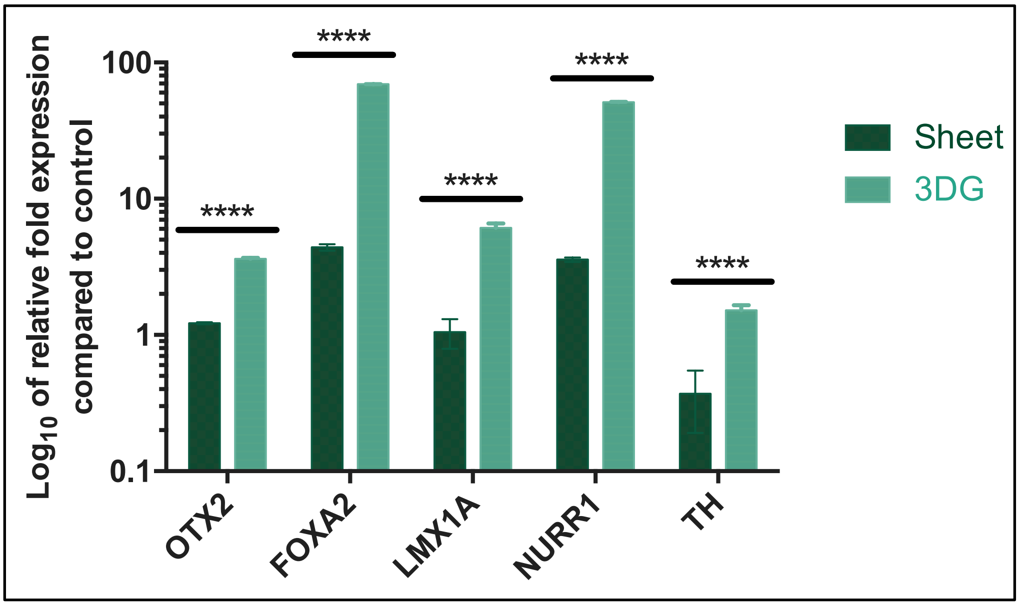

Figure 38. Relative gene expression level of differentiated DA neurons for 18 days of expression level compared to the control substrate in log scale. Abbreviations: NURR1, Nuclear receptor related 1 protein. Control was TCPS. **** indicates $p < 0.001$.

4.3.1.4. Verifying the signatures of the mature MNs and DA neurons

The induction of target cell fate conversion was verified from the morphology change and the protein and gene expression of the mature MN and DA neuronal markers. In order to fully recapitulate the *bona fide* mature subtype neurons, in this chapter, it was attempted to verify the functionality of these cells.

For mature MNs, they were either co-cultured with the C2C12, an immortalized murine myoblast, or the primary mouse astrocytes to mimic their niche environments and maintain the stability of the cells to quantify their electrical excitability. However, due to the vigorous beating of the mature C2C12 myofibers upon seeding the mature MNs, muscle fibers were torn apart and it was not feasible to continue the functional evaluation of MNs (data not shown). While, for co-culturing with the primary murine astrocytes, due to the secure attachment of MNs on the graphene-based substrates, it was challenging to isolate MNs from the graphene substrates and culture them till the point of analysis. Therefore, only the cells co-cultured with astrocytes on the control substrate survived the additional two weeks of differentiation and evaluated for its functionality, including the patterns of action potential (AP) spikes, membrane properties, and other AP characteristic measurements (Figure 39, Figure 40, and Figure 41, and Table 5). A total of 42% of the selected mature motor neurons fired multiple AP spikes as shown in Figure 39, but the rest of other immature neurons fired few AP or aborted AP spikes. Along with the AP spikes, the average resting membrane potential (RMP) was measured as -38.3 mV, where mature neurons typically indicate RMP of -60 mV. Overall, these results collectively represented that our directed differentiated protocol to MNs was not efficient.

For DA neurons, both the intracellular and extracellular DA concentrations were measured and normalized to the DNA content calculated from the mature DA neurons (Figure 42). The results demonstrated that 3DG platform significantly elevated both the intracellular

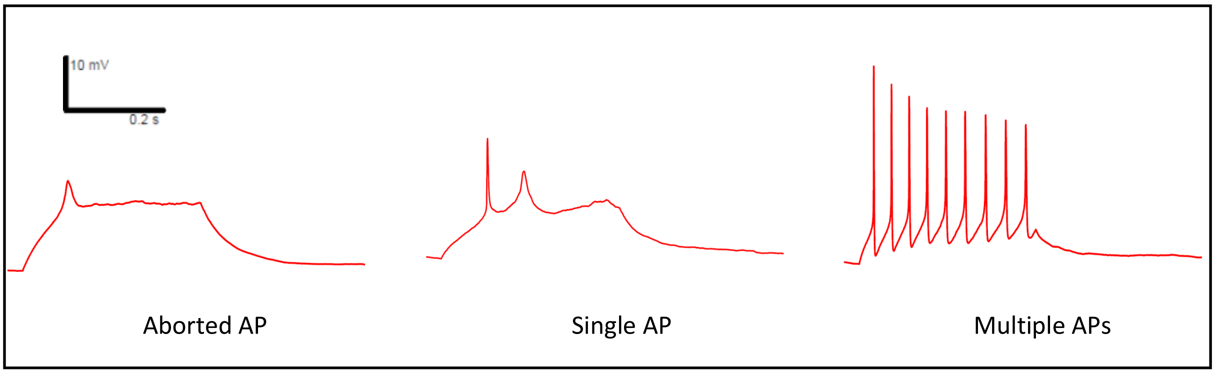

Figure 39. Different patterns of AP spikes recorded from the iPSC-derived MNs, directly differentiated for an extended period. Recordings are in the order of aborted AP signal, single AP spike, and functional MNs firing multiple AP spikes where y-axis is 10 mV and x-axis is during 200 ms.

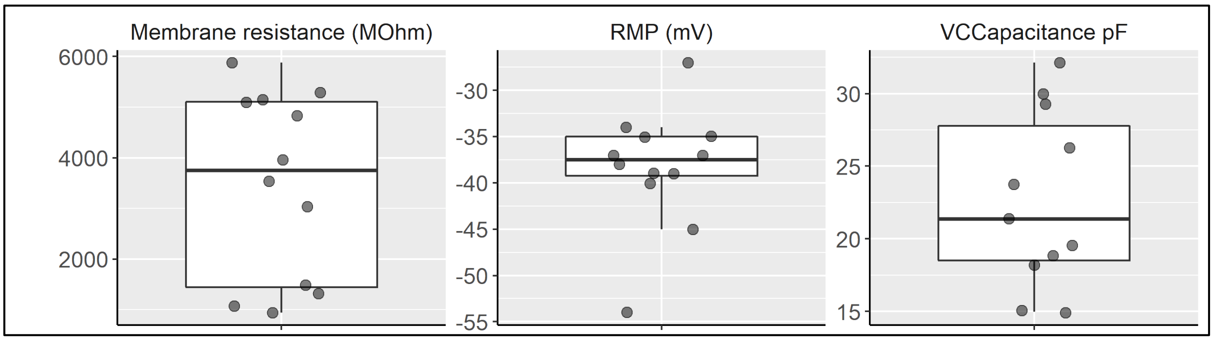

Figure 40. A box and whisker plots of the passive membrane properties of the differentiated MNs in the order of membrane resistance (mOhm), RMP (mV), and the capacitance across voltage (pF).

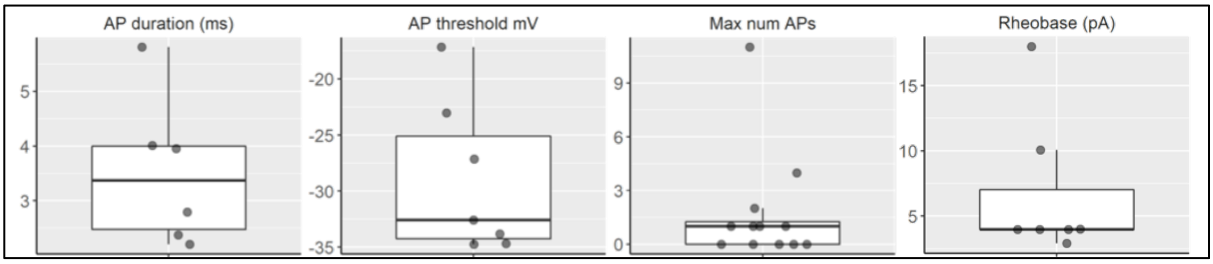

Figure 41. A box and whisker plots of the AP characteristics of the differentiated MNs in the order of AP duration (ms), AP threshold (mV), maximum number of APs, and rheobase (pA).

Table 5. Summary of the quantified electrophysiology results from the iPSC-derived MNs

Measurement	Mean	Standard error	n
Capacitance (pF)	22.68	1.82	11
Membrane resistance (MOhm)	3467.84	533.29	12
RMP (mV)	-38.33	1.88	12
Max number of APs	1.75	0.91	12
AP duration (ms)	3.52	0.55	6
AP threshold (mV)	-29.02	2.58	7
Rheobase (pA)	6.70	2.09	7

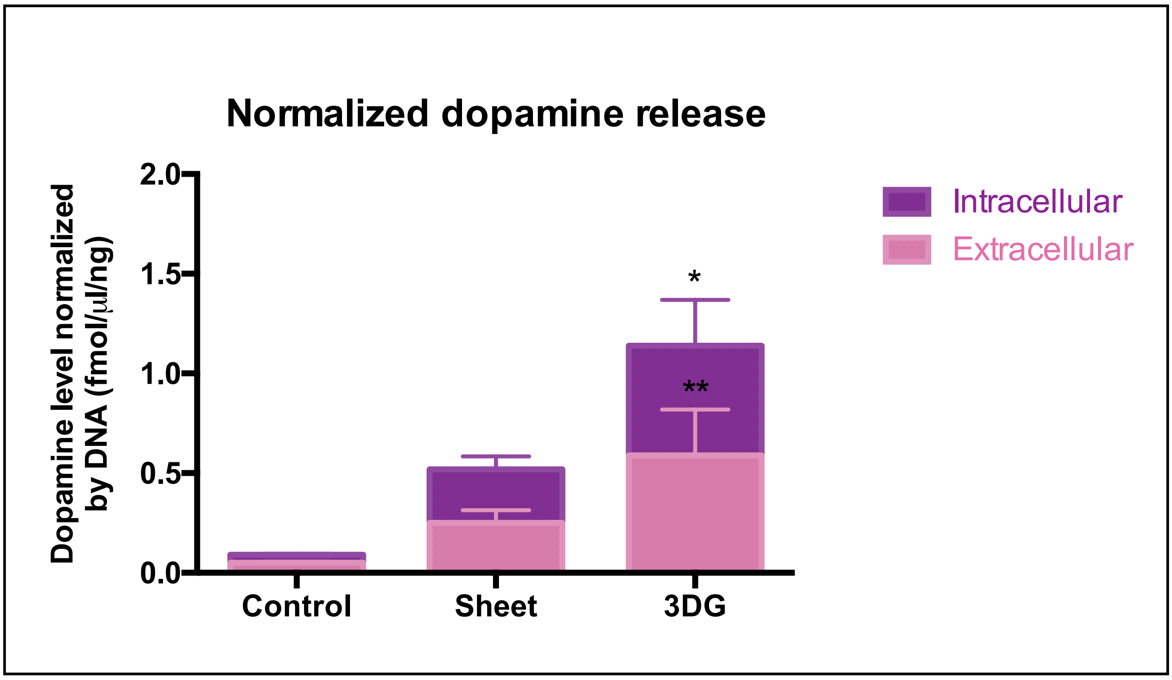

Figure 42. Normalized HPLC analysis results for measuring the intracellular and extracellular dopamine release from the mature DA neurons after 35 days of differentiation. Total DNA content was measured by the Picogreen Assay. ** indicates $p < 0.01$ and * indicates $p < 0.05$

and extracellular concentration of DA from DA neurons after 35 days of long-term differentiation.

Compared to the sheet, 3DG had an approximately 2-fold increase in both intracellular and extracellular DA concentrations. Therefore, more neuronal connectivity expressing TH^+ DA neurons attributed to the higher maturity and functionality of the DA neurons. How the higher cell attachments on the aligned microgrooved patterns of the 3DG directly contributed to the improvement of functionality was not systemically assessed in this study. However, it would be interesting to further investigate in the future.

Instead of pursuing other options to verify the correlation between the cell seeding density and its cell fate conversion efficiency, a pilot study was conducted to visualize the mature MNs on the graphene substrates using the pLV-hSyn-RFP lentiviral plasmid. Cells infected with the lentivirus bearing the plasmid expressed RFP upon the expression of human synapsin (Figure 43). Protamine sulfate (PS) was added at a lower dosage over a range of MOIs in order to increase the efficiency of lentiviral infection. Based on the increasing MOI dosage, the RFP expression significantly increased proportionally, quantified by the expression of DsRed from the qRT-PCR (Figure 44). However, similarly, as the mature MNs were unable to be fully detached from the substrate, the majority of the RFP expressing MNs were still attached to the substrate after the detachment procedure. For further assessment of the cell functionality, a more optimized detachment procedure should be established to pursue the patch-clamp study on the cells cultured on graphene-based substrates.

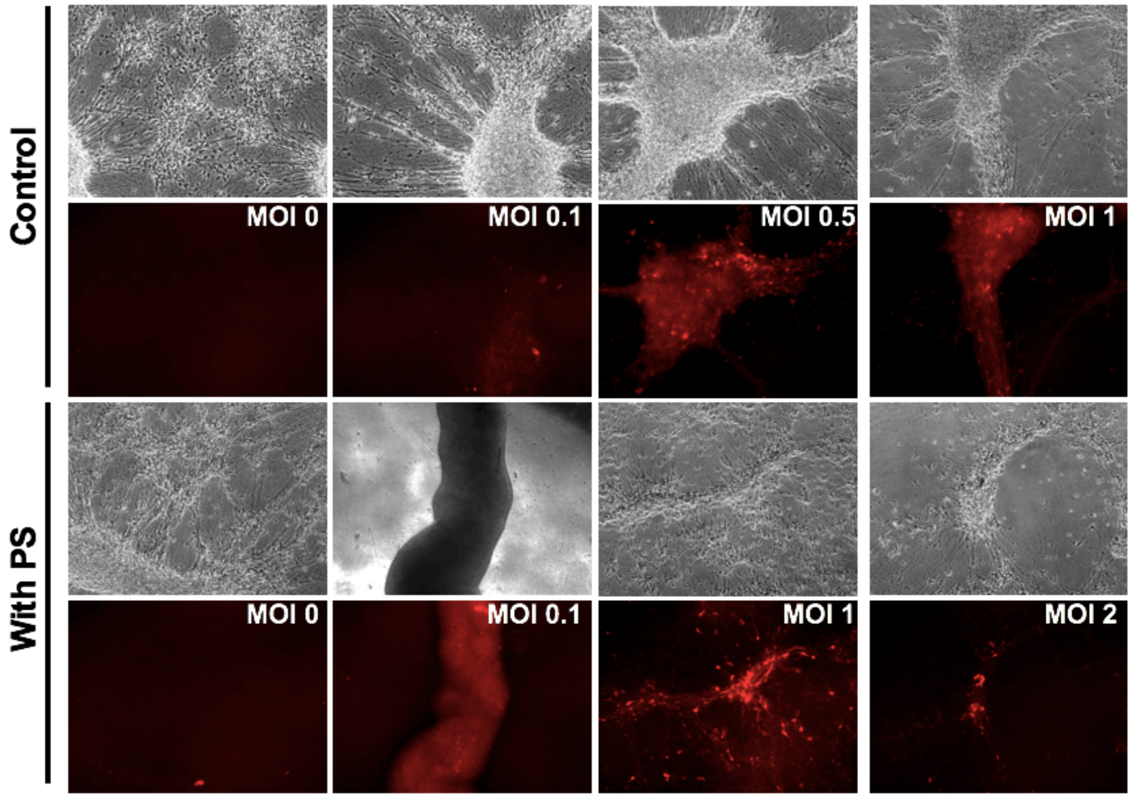

Figure 43. Lentiviral titer test for infecting NSCs with lentiviral encoding hSyn-RFP with and without protamine sulfate (PS).

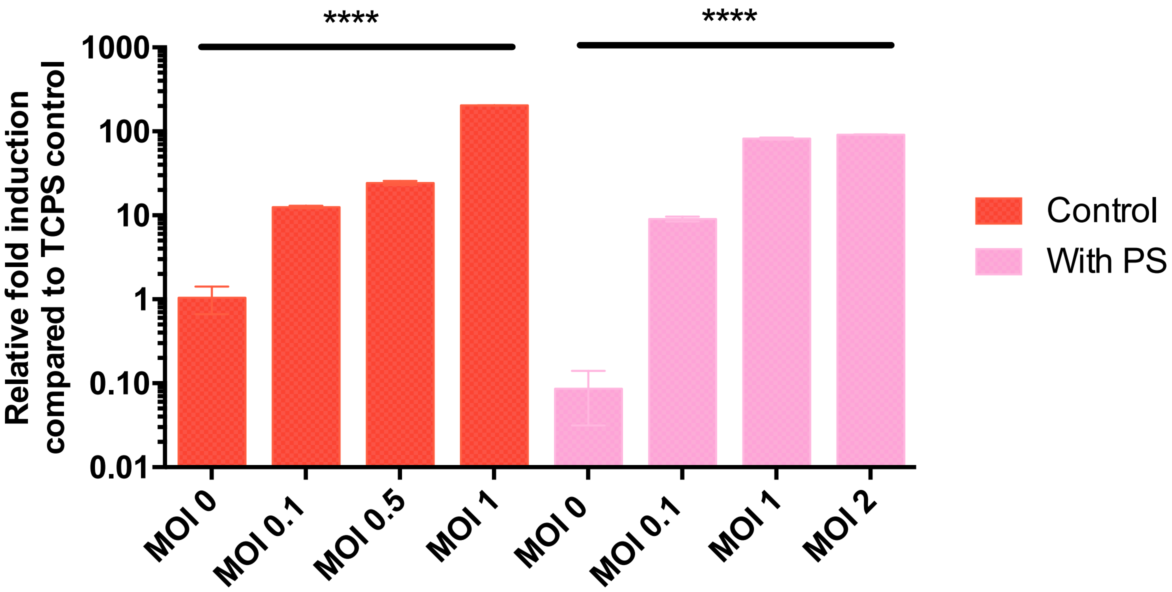

Figure 44. Quantification of the dose-responded RFP gene expression as the MOI increased. **** indicates $p < 0.001$.

4.3.2. Transdifferentiation of chemically-induced neurons

In addition to promoting the differentiation of the NS/PCs to target neuronal subtypes, in the second half of the project, we investigated if this highly electroactive substrate can also enhance direct conversion of fibroblasts to chemically-induced neurons. Small molecule mediated direct reprogramming is more advantageous over traditional lineage conversion procedures involving delivery of TFs because of the following advantages: 1) they are stable, cell-permeable, and easy to prepare; 2) they are safe as they obviate the need of using virus as a delivery vehicle; 3) they allow simple, rapid, and cost-effective method to epigenetically convert the cell fate; and 4) they allow the cell phenotype to be finely tuned by modulating their concentrations and lengths of exposure to donor cells. For our study, 8 chemical cocktails were exposed to fHDF-GFP at different time points to promote its conversion to neuronal lineage (Figure 45). Neural induction media promotes the neuronal conversion of fibroblasts and maturation media promotes survival and maturation of induced neurons.

Over 20 days, changes in cell morphology and neurite elongations implied that 3DG promoted the adhesion and aligned growth of chemically-induced iNs along the micropatterns compared to the control and the sheet substrates (Figure 46A). The neurite orientation of the cells was quantified based on the preferred spatial orientation of cells represented as an angle measured from the positive y-axis position, where 0° indicated the horizontal axis (Figure 46B). As shown in Figure 46C, the iNs from control and the sheet spread out randomly in multiple directions with directionality ranging from -181 to 73°, while the iNs on the 3DG had less than 10° dispersions in their preferred growth orientation throughout the differentiation process. Such results suggested that iNs on 3DG preferred aligning and extending along the microgrooved patterns.

In order to confirm the pan-neuronal marker of the transdifferentiated iNs, cells were stained with Tuj1 and quantified for their neurite lengths (Figure 47). In the early phase of lineage conversion, it was interesting to note the distinctive mixtures of heterogeneous cell populations; the green-colored fhDF-GFP, which did not fully transdifferentiated into iNs, and the red-colored Tuj1$^+$ cells, including both chemically induced immature and mature neurons. After the neural induction stage, due to the chemical cocktails inducing the neural maturation, more populations of Tuj1$^+$ iNs were observed over the GFP$^+$ populations (Figure 47A).

ICC data also suggested that the iNs from the 3DG had longer total neurite lengths compared to other substrates at Day 16 and the average neurite length per cell was significantly enhanced at the early stage of induction on 3DG (Figure 47B). During the neural induction, all the substrates well supported the lineage conversions of fhDF-GFP. However, during the neural maturation period, the addition of MM triggered more cell deaths, which implied the lack of mature iNs on the other substrates compared to 3DG. Besides, the discrepancy over the cell seeding density might have caused by the increase in passage number of the primary fhDF-GFP. Such an uncontrollable parameter affected the cell behaviors significantly, although only the passage number below 10 was used for the study.

Collectively, the results of specific aim 2 implied that 3DG might serve as a potential platform for neural cell cultures. Interestingly, graphene with the aligned micropatterns (3DG) had a more significant effect on guiding cells to neuronal phenotypes compared to having graphene sheets. However, to make a conclusive summary, more tests need to be conducted to confirm the functionality of these neurons and other heterogeneous cell populations on these substrates.

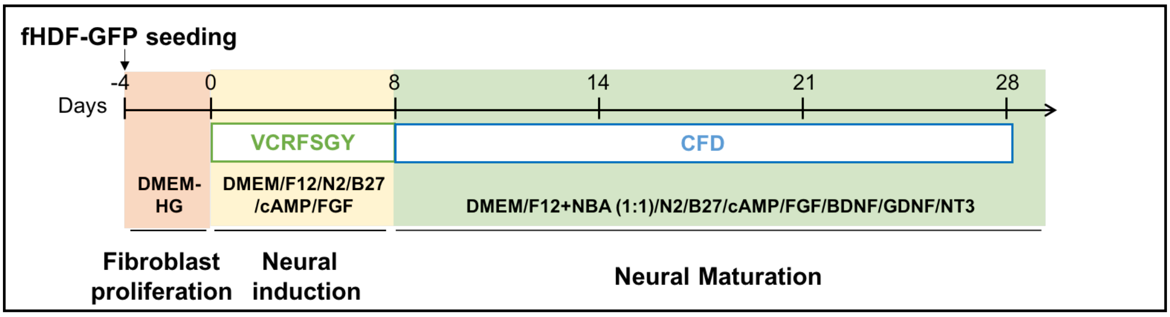

Figure 45. Chemical factor-induced lineage conversion schedule for generating iNs from fHDF-GFP.

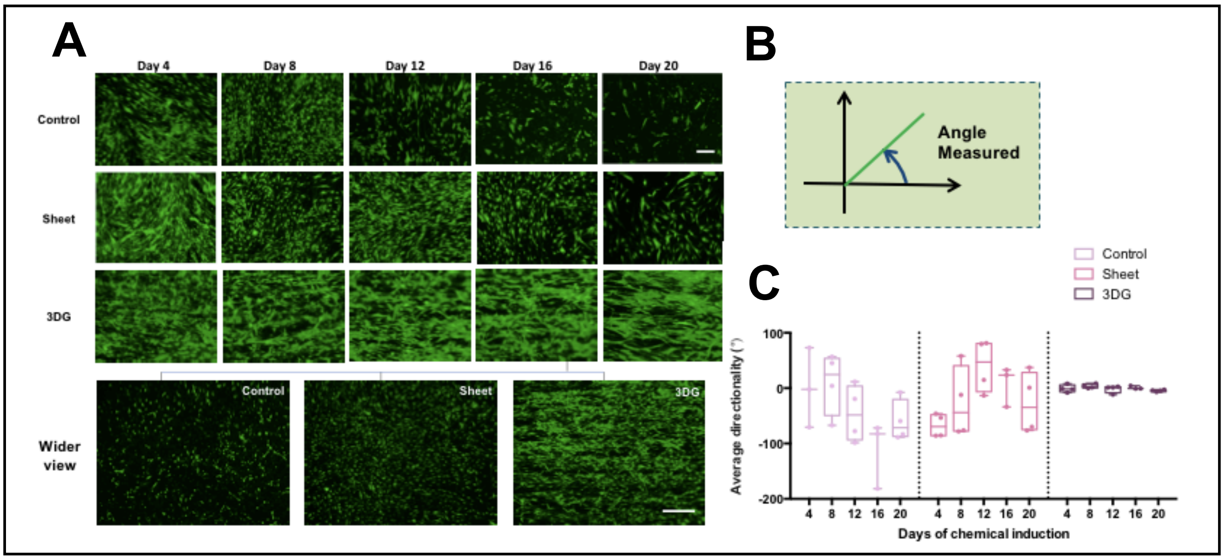

Figure 46. Epigenetically-reprogrammed iNs using chemical cocktails. Change in cell morphology (A), how the directionality angle was measured (B), and the resulting directionality (C) of iNs over time for each substrate ($n = 3$-4). Scale bar indicates 200 (top; for 10X) and 600 µm (bottom; for 4X).

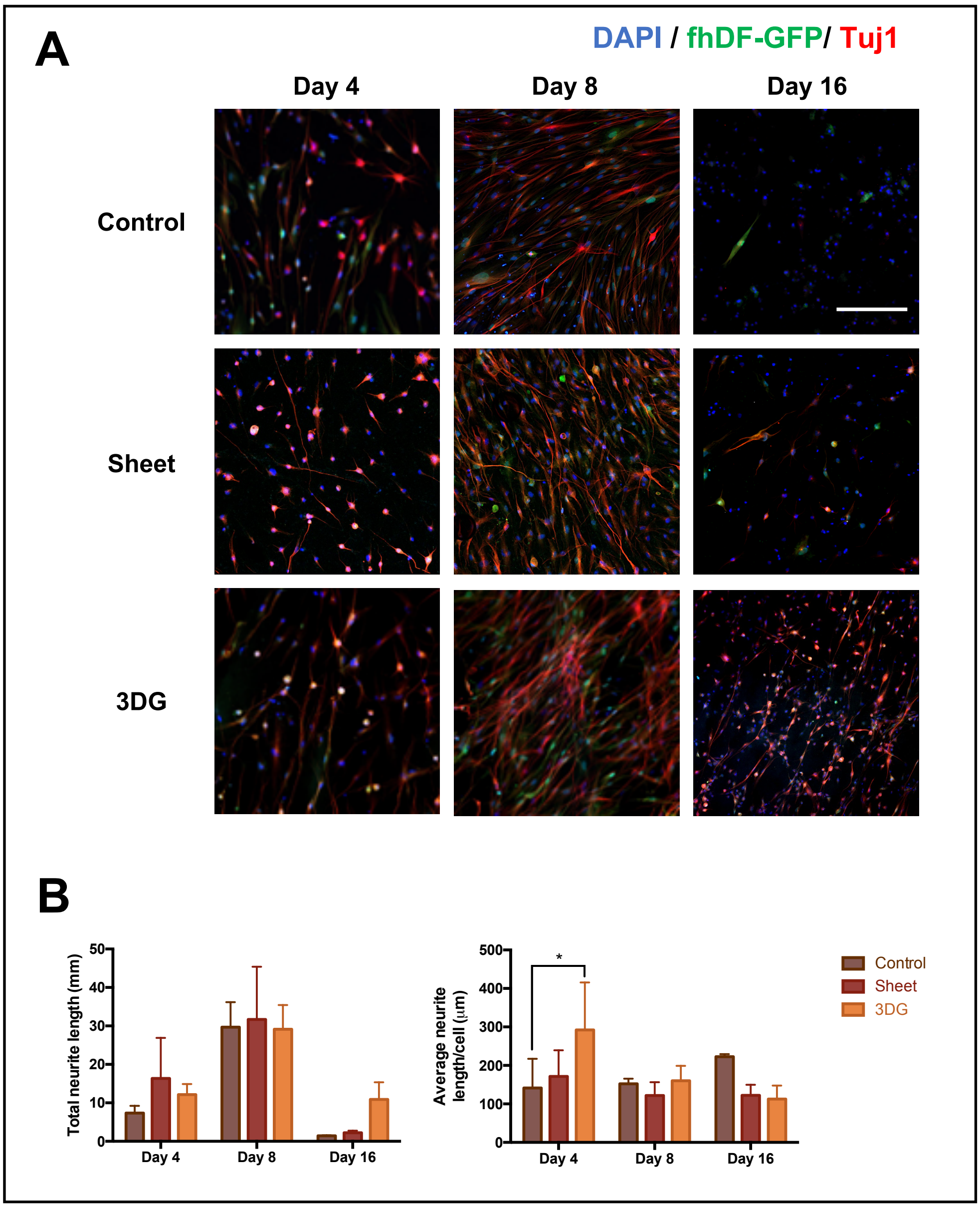

Figure 47. Small molecule-mediated direct lineage conversion of fhDF-GFP to iNs. Pan-neuronal marker expression from iNs across various substrates (A) and the total neurite length and average neurite length per cell (B). Scale bar indicates 200 µm. * indicates $p < 0.05$.

Chapter 5: Summarized conclusion and future perspectives

5.1. Summarized Conclusion

Programming one cell fate to another target cell lineage provides tremendous opportunities for utilizing these therapeutic cells, 1) directly as potential sources for cell-based therapy to treat inoperable diseases in the neuronal and muscular systems, or 2) indirectly to recapitulate the dynamic neuronal and muscular programs for developing drugs for specific diseases. Both applications are exciting enough for both researchers and patients as either application can lead to optimal personalized medicine if patients' cells could be used as a cell source. In this aspect, in **Chapter 3.** *In situ* reprogramming of EPCs by transactivation of endogenous *MYOD1* using the CRISPR/dCas9 system and **Chapter** 4. Enhancing the neural cell fate commitment by deploying biochemical cues and substrate-mediated electrophysical cues, we attempted to guide the origin cell fate of both stem/progenitor and somatic cells into iSkMs, MNs, DA neurons, and iNs by mimicking their niche in the neuronal and muscular systems. From both aims, we learned the combinations of intrinsic and extrinsic signals lower the epigenetic barriers to promote the myogenic and neuronal cell fate conversions.

5.1.1. Conclusion for Chapter 3

In **Chapter 3.** *In situ* reprogramming of EPCs by transactivation of endogenous *MYOD1* using the CRISPR/dCas9 system, we first demonstrated utilizing the CRISPR/dCas9-mediated targeted transcriptional system to instruct EPC fate to committed iSkM *in situ*. As we hypothesized, only by inducing transdifferentiation of EPCs (with the administration of dox), resulting iSkM integrated to the host tissue, promoted 2-fold elevated level in local angiogenesis, and reduced 50% of skeletal muscle fibrosis. Hence, collectively accelerating muscle regeneration process and preventing further myotoxin-induced muscle damage leading to fibrotic tissue and impairment in muscle function. Unfortunately, we could only speculate the maturation and functionality of iSkM from this combined therapeutic effect *in vivo*, which was significantly beneficial compared to other negative controls, as summarized in Table 3.

Employing the catalytically-deficient dCas9 system, dual fused with VP64 activation domains (VdC9BV), yielded a direct lineage conversion which offers economical, simple, safe, rapid, and accessible means to obtain autologous iSkMs while avoiding the use of iPSCs. Additionally, local delivery of reprogrammable cells obviates the need to directly inject the dCas9/gRNA elements for the *in vivo* reprogramming, thus precluding the off-targeting concerns associated with the CRISPR/Cas9 technology. Furthermore, this versatile tool offers multitudes of benefits for driving cell fate commitment: 1) it enables robust and efficient transcriptional activation of the endogenous gene(s) with an option to multiplex; and 2) unlike traditional transcription factor delivery, it allows activation of large-sized targets by recruiting gRNAs to the multiple target loci.

Collectively, demonstration of our work on CRISPR/dCas9-mediated *in situ* cell fate conversion bestows new source for autologous cell-based therapy in a pathophysiologically-relevant injury model in a postnatal mammalian tissue. As a proof-of-concept, this technique also offers possible means to utilize CRISPR/dCas9-based cell therapy for ameliorating other human injury or disease symptoms or understanding one's stem cell niche to ultimately aid in preclinical testing for new drug discovery and screening myotoxins for personalized medicine.

5.1.2. Conclusion for Chapter 4

It has been well documented that insoluble factors (including surface compositions, rigidity, and topology, or by delivering soluble transcription factors), which mimics the niche of the target organs, can regulate cellular behaviors and direct the cell fate towards the desired lineages. The detailed mechanisms of their effects on transforming cell behaviors, including proliferation, differentiation, and transdifferentiation, are not fully elucidated for all cell types. However, the spatiotemporal cues experienced by the cells resulted in facilitating reprogramming and transdifferentiation processes by committing to new cell identity.

In **Chapter 4.** Enhancing the neural cell fate commitment by deploying biochemical cues and substrate-mediated electrophysical cues, three different cell types were tested to explore how their cell fate decisions are affected by their exposed microenvironments. The specific biophysical cues of our interest were the unique surface characteristics offered by graphene:PLG composites, including the endogenous bioelectrical cue and the topographical cues from the microgrooved patterns in 3DG. Combined with the soluble and insoluble cues from the coated ECM proteins and the biochemical factors supplied from the media, we proposed that the efficiency of directed differentiation to sub-neuronal types (MN and DA neurons) and that of transdifferentiation to iNs would be enhanced on the graphene-based substrates.

As highlighted from our results, the physical properties of 3DG along with the soluble cues facilitated the directed differentiation and transdifferentiation of donor cells to target neuronal subtypes. On 3DG, the matured MN cells expressing HB9$^+$ and ChAT$^+$ increased by 10-fold, while for the graphene sheet, the mature MN population increased by 3-fold compared to the control (glass) substrate. Similarly, for the mature TH$^+$ DA neurons, 3DG promoted the maturation of DA neurons by 1.5-fold, whereas on the graphene sheet, TH$^+$ expression increased by 0.4-fold compared to that of control. Electroactive substrates also extended the neurite lengths of chemically-iNs, directly converted from fhDF-GFP. On day 15, 3DG facilitated to extend the neurite length by 7.5-fold, whereas, on a sheet, it was elongated by 1.5-fold. Unlike other neuronal cell types, the excitable pan-neurons preferred to elongate along the microgrooves of 3DG, as suggested by the quantified spatial directionality of the neurites.

Among all the target neuronal cells, DA neurons had the least effect on the substrate-medicated physical cues as no structured cell aggregates like MNs or neurite extension like iNs were observed along the microgrooves. Therefore, the 3DG platform may be more suitable for the differentiation of MNs and transdifferentiation of the chemically-iNs.

Collectively from our results, it can be implied that substrate-mediated biophysical and electrical cues, when coupled with biochemical stimuli, could offer a more permissive microenvironment to drive neural subtype specifications and transdifferentiation. Such cell fate transitions were promoted by enhancing the donor cell behaviors to adhere, spatially align, differentiate, and mature to target neuronal subtypes. Therefore, culturing donor cells in chemically-defined conditions on conductive graphene-based substrates with aligned patterns enable accessible means for improving the current differentiation protocol using the traditional tissue culture plate or glass substrate. By facilitating the cell fate conversion to a higher number of target neuronal subtypes for extended periods of *in vitro* culture, this electroactive *in vitro* culturing platform can be potentially utilized for regulating NS/PC fate and behaviors and for paving new therapeutic approaches for tissue engineering and regenerative medicine applications.

5.2. Future Perspectives

5.2.1. Future perspectives on increasing the clinical adaptability of CRISPR/dCas9 tool

For increasing the clinical utility of the CRISPR/dCas9, further efforts can be made to deliver smaller-sized cas9 variants and gRNAs in a polycistronic vector. In our approach, SpCas9 was utilized as the usage of ‘NGG,’ PAM sequence is commonly expressed in human cells. However, the cDNA for SpCas9 is estimated to be 4.1 kb long, which translates into 1368 amino acids (Jinek *et al*., 2012). As an alternative option, *Staphylococcus aureus* (SaCas9), which is 1000 bp smaller than SpCas9, can be utilized (Gee, Xu, & Hotta, 2017). Besides, reducing the size of Cas9 protein, gRNAs can be delivered more efficiently via a polycistronic vector, encoding multiple gRNAs by harnessing the natural tRNA-processing system for co-delivery of all gRNA elements in one vector (Xie, Minkenberg, & Yang, 2015). This eliminates the need to deliver redundant viral plasmid backbones to increase delivery efficiency. The polycistronic tRNA-gRNA (PTG) gene encodes for multiple tRNA-gRNAs under the polymerase III-promoter. Then, the endogenous tRNA-processing RNases get recruited and cut the gRNAs out from the PTG transcript, resulting in the recruitment of multiple gRNAs to the target loci. This technique would be particularly beneficial in clinical applications as the adeno-associated virus may be used as a safer option than lentivirus.

With the advances in epigenetic engineering, fusing these effector domains to CRISPR/dCas9 allows durable manipulation of multiple genes more efficiently without causing risky genetic mutations, associated with gene-editing. Molecules targeted for epigenetic manipulations involve DNA methylation, histone methylation, and acetylation. For instance, fusing dCas9 with the human acetyltransferase domain, p300 allows sufficient activation of a target gene from both promoter and the enhancer regions by catalyzing the targeted lysine 27 region of histone 3. Moreover, activation efficiency increases by de-condensing the chromatin structure for endogenous activation to occur in a more permissive environment for cell fate change. For the application of targeting neurodegenerative diseases or the brain injury, Geminin, a cell cycle regulator, can be fused to Cas9 for reducing the neurotoxicity in the brain by eliminating remaining Cas9 constructs after gene-editing (Yang, Li, & Li, 2018). Hence, with a reduction in size, increased in efficacy, and having safer AAV delivery options, targeted gene activation mediated by CRISPR/dCas9 can extend its clinical utility to achieve autologous-cell therapy or *in vivo* gene therapy for multiple human diseases/disorders with ease in multiplexing.

5.2.2. Future works proposed for Chapter 4

For neuronal cells obtained from **Chapter 4.** Enhancing the neural cell fate commitment by deploying biochemical cues and substrate-mediated electrophysical cues, we collectively exploited the microenvironmental cues mimicking the niche-like environs to guide stem cell fates to neurons. To better recapitulate the *bona fide* functional neurons *in vitro,* the investigation will proceed to confirm the functionality of MNs and iNs via conducting the whole-cell patch-clamp. This would validate the developed pre-synaptic and post-synaptic structures and ion channels for mature neurons. Two different options are proposed for analysis: 1) detaching the cells from graphene substrate to co-culture with mouse astrocyte feeder layer to support their growth after detachment, or 2) visualizing the cells directly on the graphene substrate by transducing the cells with pLV-hSyn-RFP; this plasmid allows the expression of RFP upon human synapsin activation. The second option would leave the intricate neurite formed by mature DA neurons, thereby potentially receiving higher populations cells with firing action potentials. However, graphene being not transparent, this option would require an inverted microscope to proceed.

After confirming the functionality of MNs, obtained cells can further extend its usage in vitro and *in vivo* applications for tissue engineering and regenerative medicine applications against neuronal diseases. It would be necessary to elucidate the molecular mechanisms of electroactive substrates on cell-to-matrix or cell-to-cell signal transduction. This would allow us to tailor the cell fate to the cell-specific platform, intricately designed for maximizing its clinical efficacy or mimicking its native behavior *in vitro*. Furthermore, knowing the specific cues to direct the cell fate to target cells offers exciting opportunities to realize personalized regenerative cell-based therapy by small molecules and conductive substrates, instead of genetically manipulations for the generation of medically-relevant cell types.

References

Abresch, R. T., Walsh, S. A., & Wineinger, M. A. (1998). Animal Models of Neuromuscular Diseases: Pathophysiology and Implications for Rehabilitation. *Physical Medicine and Rehabilitation Clinics*, *9*(1), 285–299. http://doi.org/10.1016/S1047-9651(18)30811-8

Ambasudhan, R., Talantova, M., Coleman, R., Yuan, X., Zhu, S., Lipton, S. A., & Ding, S. (2011). Direct Reprogramming of Adult Human Fibroblasts to Functional Neurons under Defined Conditions. *Stem Cell*, *9*(2), 113–118. http://doi.org/10.1016/j.stem.2011.07.002

Becker, D., Gary, D. S., Rosenzweig, E. S., Grill, W. M., & McDonald, J. W. (2010). Functional electrical stimulation helps replenish progenitor cells in the injured spinal cord of adult rats. *Experimental Neurology*, *222*(2), 211–218. http://doi.org/10.1016/j.expneurol.2009.12.029

Bentzinger, C. F., Wang, Y. X., Dumont, N. A., & Rudnicki, M. A. (2013). Cellular dynamics in the muscle satellite cell niche. Nature Publishing Group, 14(12), 1062–1072. http://doi.org/10.1038/embor.2013.182

Caiazzo, M., Dell'Anno, M. T., Dvoretskova, E., Lazarevic, D., Taverna, S., Leo, D., *et al.* (2011). Direct generation of functional dopaminergic neurons from mouse and human fibroblasts. *Nature*, *476*(7359), 224–U151. http://doi.org/10.1038/nature10284

Caiazzo, M., Okawa, Y., Ranga, A., Piersigilli, A., Tabata, Y., & Lutolf, M. P. (2016). Defined three-dimensional microenvironments boost induction of pluripotency. *Nature Materials*, *15*(3), 344–352. http://doi.org/10.1038/nmat4536

Cao, N., Huang, Y., Zheng, J., Spencer, C. I., Zhang, Y., Fu, J.-D., *et al.* (2016). Conversion of human fibroblasts into functional cardiomyocytes by small molecules. *Science*, *352*(6290), 1216–1220. http://doi.org/10.1126/science.aaf1502

Chakraborty, S., Ji, H., Kabadi, A. M., Gersbach, C. A., Christoforou, N., and Leong, K. W. (2014). A CRISPR/Cas9-Based System for Reprogramming Cell Lineage Specification. *Stem Cell Reports*. *3*(6):940-947. http://doi.org/10.1016/j.stemcr.2014.09.013

Chazaud, B., Sonnet, C., Lafuste, P., Bassez, G., Rimaniol, A.-C., Poron, F., *et al.* (2003). Satellite cells attract monocytes and use macrophages as a support to escape apoptosis and enhance muscle growth. *The Journal of Cell Biology*, *163*(5), 1133–1143. http://doi.org/10.1083/jcb.200212046

Choi, B., Park, K.-S., Kim, J.-H., Ko, K.-W., Kim, J.-S., Han, D. K., & Lee, S.-H. (2016). Stiffness of Hydrogels Regulates Cellular Reprogramming Efficiency Through Mesenchymal-to-Epithelial Transition and Stemness Markers. *Macromolecular Bioscience*, *16*(2), 199–206. http://doi.org/10.1002/mabi.201500273

Collins, C. A., Olsen, I., Zammit, P. S., Heslop, L., Petrie, A., Partridge, T. A., & Morgan, J. E. (2005). Stem cell function, self-renewal, and behavioral heterogeneity of cells from the adult muscle satellite cell niche. *Cell*, *122*(2), 289–301. http://doi.org/10.1016/j.cell.2005.05.010

Costa, K. D., Lee, E. J., & Holmes, J. W. (2003). Creating alignment and anisotropy in engineered heart tissue: Role of boundary conditions in a model three-dimensional culture system. *Tissue Engineering*, *9*(4), 567–577. http://doi.org/10.1089/107632703768247278

Crowder, S. W., Leonardo, V., Whittaker, T., Papathanasiou, P., & Stevens, M. M. (2016). Material Cues as Potent Regulators of Epigenetics and Stem Cell Function. *Cell Stem Cell*, *18*(1), 39–52. http://doi.org/10.1016/j.stem.2015.12.012

Darabi, R., Arpke, R. W., Irion, S., Dimos, J. T., Grskovic, M., Kyba, M., & Perlingeiro, R. C. R. (2012). Human ES- and iPSC-Derived Myogenic Progenitors Restore DYSTROPHIN and Improve Contractility upon Transplantation in Dystrophic Mice. Cell Stem Cell, 10(5), 610–619.

Davis, R. L., Weintraub, H., & Lassar, A. B. (1987). Expression of a single transfected cDNA converts fibroblasts to myoblasts. *Cell*, *51*(6), 987–1000.

Dingle, Y.-T. L., Boutin, M. E., Chirila, A. M., Livi, L. L., Labriola, N. R., Jakubek, L. M., *et al*. (2015). Three-Dimensional Neural Spheroid Culture: An *In Vitro* Model for Cortical Studies. *Tissue Engineering Part C: Methods*, *21*(12), 1274–1283. http://doi.org/10.1089/ten.tec.2015.0135

Downing, T. L., Soto, J., Morez, C., Houssin, T., Fritz, A., Yuan, F., *et al*. (2013). Biophysical regulation of epigenetic state and cell reprogramming. *Nature Materials*, *12*(12), 1154–1162. http://doi.org/10.1038/nmat3777

Ebrahimi, B. (2015). *Engineering Cell Fate: The Roles of iPSC Transcription Factors, Chemicals, Barriers and Enhancing Factors in Reprogramming and Transdifferentiation*. *bioRxiv* (pp. 1–50). Cold Spring Harbor Labs Journals.

Elkin, B. S., Azeloglu, E. U., Costa, K. D., & Morrison, B., III. (2007). Mechanical Heterogeneity of the Rat Hippocampus Measured by Atomic Force Microscope Indentation. *Home.Liebertpub.com*, *24*(5), 812–822. http://doi.org/10.1089/neu.2006.0169

Engler, A. J., Griffin, M. A., Sen, S., Bonnetnann, C. G., Sweeney, H. L., & Discher, D. E. (2004). Myotubes differentiate optimally on substrates with tissue-like stiffness: pathological implications for soft or stiff microenvironments. *The Journal of Cell Biology*, *166*(6), 877–887. http://doi.org/10.1083/jcb.200405004

Engler, A. J., Sen, S., Sweeney, H. L., & Discher, D. E. (2006). Matrix elasticity directs stem cell lineage specification. *Cell*, *126*(4), 677–689. http://doi.org/10.1016/j.cell.2006.06.044

Ferguson, J. E. III, Kelley, R. W., & Patterson, C. (2005). Mechanisms of Endothelial Differentiation in Embryonic Vasculogenesis. *Arteriosclerosis, Thrombosis, and Vascular Biology*. http://doi.org/10.1161/01.ATV.0000183609.55154.44

Forrest, A. D., Beggs, H. E., Reichardt, L. F., Dupree, J. L., Colello, R. J., & Fuss, B. (2009). Focal Adhesion Kinase (FAK): A Regulator of CNS Myelination. *Journal of Neuroscience Research*, *87*(15), 3456–3464. http://doi.org/10.1002/jnr.22022

Geng, X., Sun, T., Li, J.-H., Zhao, N., Wang, Y., & Yu, H.-L. (2015). Electroacupuncture in the repair of spinal cord injury: inhibiting the Notch signaling pathway and promoting neural stem cell proliferation. *Neural Regeneration Research*, *10*(3), 394–403. http://doi.org/10.4103/1673-5374.153687

Gilbert, P. M., Havenstrite, K. L., Magnusson, K. E. G., Sacco, A., Leonardi, N. A., Kraft, P., *et al*. (2010). Substrate Elasticity Regulates Skeletal Muscle Stem Cell Self-Renewal in Culture. *Science*, *329*(5995), 1078–1081. http://doi.org/10.1126/science.1191035

Github (Visited on March 21, 2017) http://oerpub.github.io/epubjs-demo-book/content/m46579.xhtml.

Grande, A., Sumiyoshi, K., López-Juárez, A., Howard, J., Sakthivel, B., Aronow, B., *et al*. (2013). Environmental impact on direct neuronal reprogramming *in vivo* in the adult brain. *Nature Communications*, *4*(1), 2373. http://doi.org/10.1038/ncomms3373

Gross, J. G., Bou-Gharios, G., & Morgan, J. E. (1999). Potentiation of myoblast transplantation by host muscle irradiation is dependent on the rate of radiation delivery. *Cell and Tissue Research*, *298*(2), 371–375.

Halim, A., Luo, Q., Ju, Y., & Song, G. (2018). A Mini Review Focused on the Recent Applications of Graphene Oxide in Stem Cell Growth and Differentiation. *Nanomaterials (Basel, Switzerland)*, *8*(9), 736. http://doi.org/10.3390/nano8090736

Han, D. W., Tapia, N., Hermann, A., Hemmer, K., Höing, S., Araúzo-Bravo, M. J., *et al*. (2012). Direct Reprogramming of Fibroblasts into Neural Stem Cells by Defined Factors. *Cell Stem Cell*, *10*(4), 465–472. http://doi.org/10.1016/j.stem.2012.02.021

Hendry, C. E., & Little, M. H. (2012). Reprogramming the kidney: a novel approach for regeneration. Kidney International, 82(2), 138–146. http://doi.org/10.1038/ki.2012.68

Horna, D., Ramírez, J. C., Cifuentes, A., Bernad, A., Borrós, S., & González, M. A. (2012). Efficient cell reprogramming using bioengineered surfaces. *Advanced Healthcare Materials*, *1*(2), 177–182. http://doi.org/10.1002/adhm.201200017

Hu, W., Qiu, B., Guan, W., Wang, Q., Wang, M., Li, W., *et al*. (2015). Direct Conversion of Normal and Alzheimer's Disease Human Fibroblasts into Neuronal Cells by Small Molecules. *Stem Cell*, *17*(2), 204–212. http://doi.org/10.1016/j.stem.2015.07.006

Huang, Y., Li, Y., Chen, J., Zhou, H., & Tan, S. (2015). Electrical stimulation elicits neural stem cells activation: new perspectives in CNS repair. *Frontiers in Human Neuroscience*, *9*. http://doi.org/10.3389/fnhum.2015.00586

Ichida, J. K., Blanchard, J., Lam, K., Son, E. Y., Chung, J. E., Egli, D., *et al*. (2009). A Small-Molecule Inhibitor of TGF-beta Signaling Replaces Sox2 in Reprogramming by Inducing Nanog. *Stem Cell*, *5*(5), 491–503. http://doi.org/10.1016/j.stem.2009.09.012

Iskratsch, T., Wolfenson, H., & Sheetz, M. P. (2014). Appreciating force and shape — the rise of mechanotransduction in cell biology. *Nature Publishing Group*, *15*(12), 825–833. http://doi.org/10.1038/nrm3903

Järvinen, T. A. H., Järvinen, T. L. N., Kääriäinen, M., Kalimo, H., & Järvinen, M. (2017). Muscle Injuries: Biology and Treatment. *The American Journal of Sports Medicine*, *33*(5), 745–764. http://doi.org/10.1177/0363546505274714

Jakus, A. E., Secor, E. B., Rutz, A. L., Jordan, S. W., Hersam, M. C., & Shah, R. N. (2015). Three-Dimensional Printing of High-Content Graphene Scaffolds for Electronic and Biomedical Applications. *ACS Nano*, *9*(4), 4636–4648. http://doi.org/10.1021/acsnano.5b01179

Jinek, M., Chylinski, K., Fonfara, I., Hauer, M., Doudna, J. A., & Charpentier, E. (2012). A Programmable Dual-RNA–Guided DNA Endonuclease in Adaptive Bacterial Immunity. *Science*, *337*(6096), 816–821. http://doi.org/10.1126/science.1225829

Joe, A. W. B., Yi, L., Natarajan, A., Le Grand, F., So, L., Wang, J., *et al*. (2010). Muscle injury activates resident fibro/adipogenic progenitors that facilitate myogenesis. Nature Cell Biology, 12(2), 153–163. http://doi.org/10.1038/ncb2015

Jordan, P. M., Ojeda, L. D., Thonhoff, J. R., Gao, J., Boehning, D., Yu, Y., & Wu, P. (2009). Generation of spinal motor neurons from human fetal brain-derived neural stem cells: Role of basic fibroblast growth factor. *Journal of Neuroscience Research*, *87*(2), 318–332. http://doi.org/10.1002/jnr.21856

Kenry, Lee, W. C., Loh, K. P., & Lim, C. T. (2018). When stem cells meet graphene: Opportunities and challenges in regenerative medicine. *Biomaterials*, *155*, 236–250. http://doi.org/10.1016/j.biomaterials.2017.10.004

Kim, D.-H., Lipke, E. A., Kim, P., Cheong, R., Thompson, S., Delannoy, M., *et al*. (2010). Nanoscale cues regulate the structure and function of macroscopic cardiac tissue constructs. *Proceedings of the National Academy of Sciences*, *107*(2), 565–570. http://doi.org/10.1073/pnas.0906504107

Kim, K., Doi, A., Wen, B., Ng, K., Zhao, R., Cahan, P., *et al*. (2010). Epigenetic memory in induced pluripotent stem cells. *Nature*, *467*(7313), 285–290. http://doi.org/10.1038/nature09342

Kriks, S., Shim, J.-W., Piao, J., Ganat, Y. M., Wakeman, D. R., Xie, Z., *et al*. (2011). Dopamine neurons derived from human ES cells efficiently engraft in animal models of Parkinson's disease. *Nature*, *480*(7378), 547. http://doi.org/10.1038/nature10648

Kulangara, K., Adler, A. F., Wang, H., Chellappan, M., Hammett, E., Yasuda, R., & Leong, K. W. (2014). The effect of substrate topography on direct reprogramming of fibroblasts to induced neurons. *Biomaterials*, *35*(20), 5327–5336. http://doi.org/10.1016/j.biomaterials.2014.03.034

Le Grand, F., & Rudnicki, M. (2007). Satellite and stem cells in muscle growth and repair. *Development*, *134*(22), 3953–3957. http://doi.org/10.1242/dev.005934

Li, X., Guo, F., Zhang, Q., Huo, T., Liu, L., Wei, H., *et al.* (2014). Electroacupuncture decreases cognitive impairment and promotes neurogenesis in the APP/PS1 transgenic mice. *BMC Complementary and Alternative Medicine*, *14*(1), 37. http://doi.org/10.1186/1472-6882-14-37

Liu, Z. Q. (1991). Scale space approach to directional analysis of images. *Applied Optics*, *30*(11), 1369–1373. http://doi.org/10.1364/AO.30.001369

Mali, P., Yang, L., Esvelt, K.M., Aach, J., Guell, M., DiCarlo, J.E., Norville, J.E. and Church, G.M. (2013) RNA-guided human genome engineering via Cas9. Science, 339, 823-826.

Manzano, R., Toivonen, J. M., Calvo, A. C., Miana-Mena, F. J., Zaragoza, P., Muñoz, M. J., *et al*. (2011). Sex, fiber-type, and age dependent *in vitro* proliferation of mouse muscle satellite cells. *Journal of Cellular Biochemistry*, *112*(10), 2825–2836. http://doi.org/10.1002/jcb.23197

Mead, L. E., Prater, D., Yoder, M. C., & Ingram, D. A. (2008). Isolation and characterization of endothelial progenitor cells from human blood. *Current Protocols in Stem Cell Biology*, *Chapter 2*, Unit 2C.1. http://doi.org/10.1002/9780470151808.sc02c01s6

Milisav, I. (2011). Cellular Stress Responses, Advances in Regenerative Medicine, Sabine Wislet-Gendebien, IntechOpen, DOI: 10.5772/26118. Available from: https://www.intechopen.com/books/advances-in-regenerative-medicine/cellular-stress-responses

Missirlis, Y. F. (2016). Mechanoepigenetics. *Frontiers in Cell and Developmental Biology*, *4*, 1047. http://doi.org/10.3389/fcell.2016.00113

Morez, C., Noseda, M., Paiva, M. A., Belian, E., Schneider, M. D., & Stevens, M. M. (2015). Enhanced efficiency of genetic programming toward cardiomyocyte creation through topographical cues. *Biomaterials*, *70*, 94–104. http://doi.org/10.1016/j.biomaterials.2015.07.063

Natarajan, R. *et al*., “STAT3 Modulation to Enhance Motor Neuron Differentiation in Human Neural Stem Cells,” ed. Wenhui Hu, *Plos One* 9, no. 6 (June 19, 2014): e100405, doi:10.1371/journal.pone.0100405.

NIH, Clinical Trials 1 (Visited on April 1st, 2019)
https://clinicaltrials.gov/ct2/results?recrs=&cond=ALS+%28Amyotrophic+Lateral+Sclerosis%29&term=cell+transplantation&cntry=&state=&city=&dist=

NIH, Clinical Trials 2 (Visited on April 1st, 2019) https://clinicaltrials.gov/ct2/results?cond=Parkinson+Disease&term=cell+transplantation&cntry=&state=&city=&dist=

Niu, W., Zang, T., Zou, Y., Fang, S., Smith, D. K., Bachoo, R., & Zhang, C.-L. (2013). *In vivo* reprogramming of astrocytes to neuroblasts in the adult brain. *Nature Cell Biology*, *15*(10), 1164–1175. http://doi.org/10.1038/ncb2843

Park, S. Y., Park, J., Sim, S. H., Sung, M. G., Kim, K. S., Hong, B. H., & Hong, S. (2011). Enhanced Differentiation of Human Neural Stem Cells into Neurons on Graphene. *Advanced Materials*, *23*(36), H263–. http://doi.org/10.1002/adma.201101503

Pastrana, E., Silva-Vargas, V., & Doetsch, F. (2011). Eyes Wide Open: A Critical Review of Sphere-Formation as an Assay for Stem Cells. *Cell Stem Cell*, *8*(5), 486–498. http://doi.org/10.1016/j.stem.2011.04.007

Paszek, M. J., zahir, N., Johnson, K. R., Lakins, J. N., Rozenberg, G. I., Gefen, A., *et al.* (2005). Tensional homeostasis and the malignant phenotype. *Cancer Cell*, *8*(3), 241–254. http://doi.org/10.1016/j.ccr.2005.08.010

Petrov, D., Mansfield, C., Moussy, A., & Hermine, O. (2017). ALS Clinical Trials Review: 20 Years of Failure. Are We Any Closer to Registering a New Treatment? *Frontiers in Aging Neuroscience*, *9*(e61177), 610. http://doi.org/10.3389/fnagi.2017.00068

Pothos, E., Desmond, M., & Sulzer, D. (1996). L-3,4-dihydroxyphenylalanine increases the quantal size of exocytotic dopamine release *in vitro*. *Journal of Neurochemistry*, *66*(2), 629–636.

Purves, D., Fitzpatrick, D., Katz, L. C., Lamantia, A.-S., McNamara, J. O., Williams, S. M., & Augustine, G. J. (2001). Neuroscience.

Qi, L. S., Larson, M. H., Gilbert, L. A., Doudna, J. A., Weissman, J. S., Arkin, A. P., & Lim, W. A. (2013). Repurposing CRISPR as an RNA-guided platform for sequence-specific control of gene expression. *Cell*, *152*(5), 1173–1183. http://doi.org/10.1016/j.cell.2013.02.022

Relucio, J., Menezes, M. J., Miyagoe-Suzuki, Y., Takeda, S., & Colognato, H. (2012). Laminin regulates postnatal oligodendrocyte production by promoting oligodendrocyte progenitor survival in the subventricular zone. *Glia*, *60*(10), 1451–1467. http://doi.org/10.1002/glia.22365

Schmalbruch, H., & Lewis, D. M. (2000). Dynamics of nuclei of muscle fibers and connective tissue cells in normal and denervated rat muscles. *Muscle & Nerve*, *23*(4), 617–626.

Schofield, R. (1978). The relationship between the spleen colony-forming cell and the haemopoietic stem cell. *Blood Cells*, *4*(1-2), 7–25.

Slack, J. M. W. (2007). Metaplasia and transdifferentiation: from pure biology to the clinic. *Nature Reviews Molecular Cell Biology*, *8*(5), 369–378. http://doi.org/10.1038/nrm2146

Shah, S., Yin, P. T., Uehara, T. M., Chueng, S.-T. D., Yang, L., & Lee, K.-B. (2014). Guiding Stem Cell Differentiation into Oligodendrocytes Using Graphene-Nanofiber Hybrid Scaffolds. *Advanced Materials*, *26*(22), 3673–3680. http://doi.org/10.1002/adma.201400523

Shin, H., Jo, S., & Mikos, A. G. (2003). Biomimetic materials for tissue engineering. Biomaterials, 24(24), 4353–4364. http://doi.org/10.1016/S0142-9612(03)00339-9

Shultz, L. D., Schweitzer, P. A., Christianson, S. W., Gott, B., Schweitzer, I. B., Tennent, B., *et al*. (1995). Multiple defects in innate and adaptive immunologic function in NOD/LtSz-scid mice. *Journal of Immunology (Baltimore, Md. : 1950)*, *154*(1), 180–191.

Sia, J., Yu, P., Srivastava, D., & Li, S. (2016). Effect of biophysical cues on reprogramming to cardiomyocytes. *Biomaterials*, *103*, 1–11. http://doi.org/10.1016/j.biomaterials.2016.06.034

Steinbeck, J. A., Choi, S. J., Mrejeru, A., Ganat, Y., Deisseroth, K., Sulzer, D., *et al*. (2015). Optogenetics enables functional analysis of human embryonic stem cell-derived grafts in a Parkinson's disease model. *Nature Biotechnology*, *33*(2), 204–209. http://doi.org/10.1038/nbt.3124

Takahashi, K. (2012). Cellular reprogramming – lowering gravity on Waddington's epigenetic landscape. *J Cell Sci*, *125*(11), 2553–2560. http://doi.org/10.1242/jcs.084822

Tan, S. J., Fang, J. Y., Wu, Y., Yang, Z., Liang, G., & Han, B. (2015). Muscle tissue engineering and regeneration through epigenetic reprogramming and scaffold manipulation. *Scientific Reports*, *5*(1), 16333. http://doi.org/10.1038/srep16333

Tomishima, M. (2012). Midbrain dopamine neurons from hESCs. Stembook.org

Tong, Y., Bohm, S., & Song, M. (2013). Graphene based materials and their composites as coatings. *Austin Journal of Nanomedicine Nanotechnology*, *1*(1), 1–16.

Smith, A. W., Hoyne, J. D., Nguyen, P. K., McCreedy, D. A., Aly, H., Efimov, I. R., *et al*. (2013). Direct reprogramming of mouse fibroblasts to cardiomyocyte-like cells using Yamanaka factors on engineered poly(ethylene glycol) (PEG) hydrogels. *Biomaterials*, *34*(28), 6559–6571. http://doi.org/10.1016/j.biomaterials.2013.05.050

Uz, M., Buyukoz, M., Sharma, A. D., Sakaguchi, D. S., Altinkaya, S. A., & Mallapragada, S. K. (2017). Gelatin-Based 3D Conduits for Transdifferentiation of Mesenchymal Stem Cells into Schwann Cell-like Phenotypes. *Acta Biomaterialia*, *53*, 293–306. http://doi.org/10.1016/j.actbio.2017.02.018

Vierbuchen, Thomas, and Marius Wernig. “Molecular Roadblocks for Cellular Reprogramming.” *Molecular Cell* 47, no. 6 (September 28, 2012): 827–38. doi:10.1016/j.molcel.2012.09.008.

Vierbuchen, T., Ostermeier, A., Pang, Z. P., Kokubu, Y., Südhof, T. C., & Wernig, M. (2010). Direct conversion of fibroblasts to functional neurons by defined factors. *Nature*, *463*(7284), 1035–1041. http://doi.org/10.1038/nature08797

Watanabe, A., Yamada, Y., & Yamanaka, S. (2013). Epigenetic regulation in pluripotent stem cells: a key to breaking the epigenetic barrier. *Philosophical Transactions of the Royal Society B: Biological Sciences*, *368*(1609), 20120292–20120292. http://doi.org/10.1098/rstb.2012.0292

Watt, F. M., & Huck, W. T. S. (2013). Role of the extracellular matrix in regulating stem cell fate. *Nature Reviews Molecular Cell Biology*, *14*(8), 467–473. http://doi.org/10.1038/nrm3620

Weintraub, H., Tapscott, S. J., Davis, R. L., Thayer, M. J., Adam, M. A., Lassar, A. B., & Miller, A. D. (1989). Activation of muscle-specific genes in pigment, nerve, fat, liver, and fibroblast cell lines by forced expression of MyoD. *Proceedings of the National Academy of Sciences*, *86*(14), 5434–5438. http://doi.org/10.1073/pnas.86.14.5434

Xie, K., Minkenberg, B., & Yang, Y. (2015). Boosting CRISPR/Cas9 multiplex editing capability with the endogenous tRNA-processing system. *Proceedings of the National Academy of Sciences*, *112*(11), 3570–3575. http://doi.org/10.1073/pnas.1420294112

Xu, X., Wilschut, K. J., Kouklis, G., Tian, H., Hesse, R., Garland, C., et al. (2015). Human Satellite Cell Transplantation and Regeneration from Diverse Skeletal Muscles. *Stem Cell Reports*, *5*(3), 419–434. http://doi.org/10.1016/j.stemcr.2015.07.016

Yang, S., Li, S., & Li, X.-J. (2018). Shortening the Half-Life of Cas9 Maintains Its Gene Editing Ability and Reduces Neuronal Toxicity. *CellReports*, *25*(10), 2653–. http://doi.org/10.1016/j.celrep.2018.11.019

Ye, J., Ge, J., Zhang, X., Cheng, L., Zhang, Z., He, S., *et al*. (2016). Pluripotent stem cells induced from mouse neural stem cells and small intestinal epithelial cells by small molecule compounds. *Cell Research*, *26*(1), 34–45. http://doi.org/10.1038/cr.2015.142

Yim, E. K. F., Pang, S. W., & Leong, K. W. (2007). Synthetic nanostructures inducing differentiation of human mesenchymal stem cells into neuronal lineage. *Experimental Cell Research*, *313*(9), 1820–1829. http://doi.org/10.1016/j.yexcr.2007.02.031

Yoo, J., Noh, M., Kim, H., Jeon, N. L., Kim, B.-S., & Kim, J. (2015). Nanogrooved substrate promotes direct lineage reprogramming of fibroblasts to functional induced dopaminergic neurons. *Biomaterials*, *45*, 36–45. http://doi.org/10.1016/j.biomaterials.2014.12.049

Yoo, J., Kim, J., BAEK, S., Park, Y., Im, H., & Kim, J. (2014). Cell reprogramming into the pluripotent state using graphene based substrates. *Biomaterials*, *35*(29), 8321–8329. http://doi.org/10.1016/j.biomaterials.2014.05.096

Wang, N., Tytell, J. D., & Ingber, D. E. (2009). Mechanotransduction at a distance: mechanically coupling the extracellular matrix with the nucleus. *Nature Publishing Group*, *10*(1), 75–82. http://doi.org/10.1038/nrm2594

Zhang, Y., Li, W., Laurent, T., & Ding, S. (2012). Small molecules, big roles -- the chemical manipulation of stem cell fate and somatic cell reprogramming. *Journal of Cell Science*, *125*(Pt 23), 5609–5620. http://doi.org/10.1242/jcs.096032

Zhou, P., Wu, F., Zhou, T., Cai, X., Zhang, S., Zhang, X., *et al*. (2016). Simple and versatile synthetic polydopamine-based surface supports reprogramming of human somatic cells and long-term self-renewal of human pluripotent stem cells under defined conditions. *Biomaterials*, *87*, 1–17. http://doi.org/10.1016/j.biomaterials.2016.02.012